Two Problems on Driven Granular Matter: Poiseuille and Taylor-Couette Flows

A Thesis
Submitted for the Degree of
Master of Science (Engineering)

by

Achal Mahajan

Engineering Mechanics Unit
Jawaharlal Nehru Centre for Advanced Scientific Research
(A Deemed University)
Bangalore – 560 064

JULY 2016

My family

DECLARATION

I hereby declare that the matter embodied in the thesis entitled "**Two Problems on Driven Granular Matter: Poiseuille and Taylor-Couette Flows**" is the result of investigations carried out by me at the Engineering Mechanics Unit, Jawaharlal Nehru Centre for Advanced Scientific Research, Bangalore, India under the supervision of **Prof. Meheboob Alam** and that it has not been submitted elsewhere for the award of any degree or diploma.

In keeping with the general practice in reporting scientific observations, due acknowledgment has been made whenever the work described is based on the findings of other investigators.

Achal Mahajan

CERTIFICATE

I hereby certify that the matter embodied in this thesis entitled "**Two Problems on Driven Granular Matter: Poiseuille and Taylor-Couette Flows**" has been carried out by **Mr. Achal Mahajan** at the Engineering Mechanics Unit, Jawaharlal Nehru Centre for Advanced Scientific Research, Bangalore, India under my supervision and that it has not been submitted elsewhere for the award of any degree or diploma.

Prof. Meheboob Alam
(Research Supervisor)

Acknowledgements

This thesis not only represents the work on a computer but a three year long roller coaster ride filled with ups and downs. My experience at JNCASR is nothing short of amazing. The passion to pursue fluid mechanics research as a career has increased many folds, and it is because of the stimulating environment to learn and grow both intellectually and philosophically which has made me a responsible researcher. I welcome this opportunity to thank all those people who helped me in pursuing my thesis project with their valuable comments and ideas. I would like to express my special appreciation and thanks to my advisor Professor Meheboob Alam, who has been a tremendous mentor for me. I would like to thank him for encouraging my research and for allowing me to grow as a research scientist. His advice on both research as well as on my career have been priceless. I thank Prof. K. R. Sreenivas and Prof. Ganesh Subramanian for their role in my development. I am also grateful to Prof. Sreekumar (NITK) for shining the first glance of research and on sustainabile living. He will always be a source of inspiration to me in my pursuit to have even a minuscule (perhaps profound) impact on the community through my work.

I would like to thank people who have supported and helped me so much throughout this period. I thank my fellow labmates, Reddy, TSunil, Nandu, Saikat, Ramki, Ronak and Pratik, for the stimulating discussions on various issues ranging from socialism to football. Also I thank my friends Paaji, Pande, Ponnu, Paavin, Chakri, Shank, Rafi, Sanki, Vybhav, Navaneeth and Mili in the department for their care and precious friendship during my stay at JNC.

Various beer sessions with Aditya, Manjeet, Raaghesh and Neha made my weekends mesmerising. I would never forget the beautiful moments I had shared with them. Special thanks to Aditya and Manjeet who have been there with me throughout this long period. From long treks to long drives, the sudden plans and squeezing time in a busy schedule, the stories are never ending. My dance partners in various events, Jigyasa and Aishwariya, for being patient in learning difficult moves. The simple phrase, "thank you", cannot present how much their friendship means to me. Thanks to the basketball community in JNCASR, my evenings were always fruitful and the pleasure to be actively involved in a sport gave me mental and physical strength to return strongly whenever I was feeling low. I can never forget the wonderful breweries of Bangalore for their amazing beers and crowd on weekends.

I express my gratitude to the Department of Science and Technology (DST) for funding my Masters studies through the fellowship. I thank the academic, admin, security, mess committee for all their support. I thank JNCASR for providing all facilities to pursue my graduation. I thank my family for their support who never questioned my ability and pursuit of knowledge. Words cannot express how grateful I am to my mother, sister and father for all of the sacrifices that they have made on my behalf.

Abstract

This dissertation describes the physics of granular particles in two different flow configuration: Poiseuille and Taylor-Couette. In the first part, smooth inelastic disks are allowed to flow under the effect of gravity in a two-dimensional channel. The particles are modeled as inelastic hard particles which interact through binary collisions using event-driven molecular dynamics simulations. In the second part, the particles are allowed to rotate in a cylindrical geometry confined in the annular region between two cylinders, dubbed Taylor-Couette (TC) flow, with inner cylinder rotating with different rotation rates in the absence of gravity.

Granular Poiseuille flow

The numerical simulation of gravity-driven flow of smooth inelastic hard-disks through a channel, dubbed 'granular' Poiseuille flow, is conducted using event-driven techniques. We find that the variation of the mass-flow rate (Q) with Knudsen number (Kn) can be non-monotonic in the elastic limit (i.e. the restitution coefficient $e_n \to 1$) in channels with very smooth walls. The *Knudsen-minimum* effect (i.e. the minimum flow rate occurring at $Kn \sim O(1)$ for the Poiseuille flow of a molecular gas) is found to be absent in a granular gas with $e_n < 0.99$, irrespective of the value of the wall roughness. Another rarefaction phenomenon, the *bimodality* of the temperature profile, with a local minimum ($T_{\min}$) at the channel centerline and two symmetric maxima ($T_{\max}$) away from the centerline, is also studied. We show that the inelastic dissipation is responsible for the onset of temperature bimodality [i.e. the 'excess' temperature, $\triangle T = (T_{\max}/T_{\min} - 1) \neq 0$] near the continuum limit ($Kn \sim 0$), but the rarefaction being its origin (as in the molecular gas) holds beyond $Kn \sim O(0.1)$. The competition between dissipation and rarefaction seems to be responsible for the observed dependence of both the mass-flow rate and the temperature bimodality on Kn and e_n in this flow. The validity of the Navier-Stokes-order hydrodynamics for granular Poiseuille flow is discussed with reference to the prediction of bimodal temperature profiles and related surrogates.

Granular Taylor-Couette flow

In the second part of the thesis, event-driven simulations of smooth hard spheres in Taylor-Couette setup are carried out in the absence of gravity. Mean field properties like velocity (U), granular temperature (T), volume fraction (ν) and angular momentum (l), as functions of normal restitution coefficient (e_n), gap width (d_w) and rotation rate (ω_i), are studied in both two and three-dimensions. For dissipative systems ($e_n < 1$), the particles accumulate, thereby, forming a particle-rich cluster and exhibiting various patterns and structures in two-dimensions. Effects of different axial wall boundary conditions are characterised. The strength of the Taylor-like vortices is found to a reduce in granular system, and a new type of vorticity-banding (axial bands of particle-rich and particle-depleted regions) is uncovered.

List of Figures

List of Tables

Contents

Chapter 1

Introduction

Granular matter has intrigued many researchers for a long time (Faraday 1831; Raman 1923), but a thorough understanding was made after the seminal work by Bagnold (Bagnold 1954) and his book on granular matter (Bagnold 1941) is still an important reference to this day. The first recorded evidence of scientific importance was made by Lucretius, the Latin philosopher 100 years after Archimedes (circa 200 B.C.) calculated the number of grains of sand that would fill the universe. He was one of the few pioneers to ponder on the flowing grains, and was quoted *"One can scoop up poppy seeds with a ladle as easily as if they were water and, when dipping the ladle the seeds flow in a continuous stream"* (Duran 2012).

Granular particles can be found in different sizes and shapes, and due to this anistropy in structure, it shows many interesting features. They are a large conglomeration of discrete solid macroscopic particles, characterized by a loss in energy of the particles on interacting with each other. The thermal energy of granular materials is much lower compared to that in its molecular counterpart as the size of the constituent particles is larger than a gas molecule. The size of the particles can vary from 1 μm, below this size Brownian motion of the particle becomes dominant, found in sand to kilometres found in asteroid belts of the solar system with individual grains being asteroids. In general, the collective motion of granular particles can exist in solid, liquid, and gaseous phases depending on the density and the energy of the individual particle.

Many food processing and pharmaceutical industries rely on the effective transportation, processing and storage of granular materials which are in the form of seeds, grains and food products along with products like medical tablets. Estimates show that we waste 60 % (Duran 2012) of the capacity of many of our industrial plants due to problems related to the transport of these materials from part of the factory floor to another. Hence even a small improvement in our understanding of how granular media behave should have a profound impact for industry. Statistics indicate that *"the processing of granular media and aggregates consumes roughly 10% of all energy produced on this planet. As it turns out, this class of materials ranks second, immediately behind water, on the scale of priorities of human activity. As such, any advance in understanding the physics of granulars is bound to have a major economic impact."* (Duran 2012).

Real granular flows (Campbell 1990; Goldhirsch 2003; Forterre & Pouliquen 2008) can be subject to a plethora of complicating forces. These include adhesion, cohesion, van der Waals forces, magnetic forces and capillary forces from the interstitial fluid. Indeed, even without any of these effects, the description of a dry, cohesionless granular material still represents a challenge and the question of which equations should be used in a given situation is still controversial. A number of effects complicate the use of traditional continuum thermo- and hydro-dynamical principles. A lack of separation of scales among typical flow lengths and the size of the constitutive particles means that continuum models often cannot capture many important

features of granular materials. Also, the inherent dissipation of energy present in the form of inelasticity due to collision of particles forces the system to be unsteady locally and pushes it away from equilibrium. Since inelasticity renders any thermal motion unimportant when compared to the dynamical forces acting on the grains, the system can be considered athermal.

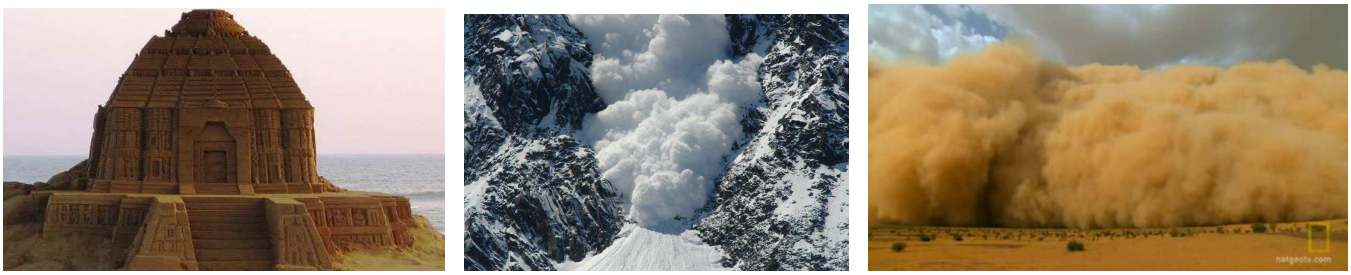

(a) (b) (c)

Figure 1.1: Existence of granular matter in three phases:(a) Solid, (b) Liquid and (c) Gas.

In fact, it is an open question in the study of granular physics if a single set of constitutive relations will ever capture the wide spectrum of granular behaviours. As a result, granular physicists do not have the same framework as fluid dynamicists, who can exploit the well-tested Navier-Stokes equations. Depending on the mode of deformation, granular material can behave as a gas, liquid or solid; indeed, all three phases can co-exist in granular chute flow and the distinction between the three is not well-defined. Figure 1.1 serves to introduce three main phases of granular materials. What needs to be highlighted is that despite their apparent simplicity, granular materials behave differently from solids, liquids and gases and should therefore be considered an additional state of matter (Jaeger *et al.* 1996). With a wide variety of different behaviour possible, it seems unlikely that a single continuum model will be capable of capturing the entire spectrum of granular phenomenology. However, a good description of gas-like granular flows already exists in modified forms of kinetic theory, such as those described by Brilliantov & Pöschel (2004) taking inspiration from the kinetic theory of gases (Chapman & Cowling 1970; Jenkins & Savage 1983; Jenkins & Richman 1985).

At higher densities, the flow is very slow and the dynamics is governed by enduring contacts and force chains, caused primarily by the inter-particle friction. As such a granular material deforming in this way behaves much like a plastic solid; although for static assemblies of granular materials under very low shear, the assembly responds as an elastic solid (Brown & Richards 1970). This is in contrast to the dominant transfer mechanism of binary collisions in the kinetic regime. The "quasi-static" flow of granular materials has been studied in depth by the soil mechanics community and is well described by critical-state and plasticity theories (Nedderman 2005; Rao & Nott 2008). In addition to gas, solid and liquid phases, grains can also exhibit a slow creeping flow, analogous to a glass (Jaeger *et al.* 1989).

In the region between the kinetic and quasi-static regimes the granular materials flow like a liquid (Fig. 1.1(b)). In this case, the interactions between particles are governed by collisions, frictional interactions and geometric entanglement of the particles. Persistent contacts and force chains can also play a role, as the volume fraction is only slightly less than that of the solid

phase. In a broad sense, such dense granular flows can be placed in the visco-plastic family of materials, as it has a yield stress and a shear-rate dependent rheology, with the latter being responsible for its viscous-like behaviour.

1.1 Chapter organization

In the present study we consider flow of dry granular matter. A simple problem of the flow of granular particles in a channel under the influence of gravity (Poiseuille flow) is simulated in two-dimensions (2D) in Chapter 2. The development and validation of 2D and 3D codes for granular flows in an annular geometry (Taylor-Couette flow) are discussed in Chapter 3. The 2D and 3D Taylor-Couette flow results are dealt in Chapters 4 and 5, respectively.

Chapter 2

In this chapter, two important rarefaction effects, Knudsen minimum and temperature bimodality, are explained (Alam *et al.* 2015). The hard sphere collision dynamics of two granular particles is explained with schematic diagrams. The equations used to obtain the mean properties like velocity, volume fraction and density are listed.

Chapter 3

This chapter mainly deals with a brief intorduction on Taylor-Couette flow along with details about the development of molecular dynamics (MD) code and its validation with the existing literature. A general introduction on the Taylor-Couette flow is given with a focus on present problems. The extension of 2D code used in Chapter 2 to 3D is explained in detail with wall boundary conditions used. The 2D and 3D results are validated with the existing literature and a good qualitative agreement is observed.

Chapter 4

In this chapter, we deal with smooth inelastic granular disks in an annular region with the inner disk rotating at ω_i. Simulations are carried out for both low and high densities to capture the effects of rarefaction and dissipation. It is observed that the flow at low Knudsen number (Kn) is greatly dominated by dissipation in the system and by rarefaction at high Kn. Hydrodynamic properties are examined at varying normal restitution coefficient (e_n), gap width (d_w) and rotation rate (ω_i). Various other results are discussed in this chapter.

Chapter 5

Here, we extend the analysis from two-dimensional annular geometry to three-dimensional cylindrical setup with the emphasis on assessing the roles of end-walls and restitution coefficient on vortex formation. All simulations in this chapter are done for moderately dense flows ($\nu_{av} = 0.2$). The first part deals with the effect of using different axial wall boundary conditions for an elastic system. In the second part, the focus shifts to addressing the role of dissipation on the vortex dynamics in a Taylor-Couette setup followed by summary and conclusions in Chapter 6.

Chapter 2

Dilute Granular Poiseuille Flow[†]

2.1 Introduction

The compressible Navier-Stokes-Fourier (NSF) equations are routinely used to analyse gas flows when the Knudsen number (Kn, the ratio between the mean free path and the macroscopic length of the system), is close to zero. For flows with large Knudsen numbers, the traditional low-order hydrodynamic equations are unable to predict many flow features including the velocity-slip and temperature-jump at the walls, both being signatures of rarefaction effects. In molecular gases the flows are empirically classified based on Knudsen number (Kogan 1969; Bird 1994): (i) continuum regime ($Kn \leq 10^{-2}$), (ii) slip flow ($10^{-2} < Kn < 0.1$), (iii) transition flow ($0.1 < Kn < 10$) and (iv) free-molecular flow ($Kn \geq O(10)$). The slip and transition regimes fall under the category of 'rarefied' flows. The Boltzmann equation with appropriate boundary conditions can describe all flow regimes, unfortunately, however, it is not possible to solve Boltzmann equation, even semi-analytically, for all Kn. The NSF equations augmented by slip boundary conditions can describe slip-flow regime reasonably well, but they fail when the Knudsen number is larger. One approach to model rarefied flows is to solve Boltzmann equation via the direct simulation Monte Carlo (DSMC) method which is, however, computationally expensive (Bird 1994); an alternative to DSMC is to use coarse-grained equations for extended sets of hydrodynamic fields. Such higher-order hydrodynamic equations, like the Burnett or super-Burnett equations (Burnett 1935) or the Grad's moment equations (Grad 1949) or the regularized moment equations (Torrilhon & Struchtrup 2004), seem to work well in the rarefied regimes of slip and transition flows up-to a Knudsen number of $O(1)$.

Rarefaction effects lead to non-Newtonian and non-Fourier transport coefficients, like the normal stress differences and 'anisotropic' thermal conductivity tensor, respectively, in molecular gases (Burnett 1935; Grad 1949; Kogan 1969) as well as in dilute granular gases (Saha & Alam 2014, 2016). At the level of hydrodynamic fields, one prototypical signature of rarefaction is the well-known 'Knudsen-minimum' effect (Knudsen 1909) in Poiseuille flow: the mass-flow rate of a molecular gas decreases with increasing Knudsen number (Kn), reaches a minimum at $Kn \sim O(1)$ and increases again with further increase in Kn; this is also referred as 'Knudsen-paradox'. The Knudsen-minimum/Knudsen-paradox has been predicted by analysing the steady Boltzmann equation with a BGK (Bhatnagar-Gross-Krook) collision term (Cercignani & Daneri 1963) – the flow rate is inversely proportional to Kn for small Kn, but increases logarithmically ($\sim \log Kn$) for large Kn. Another rarefaction-induced phenomenon in Poiseuille flow is the 'bi-modality' of the temperature profile, i.e. the temperature is minimum at the channel centerline,

[†]This chapter is an extended version of the paper (Journal of Fluid Mechanics): Alam, M., Mahajan, A., & Shivanna, D. (2015) "On Knudsen-minimum effect and temperature bimodality in a dilute granular Poiseuille flow", vol. 782, pg. 99-126

with its maxima being located a few mean-free paths away from the center – this was originally predicted by Tij & Santos (1994) and was confirmed later via DSMC (direct simulation Monte Carlo) simulations (Mansour *et al.* 1997). The origin of the temperature bimodality has been attributed to the second-order correction terms in Kn and hence this phenomenon belongs to the non-NSF regime (Aoki *et al.* 2002).

Most granular flows of practical interest have Knudsen numbers larger than 0.01 (Goldhirsch 2003; Galvin *et al.* 2007; Gayen & Alam 2008; Khain *et al.* 2008; Forterre & Pouliquen 2008; Rao & Nott 2008; Rongali & Alam 2014; Saha & Alam 2014) and therefore it is of interest to know whether the well-known signatures of rarefaction effects in molecular gases hold in granular gases. The latter is characterized by inelastic dissipation which is known to lead to some unexpected behaviour (Pöschel & Luding 2001). Understanding the role of dissipation on rarefaction phenomena would help to formulate/test hydrodynamic-like theories and related boundary conditions for rarefied granular flows. Driven by this motivation, we focus on a simple flow configuration: the gravity-driven Poiseuille flow of a granular gas for which there is no study on the Knudsen-minimum effect, but the temperature bimodality has been studied theoretically (Tij & Santos 2004). We shall show, via simulation, that (i) the effect of dissipation on above two rarefied phenomena is non-trivial, (ii) the wall roughness has a crucial role on the Knudsen-minimum effect and (iii) the characteristic features of temperature bimodality are at variance with the theoretical analysis of Tij & Santos (2004).

The simulation method for the gravity-driven flow of smooth inelastic hard-disks in a channel is described in section 2.2 focussing on 'dilute' flows (the mean area fraction of particles being less than or equal to 0.01) for a range of Knudsen number ($O(0.001) \leq Kn \leq O(1)$). Section 2.3.1 describes the statistical steady state of simulation and section 2.3.2 gives the hydrodynamic fields of granular Poiseuille flow. The results on the mass-flow rate and the temperature profile are discussed in section 2.4 and section 2.5, respectively, as functions of the normal restitution coefficient (e_n), the wall roughness (β_w) and the Knudsen number (Kn). The conclusions are given in 2.6.1. The present results shed some light on the range of validity of the granular hydrodynamic equations as discussed briefly in 2.6.2.

2.2 Simulation Model for Granular Poiseuille Flow

The flow configuration consists of a collection of circular-disks flowing through a two-dimensional channel of width W and length L under the action of gravitational acceleration g which is acting along the positive x-direction, see Fig. 1(a). The channel is bounded by two rigid parallel walls at $y = \pm W/2$, and the flow is assumed to be periodic along the x-direction; the latter condition implies that a particle leaving the periodic boundary at $x = L$ is reentered through the opposite-end at $x = 0$ and vice versa (Mansour *et al.* 1997; Alam & Chikkadi 2010). As in the case of rapid granular flows (Goldhirsch 2003), the particles move around randomly and are modeled as inelastic smooth hard-disks (of diameter d and mass m) which interact via instantaneous binary collisions.

For smooth particles, the tangential velocity during a collision remains unchanged but the energy loss is manifested as a change in the normal component of the relative velocity via the

following collision rule:

$$\mathbf{c}'_{12}\mathbf{k} = -e_n(\mathbf{c}_{12}\mathbf{k}), \tag{2.1}$$

where $\mathbf{k}$ is the contact vector, $\mathbf{c}_1$ and $\mathbf{c}_2$ are the instantaneous velocities of disks 1 and 2, respectively, and $\mathbf{c}_{12} = \mathbf{c}_2 - \mathbf{c}_1$ is the relative velocity. The restitution coefficient e_n, the ratio between the post- and pre-collisional relative velocity between the colliding pair, is assumed to be a constant throughout the simulation.

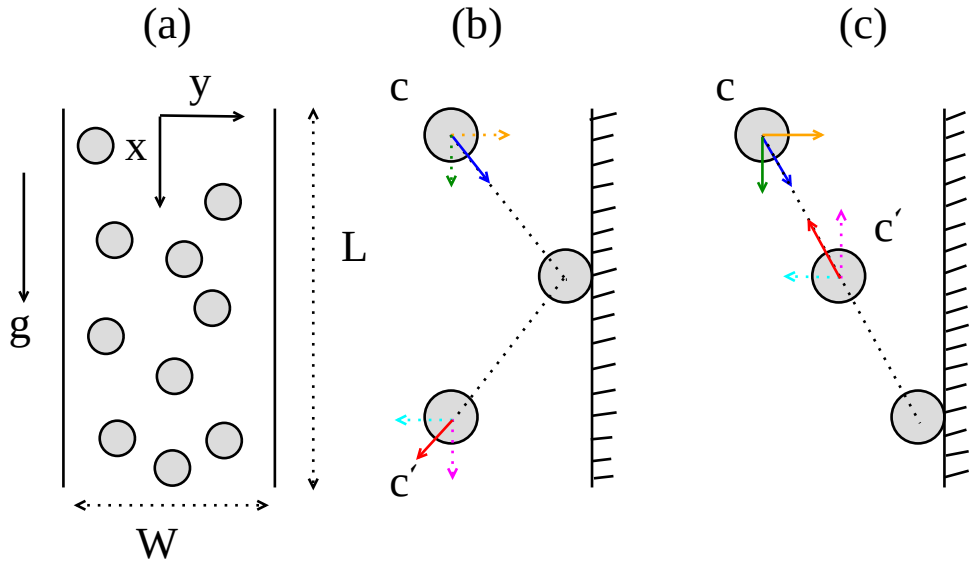

Figure 2.1: Schematics of (a) granular Poiseuille flow and (b-c) the rules for wall-particle collisions: (b) reflected/specular (smooth walls, $\beta_w = -1$) and (c) bounce-back collisions (rough walls, $\beta_w = 1$).

2.2.1 Algorithm

A general procedure of molecular dynamics involves step by step process of moving the system by an interval of δt along with accounting for the collisions which might occur in the time interval. All input parameters (eg. e_n, β_w) are assumed to be independent of time. In such cases of event-driven molecular dynamics, the system moves from one state to another with respect to events. The main assumption in event-based molecular dynamics is that at any instant only one collision occurs in an infinitesimal small interval of time. The framework of this event-based simulation constitutes the following steps [Allen & Tildesley (1989)]:

1. Setting up particle positions in the system [r_{ix},r_{iy},r_{iz}]
2. Initialization of particle velocities $[u_{ix}, u_{iy}, u_{iz}]$
3. Calculation of collision time of all particle pairs $(t_{12}, t_{13}...t_{1n}...t_{(n-1)n})$
4. Find the minimum of collision between particle pairs t_{ij}
5. Move the system to time $t = t_0 + t_{ij}$ by calculating the new positions and velocities of the system

6. Go to step 3

In such a procedure there are two types of events - particle-particle collision and wall-particle collision.

2.2.2 Domain modification

In a scenario as described above one needs to calculate the collision time between all the pairs of particles 12, 13, 14 ..., 23 ,24 ...., (n-1)n. The computational time required is of the order of the $O(N)$ per event processed. Such algorithms are efficient only for small number of particles.

To ease the load, the domain is divided into cells/regions and the collision partners of i is searched in cells neighboring the cell containing particle i (Allen & Tildesley 1989). For example, in 2D case, particles in 8 neighboring cells and the cell in which the particle is present is to be looked into as shown in Fig. 2.2.

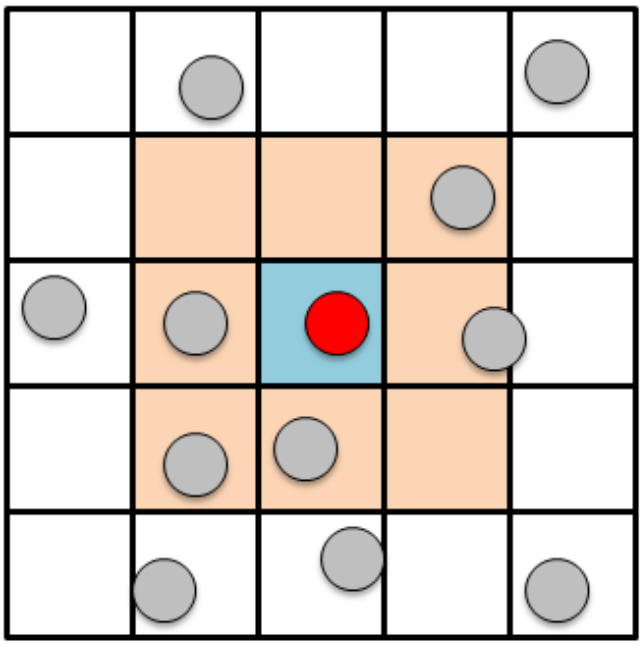

Figure 2.2: Schematic of cell division in 2D system

This reduces the computational load to $O(logN)$ per one processed event (Lubachevsky (1991)) for a system with all peroidic boundaries. Using such schemes, the following are considered as events while simulating Poiseuille flow - (i) particle-particle collision, (ii) cell-crossing and (iii) wall-particle collision. In order to implement this scheme efficiently a separate array-list is required, which contains information regarding the particles, the cell to which they belong, and their neighbors. Though this is computationally burdensome, it is better than the conventional method where one moves the whole system event by event.

2.2.3 Collision time calculation

Consider two particles of same diameter d at distances r_1 and r_2. At any time t, for the collision to occur the minimum distance between the particles must be equal to the particle diameter.

$$\vec{r}_1(t) - \vec{r}_2(t) = d. \tag{2.2}$$

$\vec{r}_2$ can be written in terms of $\vec{r}_1$

$$\vec{r}_2(t) = \vec{r}_1(t_0) + \vec{c}_{12}t_{12}. \tag{2.3}$$

Substituting Eq. (2.3) in (2.2) and squaring both sides, we get

$$[\vec{r}_{12} + (t_{12}\vec{c}_{12})]^2 = d^2. \tag{2.4}$$

The above equation is quadratic in t_{12} whose roots are given by:

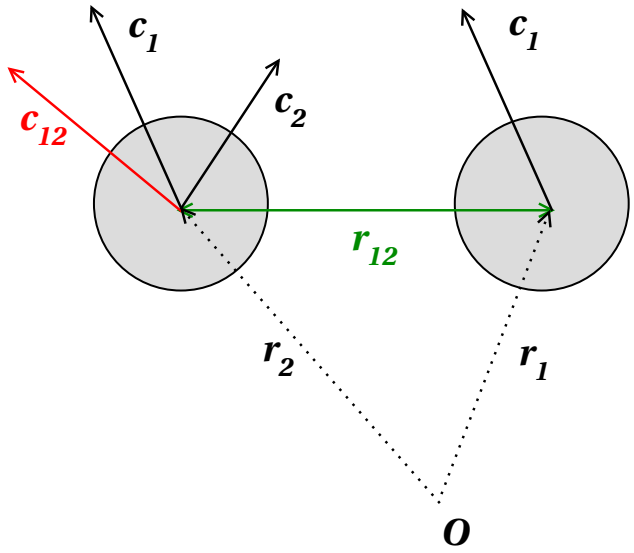

Figure 2.3: Vector construction showing condition for the particles to collide

$$t_{12} = t_0 + \frac{(-\vec{c}_{12}.\vec{r}_{12}) \pm \sqrt{(\vec{c}_{12}.\vec{r}_{12})^2 - \vec{c}_{12}^2(\vec{r}_{12}^2 - d^2)}}{\vec{c}_{12}^2}. \tag{2.5}$$

These roots can be real or complex; if real, it can be positive or negative. In order to eliminate the complex and negative roots and zero down to the minimum time of collision certain conditions are imposed. The particles can be moving parallel to each other, away from each other or towards each other. The collisions occur when particles move towards each other. To find out the the condition for such a situation a vector construction is shown in FIg. 2.3. The red line represent c_{12} and the green line represents r_{12} which are the resultants of the individual velocity and position vectors of particle 1 and 2. It can be seen that for the particles to be moving towards each other, the dot product $\vec{c}_{12}.\vec{r}_{12} < 0$. Further to eliminate complex root, Eq.(2.5) must satisfy the rule of discriminant. When all the above conditions are fulfilled two real roots are obtained. The larger root is neglected as the particles are impenetrable while the smaller

root is chosen.

2.2.4 Particle-level boundary condition

In addition to particle-particle collisions, the particles collide with two rigid walls, see Figs. 2.1(*b*,*c*), and hence their post-collisional velocities are likely to be affected depending on the bulk 'roughness' of the walls. Assuming that the walls are rigid and massive (compared to the mass of a particle), the model for particle-wall collisions is taken as (Liss *et al.* 2002; Alam & Chikkadi 2010):

$$c_x' = -\beta_w c_x \quad \text{and} \quad c_y' = -e_w c_y, \tag{2.6}$$

where c_i is the velocity component of the colliding particle along $i = x, y$ direction. For all simulations reported in this paper, we set $e_w = 1$ in 2.6, i.e. the magnitude of the normal component of the velocity of a disk remains unchanged upon collision with a wall. The blue and red arrows emanating from the centers of the colliding particles in Figs. 2.1(*b*,*c*) represent typical pre- and post-collisional velocities, respectively, for two limiting cases of particle-wall collisions as described below.

The change in the tangential velocity component (c_x) in (2.6) is parameterized by the 'wall-tangential' restitution coefficient β_w, which characterizes the bulk roughness of the wall (Rao & Nott 2008). The walls, which reflect all particles ($\beta_w = -1$) forward as in Fig. 2.1(*b*), do not incur any loss in the tangential momentum of incident particles and are called 'smooth' walls. On the other hand, the walls, which bounce back ($\beta_w = 1$) particles in the direction of their incidence as in Fig. 2.1(*c*), reverse the tangential momentum of incident particles, and are called 'perfectly rough' walls. While the perfectly rough walls ($\beta_w = 1$) represent the 'zero-slip' condition at walls, the perfectly smooth walls ($\beta_w = -1$) represent the 'free-slip' condition at walls (Chikkadi & Alam 2009). The intermediate case of $\beta_w = 0$, a linear combination of reflected ($\beta_w = -1$) and bounce-back ($\beta_w = 1$) conditions, corresponds to the maximum energy loss for particle-wall collisions (which is proportional to $\sim (1 - \beta_w^2)$ for $e_w = 1$). Other values of $\beta_w \neq \pm 1$ represent a 'mixed' boundary condition which may be thought of as an analog of the Maxwell's accommodation model (a fraction of wall-particle collisions is of specular-type and the rest being of bounce-back type) which is routinely used to model gas-surface interactions in kinetic theory(Cercignani 2000).

In summary, the walls are modelled as rough-frictional surfaces with the particle-wall collision rule being given by a two-parameter model (2.6). The limits of zero-slip and free-slip conditions are achieved in this model by varying the wall tangential-restitution coefficient (i.e. the 'bulk' roughness of the walls) from $\beta_w \to -1$ to $\beta_w \to 1$, respectively, see Figs. 2.6(*a*) and 2.6(*b*) in section 2.3.2.

2.2.5 Simulation method and averaging

A previously developed (Alam & Chikkadi 2010) event-driven molecular dynamics code based on Lubachevsky's (Lubachevsky 1991) algorithm has been modified to simulate the granular Poiseuille flow in the dilute regime as detailed in §2.2.1 - 2.2.4. In order to prevent the inelastic collapse which is likely to occur at small values of the restitution coefficient, we implemented

the TC-rule (Luding & McNamara 1998): if the collision time between particles is less than a critical time ($t_c \leq 10^{-9}$) then e_n is set to 1. The simulations are run for about 50000 collisions per particle and the data is collected after the system has reached a statistical steady state which is ascertained by monitoring the constancy of the average kinetic energy, $E(t) = \sum_{i=1}^{N}(c_{xi}^2 + c_{yi}^2)/2N$, per particle, see Fig. 2.4.

Since we are investigating rarefaction effects, the Knudsen number, the ratio between the mean-free path and a characteristic length-scale of the system, must be calculated. In Poiseuille-type flows, the mean free path (λ) varies across the channel width (see Fig. 2.5), and hence an average Knudsen number is defined via

$$Kn \equiv \langle Kn(y)\rangle_y = \frac{\langle \lambda(y)\rangle_y}{W}, \tag{2.7}$$

where $\langle\cdot\rangle_y$ represents a spatial-averaging over the channel width. To analyse rarefaction effects, a large range of (2.7) needs to be probed which can be achieved in two ways: (i) vary the channel width W/d and the number of particles N for specified values of the channel length L/d and the mean density,

$$\nu_{av} = \frac{\pi N}{4(L/d)(W/d)}, \tag{2.8}$$

or, (ii) for specified W/d and N, increase the channel length L/d such that ν_{av} is decreased which increases the mean-free path λ (and hence Kn increases) since λ is inversely proportional to density. In both cases, the mean density is kept small enough ($\nu_{av} \leq 0.01$) since we are focussing on a dilute granular gas. For all simulations reported here, we employed the first protocol to probe a range of $Kn \sim O(0.001) - O(1)$, see table 2.1; the same procedure was followed by Mansour *et al.* (1997) in the case of a molecular gas. The second protocol is computationally expensive especially at large Kn since the channel width must be kept at $W/d \sim O(10^3)$ or larger, but it was verified from a few case studies that the results reported here are robust irrespective of the protocol employed to vary the Knudsen number.

To extract hydrodynamic fields from simulations, we divide the channel into an array of vertical bins, each of width w ($w > d$, see table 2.1) and then carry out 'binwise' averaging by collecting data in each bin after reaching a statistical steady state. The volume fraction ν, stream-wise velocity U and granular temperature T in the i^{th} bin (located at $y = y_i$) are calculated from:

$$\nu(y) = \frac{\pi d^2}{4wL}\Big\langle \sum_{i=1}^{N} \delta(y - y_i)\Big\rangle, \tag{2.9}$$

$$U(y) = \frac{\Big\langle \sum_{i=1}^{N} c_{xi}(t)\delta(y - y_i)\Big\rangle}{\Big\langle \sum_{i=1}^{N} \delta(y - y_i)\Big\rangle}, \tag{2.10}$$

$$T(y) = \frac{\Big\langle \sum_{i=1}^{N} \mathbf{C}_i(t)\mathbf{C}_i(t)\delta(y - y_i)\Big\rangle}{2\Big\langle \sum_{i=1}^{N} \delta(y - y_i)\Big\rangle}, \tag{2.11}$$

where $\mathbf{C}_i(t) = \mathbf{c}_i(t) - U(y)\hat{x}$ is the peculiar velocity of particles, with $\hat{x}$ being the unit vector along x-direction, and $\langle\cdot\rangle$ represents the time-averaging over a large number of snapshots of the

system. For non-dimensionalization, the reference length, time and velocity scales are taken to be:

$$L_R = W, \tag{2.12}$$

$$t_R = \sqrt{\frac{W}{g}}, \tag{2.13}$$

$$U_R = \sqrt{gW}, \tag{2.14}$$

respectively, and the granular temperature (3.22) is scaled by gW.

2.3 Steady State and Hydrodynamic Fields

Given the mean density (area fraction) of disks ν_{av}, the width W and the length L of the channel, a collection of N identical smooth and rigid inelastic disks of mass $m = 1$ and diameter $d = 1$ are positioned randomly within the channel, and the disks are assigned random velocities (chosen from a normal distribution). With this initial configuration and wall-conditions, the material is allowed to flow under the action of gravity, and an event-driven algorithm (Lubachevsky 1991) is used to simulate the temporal dynamics of this system.

2.3.1 Steady state and Knudsen number

Figures 2.4(*a*-*b*) display the temporal variations of the total kinetic energy,

$$E(t) = \frac{1}{2N}\sum_{i=1}^{N} c_{xi}^2 + c_{yi}^2, \tag{2.15}$$

per particle. The data in panels (*a*) and (*b*) correspond to smooth- ($\beta_w = -0.95$) and rough-walled ($\beta_w = 0.95$) channels respectively; other parameters are the same as in Fig. 2.7 and listed in table 2.1.

W/d	**N**	**No of Bins** n_{bin}	**Bin width** $w = W/n_{bin}$	Kn ($\beta_w = -0.95$)	Kn ($\beta_w = 0.95$)	Kn ($\beta_w = 0$)	Kn ($\beta_w = 0$) ($e_n = 0.99$)
5497.78	35000	1374	4d	0.001	0.00075	–	–
1413.71	9000	353	4d	0.012	0.006	0.0085	0.0127
942.48	6000	325	4d	0.027	0.012	0.016	0.0245
392.70	2500	98	4d	0.15	0.043	0.055	0.056
157.08	1000	39	4d	0.526	0.14	0.185	0.192
62.83	400	15	4d	2.19	0.33	0.45	0.46
23.56	150	19	1.2d	5.25	0.62	1.048	1.06
15.71	100	13	1.2d	6.99	0.75	1.47	1.47

Table 2.1: Parameters used in simulations to vary the mean Knudsen number (2.7) for the mean density $\nu_{av} = 0.01$, channel length $L/d = 500$ and restitution coefficient $e_n = 0.9999$. Refer to Figs. 2.7 and 2.14(a, b).

It is seen that $E(t)$ fluctuates around some statistical mean value after a transient period,

irrespective of the values of β_w and the mean Knudsen number Kn (2.7). In each panel, the initial period of transients continues till a few hundreds collisions per particle, beyond which the data is collected to calculate hydrodynamic fields and related coarse-grained quantities. For most simulations, we used a mean density (2.8) of $\nu_{av} = 0.01$ or less, and the Knudsen number was changed by varying the width of the channel (W/d) and the number of particles N by keeping the channel length (L/d) fixed (Protocol 1, see section 2.2.5). Since the hydrodynamic fields vary across the wall-normal direction y (see below), the channel is partitioned into a number of bins (n_{bin}) parallel to the flow-direction x, each of width $w = W/n_{bin}$.

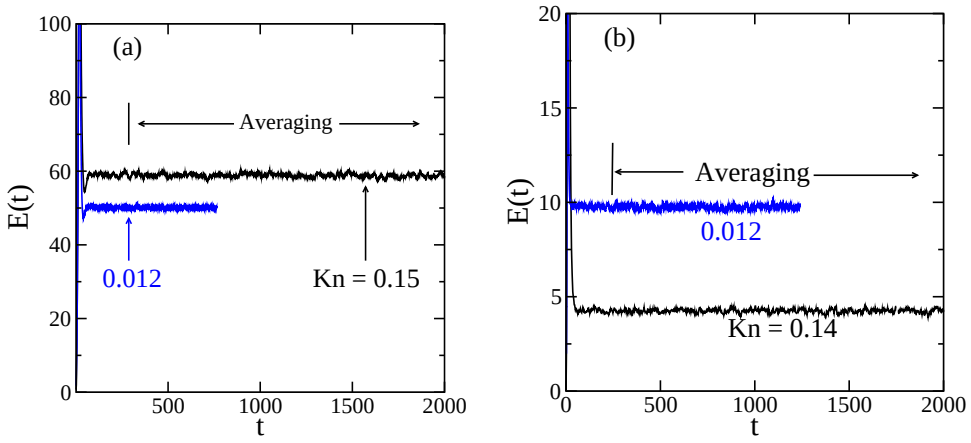

Figure 2.4: Evolution of kinetic energy, (2.15), versus time for (a) $\beta_w = -0.95$ (smooth wall) and (b) $\beta_w = 0.95$ (rough wall). The system reaches a statistical steady state when $E(t)$ fluctuates around some mean value; the vertical line in each panel marks an approximate time at which data is collected for averaging. The mean density is $\nu_{av} = 0.01$ and the restitution coefficient is $e_n = 0.9999$, and the parameter combinations of $(W/d, N)$ for different Kn are listed in table 2.1.

Table 2.1 provide details on the system parameters used to vary the average Knudsen number (2.7) as well as the number of bins used for averaging. The 'bin-wise' averaging procedure has been described in section 2.2.5. Two values of Kn marked in each panel of Fig. 2.4 correspond to different combinations of $(W/d, N)$ which are given in table 2.1.

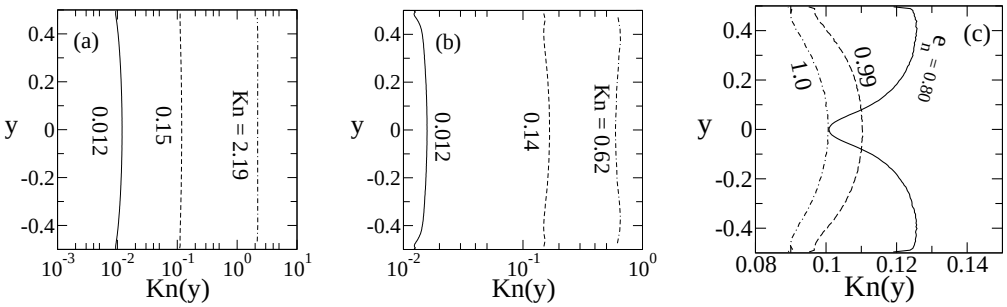

Figure 2.5: (a,b) Variations of local Knudsen number $Kn(y)$ across the channel width for (a) smooth $(\beta_w = -0.95)$ and (b) rough $(\beta_w = 0.95)$ walls, with parameter values as listed in table 2.1. (c) Variation of $Kn(y)$ for parameter values as in Fig. 2.10(b).

The cross-stream variations of the local Knudsen number $Kn(y)$ are shown in Figs. 2.5$(a$-$c)$. In panels (a) and (b), three profiles of $Kn(y)$ are plotted for different combinations of $(W/d, N)$,

resulting in different values of the mean Knudsen number; other parameter values are as in Figs. 2.4(a-b). Clearly, the local Kn varies along the wall-normal direction, albeit modestly, for both smooth- (panel a) and rough-walled (panel b) channels. The modulations of $Kn(y)$ become stronger when the restitution coefficient (e_n) is decreased, see panel (c) for which the parameter combinations of $(W/d, N)$ were chosen such that $Kn = \langle Kn(y) \rangle \approx 0.1$ as in Fig. 2.10(b).

2.3.2 Hydrodynamic profiles in granular Poiseuille flow

For the present system the statistical steady state corresponds to a "non-equilibrium" steady state for which the stream-wise velocity (U), volume fraction (ν) and granular temperature, T, remain invariant in time, having spatial variations along the wall-normal direction (y). Typical velocity and density profiles are shown in Fig. 2.6 for flows in smooth- ($\beta_w = -0.95$, first column) and rough-walled ($\beta_w = 0.95$, second column) channels, with parameter values as in Fig. 2.7. As expected, the velocity profiles remain symmetric about the channel centerline $y = 0$. It is clear from Fig. 2.6(a) that there is a large slip velocity when the channel walls are smooth ($\beta_w = -0.95$), and the magnitude of the slip velocity increases with increasing Kn and so does the centerline velocity.

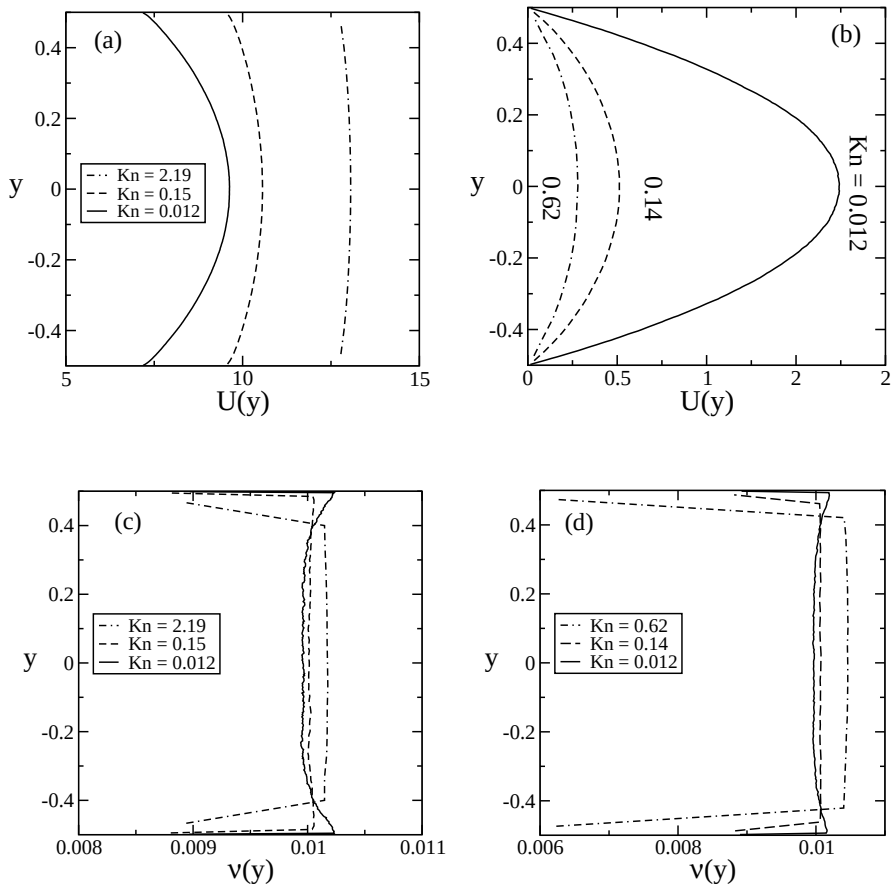

Figure 2.6: Profiles of (a,b) the streamwise velocity and (c,d) the density for flows in smooth-walled ($\beta_w = -0.95$, left column) and rough-walled ($\beta_w = 0.95$, right column) channels. Other parameter values are listed in table 2.1.

In contrast, the slip velocity remains finite but small when the walls are rough ($\beta_w = 0.95$,

Fig. 2.6*b*) compared to that for smooth-walled channels; although there is no discernible change in the slip velocity with increasing Kn, the centerline velocity (and hence the average velocity as well as the flow rate) decreases markedly with increasing Kn. Collectively, panels (a,b) confirm that the slip velocity can be changed from nearly zero to some large value by changing the wall-roughness parameter β_w from 1 to -1. The density profiles in Figs. 2.6(c,d) suggest that the wall-normal variations of density in the 'bulk' (around the centerline $y = 0$) of the channel remain relatively small (but finite) for both smooth and rough walls for elastic collisions ($e_n = 1.0$). On the other hand, for a given wall-roughness β_w, increasing the Knudsen number from the continuum limit ($Kn \sim 0$) to the rarefied regime ($Kn \sim O(1)$) makes the density variation relatively lesser (i.e. more homogeneous) in the bulk of the channel. For a specified Kn, increasing the inelastic dissipation (i.e. decreasing e_n) ensures discernible density modulations across the channel width as discussed in section 2.4 (see Fig. 2.10*b* in the main text) – this is dubbed 'dissipation-induced' clustering.

2.4 Results on Knudsen Paradox: Rarefaction ($Kn \neq 0$) Versus Dissipation ($e_n \neq 1$)

The effect of inelastic dissipation on the microscopic (i.e. velocity distribution functions and two-point density and velocity correlations) and macroscopic fields (hydrodynamic profiles, slip velocity, rheology and density waves) of gravity-driven granular Poiseuille flow have been investigated in previous works (Chikkadi & Alam 2007, 2009; Alam *et al.* 2009; Alam & Chikkadi 2010) for a range of densities. It must be noted that the above simulation works were carried out in a channel of width $W/d < 100$, and the Knudsen number was of order one [$Kn \sim O(1)$] in the dilute regime and hence the rarefaction effects were not studied. On other hand, the focus of the present work is to understand the role of inelastic dissipation on two well-known rarefaction effects in the gravity-driven Poiseuille flow of a dilute gas: (i) the Knudsen-minimum phenomenon (section 2.4) and (ii) the bimodal shape of the temperature profile (section 2.5).

The dimensionless mass-flow rate is calculated from:

$$Q = \frac{1}{\nu_{av} W \sqrt{gW}} \int_{-1/2}^{1/2} \nu(y) U(y) \mathrm{d}y, \tag{2.16}$$

where $U(y)$ and $\nu(y)$ are the streamwise velocity and density respectively.Equation (2.16) represents the mass flow rate per unit width of the channel, since the length scale used is the width of the channel (W) and the velocity scale is $\sqrt{gW}$. In the dilute limit ($\nu \to 0$), the mass flow rate Q is likely to depend on (i) the Knudsen number Kn, (ii) wall-roughness β_w and (iii) the restitution coefficient e_n which we discuss separately in the following subsections.

2.4.1 Effect of wall-roughness in the elastic limit: $Q(Kn, \beta_w, e_n \approx 1)$

The variation of the flow rate Q with Knudsen number Kn is shown in Fig. 2.7 for a range of wall roughness [$\beta_w \in (-0.95, 0.95)$] in the elastic limit ($e_n = 0.9999$), with a mean density of

$\nu_{av} = 0.01$; the results for the case of perfectly elastic collisions ($e_n = 1$) are almost identical with those of $e_n = 0.9999$, see the open circles in Fig. 2.7 for $\beta_w = -0.9$. As discussed in section 2.2.5, the range of Kn (2.7) in this Fig. has been achieved by varying the channel width W/d and the number of particles N which are listed in table 2.1. Focussing on the near-continuum limit ($Kn \to 0$) of all curves in Fig. 2.7, we find that, irrespective of the value of the wall-roughness β_w, the flow rate decreases with increasing Kn (for $Kn < 0.01$) which follows from Navier-Stokes hydrodynamics (Cercignani 2000; Cercignani & Daneri 1963). On the other hand, for any specified value of Kn, Fig. 2.7 also indicates that the mass-flow rate decreases with increasing wall-roughness ($\beta_w > -1$). This is because the smoother walls ($\beta_w \to -1$) ensure a larger slip velocity (see below), leading to a higher flow-rate compared to that in rough-walled channels ($\beta_w \to 1$).

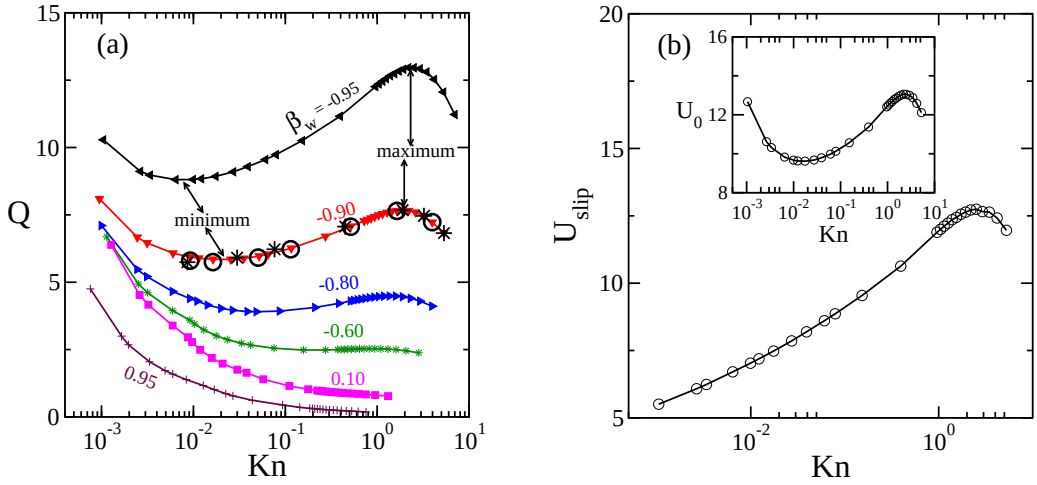

Figure 2.7: (a) Effect of wall-roughness (β_w) on the variation of mass-flow rate (Q) with average Knudsen number (Kn) for a restitution coefficient of $e_n = 0.9999$. The mean density is $\nu_{av} = 0.01$ and the channel length is $L/d = 500$; the open black circles represent the data for perfectly elastic collisions ($e_n = 1$) with a wall-roughness of $\beta_w = -0.9$ and a channel-length of $L/d = 500$, while the star-symbols represent the data for $e_n = 1$ in a longer channel of length $L/d = 1000$. (b) Variations of the slip-velocity (main panel) and the centerline velocity (inset) with Kn for flows through a smooth-walled ($\beta_w = -0.95$) channel. The range of Kn is obtained by varying the channel width W/d and the number of particles N as listed in table 2.1.

Returning to the dependence of Q on Kn, we note from Fig. 2.7 that the flow-rate decreases monotonically with increasing Kn for channels with a wall-roughness of $\beta_w > -0.6$. In contrast, for flows in relatively smooth-walled channels (see the top three curves in Fig. 2.7), the flow-rate varies 'non-monotonically' with Kn. More specifically, for the case of $\beta_w = -0.95$ (black curve), we find that the flow rate decreases with increasing Kn, reaches a minimum at $Kn \approx 0.01$, then increases by reaching a maximum at $Kn \approx 2.5$ and finally decreases again with further increase in Kn. The flow-rate curves for $\beta_w = -0.9$ and -0.8 remain qualitatively similar to that for $\beta_w = -0.95$, but the locations of $Q_{\min}$ and $Q_{\max}(Kn \neq 0)$ shift to larger and smaller values of Kn respectively. For all data in Fig. 2.7 the channel length is set to $L/d = 500$, except for the star-symbols which represent additional data for $e_n = 1$ with a larger channel length of $L/d = 1000$; this confirms that the overall shape of Q-curves does not depend on the length

of the channel. The degree of non-monotonicity of the Q-curves is quantified in terms of the difference between the local maximum and minimum of Q,

$$\triangle Q = Q_{\max}(Kn \neq 0) - Q_{\min}, \tag{2.17}$$

To understand the origin of non-monotonic Q-curves in Fig. 2.7, we probe the slip-velocity

$$U_{slip} \stackrel{def}{=} \frac{1}{2}\left(U(bin = 1) + U(bin = last)\right), \tag{2.18}$$

which is defined as the average of the streamwise velocities in two bins adjacent to stationary walls (see the velocity profiles in Figs. 2.6(a) and 2.6(b)). The variation of U_{slip} (2.18) with Kn is displayed in Fig. 2.7(b) for a wall-roughness of $\beta_w = -0.95$. It is seen that U_{slip} increases with increasing Kn, reaches a maximum at $Kn \sim 2$ and then starts decreasing with further increasing Kn. This maximum slip velocity seems to be responsible for the local maximum in the flow rate at $Kn \sim 2$ for the case of $\beta_w = -0.95$ (see the topmost black curve in Fig. 2.7). Interestingly the centerline velocity U_0, displayed in the inset of Fig. 2.7(b), follows the same non-monotonic trend with Kn as that of the flow rate Q. This is due to the fact that U_0 is a measure of the average velocity through the channel since the density variations across the channel (see Figs. 2.6c and 2.6d) at any Kn remains small for $e_n \to 1$.

2.4.2 Effects of inelastic dissipation ($e_n < 1$) and rarefaction ($Kn > 0$): the phase diagram

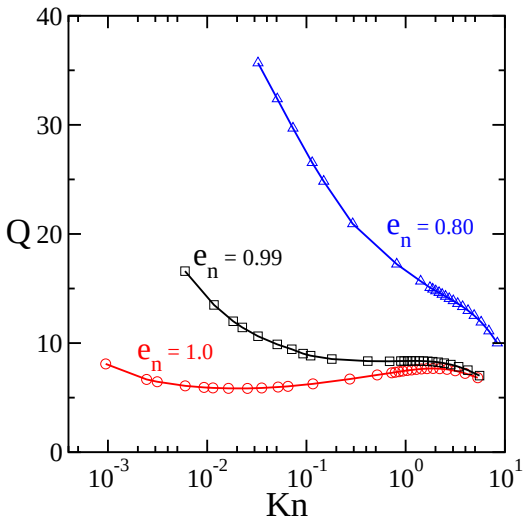

Figure 2.8: Effect of restitution coefficient e_n on Q for a wall-roughness of $\beta_w = -0.9$, with $e_n = 1$ (red circles), 0.99 (black squares) and 0.8 (blue triangles). Other parameter values are as in Fig. 2.7 as listed in table 2.1.

The effect of inelastic dissipation on the mass-flow rate Q can be ascertained from Fig. 2.8 which compares three Q-curves for $e_n = 1.0$ (red circles) , 0.99 (black squares) and 0.8 (blue

triangles). For all cases, the wall-roughness is set to $\beta_w = -0.9$ such that $Q(Kn)$ is non-monotonic in the elastic limit ($e_n = 1.0$) as indicated by the red-circled curve. In contrast, the black-squared curve for $e_n = 0.99$ indicates that $Q(Kn)$ decreases sharply up-to $Kn \approx 0.2$, and there is a plateau at around $Kn = O(1)$, beyond which $Q(Kn)$ decreases again with increasing Kn. Decreasing the restitution coefficient to $e_n = 0.8$ (blue-triangles curve) makes $Q(Kn)$ a monotonically decreasing function of Kn. The decrease of $Q(Kn)$ with increasing Kn becomes sharper with further decrease of e_n (not shown). The regions on the left and right of the broken line (marked with diamonds) in Fig. 2.9 represent the regimes of 'non-monotonic' ($\triangle Q > 0$) and 'monotonic' ($\triangle Q = 0$) mass-flow rates respectively. We conclude from this phase-diagram that the Knudsen-minimum effect is absent in granular Poiseuille flow (i) for $e_n < 0.989$, irrespective of the value of the wall-roughness, and (ii) for relatively rougher walls with $\beta_w > -0.6$ at any e_n.

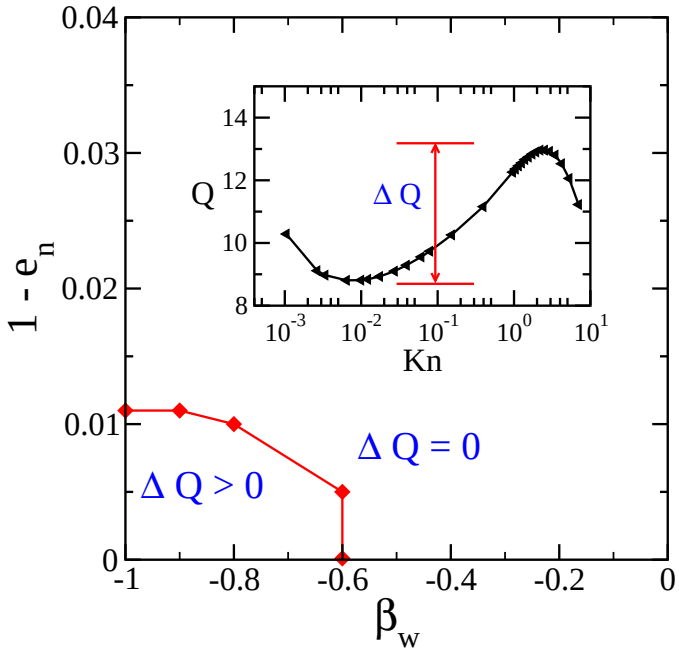

Figure 2.9: Phase-diagram in the $(\beta_w, 1 - e_n)$-plane, delineating the regions of non-monotonic ($\triangle Q > 0$) and monotonic ($\triangle Q = 0$) mass-flow rates; the inset shows the definition of $\triangle Q$, eqn. (2.17), with representative data for $e_n = 0.9999$ and $\beta_w = -0.95$. Other parameter values are as in Fig. 2.7 as listed in table 2.1.

2.4.3 Role of Knudsen number and the anomalous variation of slip velocity

To understand the dependence of $Q(Kn, e_n)$ on Kn for specified e_n, we show the variations of the slip velocity U_{slip} and the centerline velocity U_0 with Kn, respectively, in the main panel and the inset of Fig. 2.10(a) for $e_n = 0.8$ and 1.0. For this parameter combination, U_{slip} increases with increasing Kn for elastic ($e_n = 1$) particles, however, it follows a completely opposite trend when the restitution coefficient is reduced to $e_n = 0.8$. The latter finding is dubbed *anomalous* since U_{slip} is known to increase with increasing Kn in a molecular gas. In

any case, the decrease of U_{slip} with increasing Kn is responsible for the continual decrease of Q with increasing Kn for moderately dissipative ($e_n = 0.8$) particles in smooth-walled channels. Figure 2.10(a) further indicates that increasing dissipation results in larger values for both the slip velocity U_{slip} (main panel) and the centerline velocity U_0 (inset), and hence the flow rate would increase with decreasing e_n at any Kn as we found in Fig. 2.8. It is noteworthy that the latter effect becomes more prominent as Kn decreases progressively towards zero which can be explained as follows. The density profiles in Fig. 2.10(b) confirm a significant density-variation across the channel-width for $e_n = 0.8$ (blue-solid line) in comparison to nearly flat density profiles for $e_n = 0.99$ (black dot-dashed line) and 1.0 (red-dashed line); the Knudsen number is set to $Kn \approx 0.1$ for three data sets. Overall, the particles tend to migrate towards the channel centerline where the shear rate is low (and vice versa) with increasing dissipation, leading to the formation of particle-rich and particle-depleted regions near the centerline and the walls respectively. The relatively particle-depleted regions near the walls for $e_n = 0.8$ imply a more rarefied regime, resulting in an increased slip velocity with decreasing e_n for specified Kn. This finding of 'transverse-clustering' of particles (see Fig. 2.10(b)) with decreasing e_n, in conjunction with enhanced bulk velocities (Fig. 2.11(a)), would result in enhanced flow rate (2.16) in the same limit. (A related effect with decreasing e_n is the 'finite/measurable' normal stress differences that may also aid in enhancing the mass-flow rate, see the discussion in section §2.4.5) It must be noted, however, that the above argument of clustering-enhanced flow rate is strictly valid in the continuum limit ($Kn \to 0$) where the rarefaction effects can be neglected.

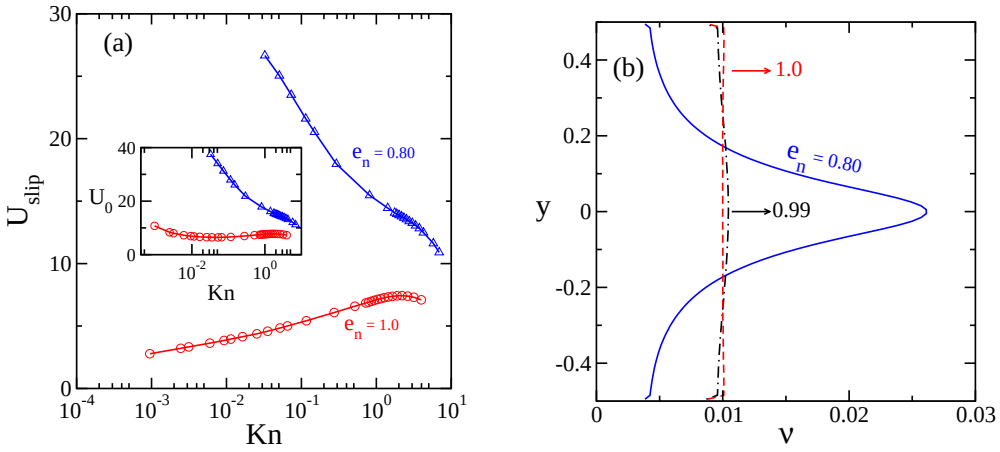

Figure 2.10: (a) Variations of slip velocity (main panel) and centerline velocity (inset) with Kn for $e_n = 0.8$ (blue triangles) and $e_n = 1.0$ (red circles). (b) Effect of e_n on density at $Kn \approx 0.1$, the blue-solid, black dot-dashed and red-dashed lines refer to $e_n = 0.8$, 0.99 and 1 respectively, in a channel of width $W/d = 549.77$ with $N = 3500$ particles. In all panels, the wall-roughness is $\beta_w = -0.9$ with other parameter values as in Fig. 2.7.

Returning to the effects of Knudsen number on the spatial distribution particles, we compare the density profiles for $Kn = 1.14$ (dashed line) and 0.14 (solid line) in Fig. 2.11(b). It is clear that, with other parameters being fixed, increasing Kn leads to a more homogeneous distribution of particles across the channel width, dubbed 'declustering'. The relatively homogeneous distribution of particles at larger Kn results in more collisions with the walls (compared to the

case for $Kn = 0.14$) and hence a larger energy loss near the walls, leading to a lower slip velocity with increased Kn at $e_n = 0.8$. Therefore, the competing effects of (i) the dissipation-induced clustering and (ii) the rarefaction-induced declustering along the wall-normal direction are responsible for the 'anomalous' decrease of U_{slip} with increasing Kn at lower values of e_n (the blue curve in Fig. 2.10a).

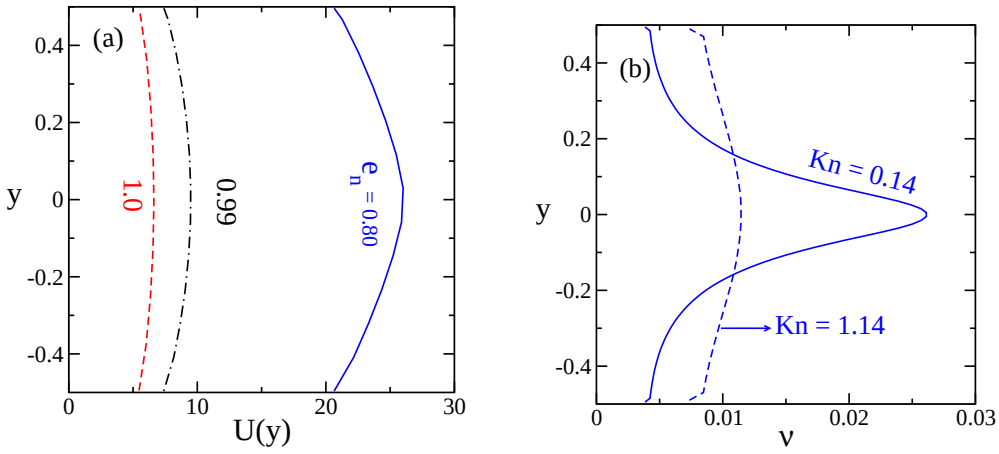

Figure 2.11: (a) Effect of e_n on velocity profiles at $Kn \approx 0.1$; the blue-solid, black dot-dashed and red-dashed lines refer to $e_n = 0.8$, 0.99 and 1 respectively, in a channel of width $W/d = 549.77$ with $N = 3500$ particles. (b) Comparison of the density profiles for $Kn = 0.14$ (solid line, $W/d = 549.77$ and $N = 3500$) and $Kn = 1.14$ (dashed line, $W/d = 196.35$ and $N = 1250$) at $e_n = 0.8$. In all panels, the wall-roughness is $\beta_w = -0.9$ with other parameter values as in Fig. 2.7.

2.4.4 Dissipation versus rarefaction: effects on density profile

The above issue of dissipation-induced 'clustering' (i.e. the density-inhomogeneity along the transverse/wall-normal direction) is also evident from a comparison of density profiles in Figs. 2.12(a) and 2.12(b). The corresponding temperature profiles are shown in Fig. 2.14, see the related discussion on temperature bimodality in section 2.5. It is clear from Figs. 2.12(a) and 2.12(b) that, for any specified e_n, increasing the Knudsen number makes the density profiles relatively homogeneous in the 'bulk' of the channel – this is dubbed 'rarefaction-induced' declustering. with the Knudsen number Kn for two values of the restitution coefficient; here, $\nu(0)$ is the density at the channel centerline and ν_{av} is the mean density. The curves for both $e_n = 1$ (black circles) and 0.99 (red squares) coincide with each other for $Kn \geq 0.2$, implying that dissipation plays no role on the bulk dynamics of density profiles for $Kn \geq 0.2$.

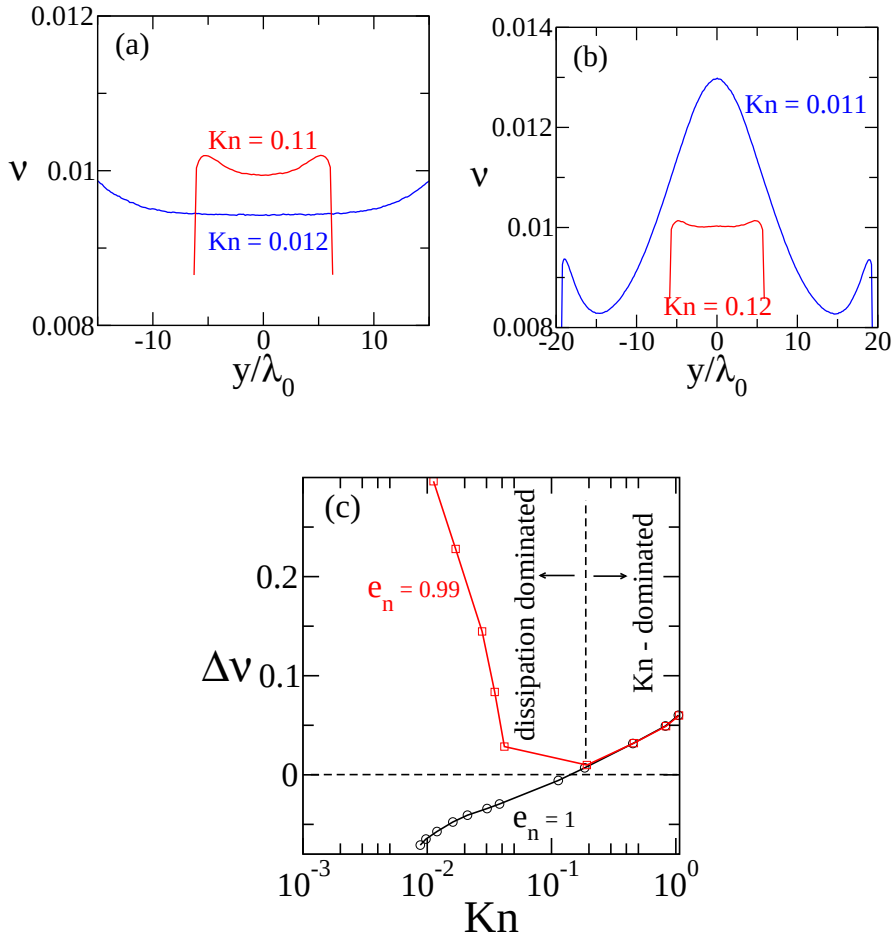

Figure 2.12: Profiles of density for (a) $e_n = 1.0$ and (b) $e_n = 0.99$, with parameter values as in Fig. 2.14. (c) Variation of the excess density, $\Delta\nu = (\nu(0)/\nu_{av} - 1)$, with Knudsen number.

It is clear that, for $e_n = 1$, there is a critical Knudsen number of $Kn \approx 0.2$ above/below which there is a net accumulation/depletion of particles at $y = 0$. Interestingly, even a small amount of dissipation ($e_n = 0.99$) leads to an overall accumulation of particles ($\Delta\nu > 0$) around the channel centerline at any $Kn < 0.2$, and the degree of particle accumulation ($\propto \Delta\nu$) increases with decreasing Kn for a given $e_n \neq 1$. Further decreasing the restitution coefficient (not shown) increases the value of the excess density $\Delta\nu$ at $Kn < 0.2$.

Figure 2.12(c) displays the variations of the 'excess' density at $y = 0$ (with respect to mean/average density),

$$\Delta\nu = \frac{\nu(0)}{\nu_{av}} - 1, \tag{2.19}$$

Based on these results, we conclude that the inelastic dissipation has a primary influence on the hydrodynamic density profiles at lower values of Kn. The vertical dashed line in Fig. 2.12(c) approximately demarcates the regions of 'dissipation-dominated' and 'rarefaction-dominated' flows.

2.4.5 Possible role of normal stress difference on flow rate

It is well-known in rarefied gas-dynamics (Kogan 1969) that the finite values of Knudsen number (Kn) give rise to non-zero normal stress difference which remains of infinitesimal magnitude in a molecular gas. In contrast, however, the inelastic dissipation makes the normal stress differences (Sela & Goldhirsch 1998; Saha & Alam 2014) finite and 'measurable'. This additional effect of inelasticity may have some impact on the macroscopic behaviour of Poiseuille flow (e.g. the mass-flow rate) as we discuss below. In Fig. 2.13, we compare the profiles of the 'scaled' first normal stress difference (Chikkadi & Alam 2009; Alam & Luding 2003, 2005*a*,*b*)

$$\mathcal{N}_1 = \frac{p_{xx} - p_{yy}}{p} = \frac{2(p_{xx} - p_{yy})}{(p_{xx} + p_{yy})} \sim (T_x - T_y), \tag{2.20}$$

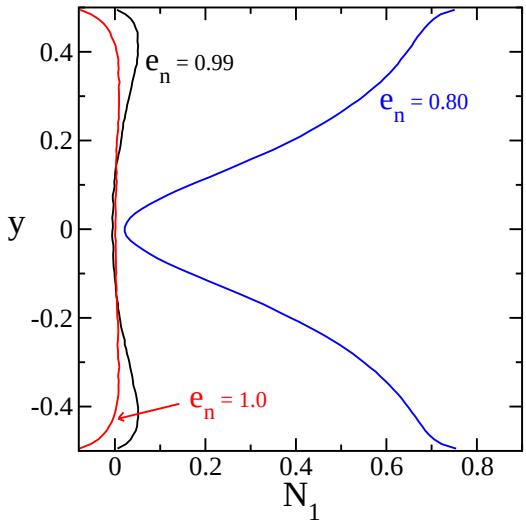

Figure 2.13: Effect of e_n on the first normal stress difference, $\mathcal{N}_1 = (p_{xx} - p_{yy})/p$, at $Kn \approx 0.1$. Other parameters are as in Fig. 2.10(b).

where $p_{ij} = \langle \nu C_i C_j \rangle$ and C_i is the peculiar velocity, see Eqn. (3.22); the Knudsen number is set to $Kn \approx 0.1$ as in the main panel of Fig. 2.10(b); It is clear that inelastic dissipation enhances the first normal stress difference across the channel width. Since (2.20) is also a measure of the temperature anisotropy ($T_x \neq T_y$), this implies that the fluctuation velocity levels along the flow direction are higher than that along the wall-normal direction as dissipation increases. The latter finding may partially be responsible for the enhanced flow-rate with increasing dissipation as found in Fig. 2.8.

2.5 Results on Bimodal Temperature Profile: Rarefaction or Dissipation Driven?

Here we characterize the temperature profiles in a dilute granular Poiseuille flow, and attempt to make a connection with the well-known 'bimodal' shape (Tij & Santos 1994), with a temperature minimum at the center of the channel and two local maxima positioned symmetrically away

from $y = 0$, in its molecular gas counterpart. The primary goal is to unveil the origin of the temperature bimodality in the granular Poiseuille flow. All results in this section are presented for $\beta_w = 0$, which corresponds to a *mixed boundary condition* with equal contributions from bounce-back ($\beta_w = 1$) and specular/reflected ($\beta_w = -1$) particle-wall collisions, but we have verified that the following observations hold for any $-1 < \beta_w < 1$. Figures 2.14(a) and 2.14(b) display the temperature profiles for the case of perfectly elastic ($e_n = 1$) and inelastic ($e_n = 0.99$) collisions respectively. The temperature has been normalized by its centerline value [$T_0 = T(y = 0)$] which is plotted against y/λ_0, where λ_0 is the centerline mean-free path. The corresponding density profiles are shown in Figs. 2.12(a,b).

Two curves in each panel represent data for channels of different widths that can be mapped to different values of average Knudsen number ($Kn \sim 0.01$ and 0.1, viz. Eq. 2.7; see table 1). For the case of perfectly elastic collisions ($e_n = 1$) in Fig. 2.14(a), it is seen that the temperature profile has a maximum at $y = 0$ for $Kn = 0.012$, but the one at $Kn = 0.11$ has a local minimum at $y = 0$, with two maxima being located symmetrically away from $y = 0$. Overall the temperature profile for $e_n = 1.0$ is unimodal at lower values of Kn and becomes bimodal at larger Kn. In contrast, for a granular gas ($e_n = 0.99$), the bimodal shape of the temperature profile persists even at lower values of $Kn \sim 0.01$ as confirmed in Fig. 2.14(b).

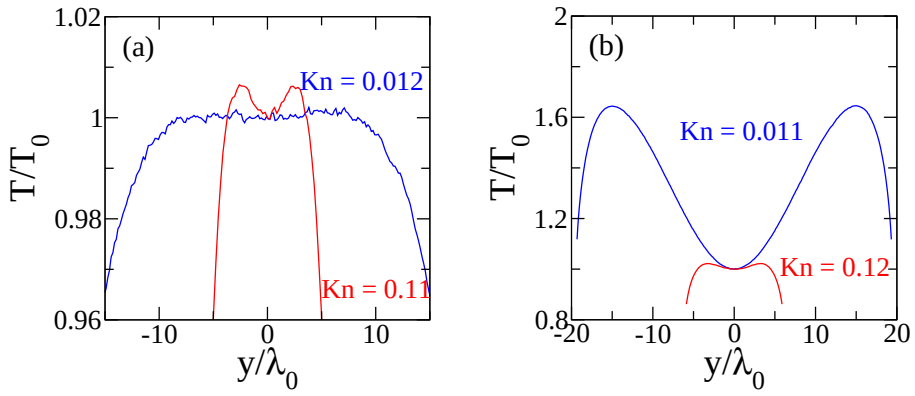

Figure 2.14: Temperature profiles at different Kn for (a) perfectly elastic ($e_n = 1$) and (b) inelastic ($e_n = 0.99$) particles; the parameter values are set to $\nu_{av} = 0.01$, $L/d = 500$ and $\beta_w = 0$ in both panels. While in panel (a) the Knudsen numbers of $Kn = 0.012$ and 0.11 are achieved with parameters of $(W/d, N) = (1178.09, 7500)$ and $(W/d, N) = (235.61, 1500)$ respectively, in panel (b) $Kn = 0.011$ and 0.12 correspond to $(W/d, N) = (1570.79, 10000)$ and $(W/d, N) = (235.61, 1500)$ respectively.

More importantly, the degree of bimodality [$\sim (T_{\max} - T_0)$, eqn. (2.21)] has increased markedly with decreasing Kn for $e_n = 0.99$. This seemingly opposite behaviour between $e_n = 1$ and $e_n = 0.99$ can be resolved if we know the origin of the temperature bimodality in granular/athermal Poiseuille flow.

2.5.1 Origin of temperature bimodality

The primary characteristic feature of the bimodal shape of the temperature profile, such as those in Fig. 2.14, is the 'excess' temperature ratio, $\triangle T$, which is defined as

$$\triangle T = \frac{(T_{\max} - T_0)}{T_0}, \tag{2.21}$$

where T_0 is the temperature at the channel centerline ($y = 0$) and $T_{\max}$ is the maximum temperature. Clearly, $\triangle T = 0$ and > 0 for unimodal and bimodal temperature profiles respectively. The larger the value of $\triangle T$, the larger is the deviation from an unimodal profile, and hence $\triangle T$ is also a measure of the degree of temperature bimodality. To find out whether there is indeed a local minimum of the temperature profile at $y = 0$, we need to evaluate its second derivative $T''(y = 0)$: the temperature has a local maxima or minima at $y = 0$ depending on whether

$$T''(0) \equiv \frac{\mathrm{d}^2 T}{\mathrm{d}y^2}(y = 0) \leq 0, \quad \text{or,} \quad T''(0) > 0, \tag{2.22}$$

respectively.

Figures 2.15(a) and 2.15(b) display the variations of $\triangle T$ and $T''(y = 0)$, respectively, with Knudsen number Kn. In each panel, the curves represent data for different restitution coefficients. The black-circled curves for $e_n = 1$ in panels a and b confirm that the temperature profile for elastically-colliding particles undergoes a transition from an unimodal ($\triangle T \approx 0$ and $T''(y = 0) \approx 0$) to a bimodal ($\triangle T > 0$ and $T''(y = 0) > 0$) shape at some small but finite value of $Kn = Kn_c \approx 0.01$. Therefore, the origin of temperature bimodality in the Poiseuille flow of a molecular gas is tied to the *rarefaction effect* (Tij & Santos 1994; Mansour *et al.* 1997) since it occurs at finite values of Knudsen number.

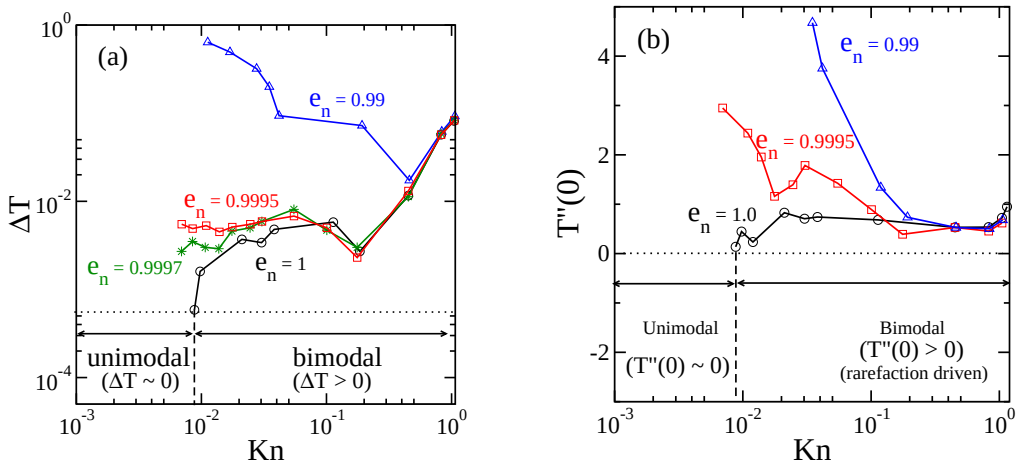

Figure 2.15: Variations of (a) excess temperature, $\triangle T$, and (b) $d^2T/dy^2(y = 0)$ with average Knudsen number $Kn = \langle Kn(y) \rangle$ for different restitution coefficients of $e_n = 1$ (black-circles), $e_n = 0.9995$ (red-squares), $e_n = 0.9997$ (green-stars) and 0.99 (blue-triangles). The parameter values are set to $\nu_{av} = 0.01$ and $\beta_w = 0$, with channel dimensions (for different Kn) being listed in table 2.1.

The red-squared lines in Figs. 2.15(a) and 2.15(b) indicate that both $\triangle T$ and $T''(0)$ are

positive for all $Kn > 0$ at $e_n = 0.9995$ (since the $\triangle T$-curve develops a plateau and does not seem to decrease as $Kn \to 0$ and $T''(0)$ increases in the same limit), implying that the corresponding temperature profile is bimodal. Further decreasing the restitution coefficient ($e_n = 0.99$, see the blue lines in both panels) enhances the values of both $\triangle T$ and $T''(0)$ markedly at lower values of $Kn < 0.1$. In contrast, we find from panels a and b that the effect of dissipation on both $\triangle T$ and $T''(0)$ diminishes with increasing Kn, and the respective curves for different e_n coincide at $Kn \sim O(1)$ and beyond. Collectively, therefore, Figs. 2.15(a) and 2.15(b) confirm that the inelastic dissipation is the driving factor for the genesis of temperature bimodality in the continuum limit of $Kn \to 0$, and the rarefaction effect prevails at large enough Kn.

2.5.2 The phase diagram: rarefaction versus dissipation

It is clear from Fig. 2.15(a) that the temperature profile remains bimodal ($\triangle T > 0$) for $e_n \leq 0.9995$ at any Kn. On the other hand, extrapolating the green-line (for $e_n = 0.9997$), marked by the star-symbols in Fig. 2.15(a), for small Kn yields $\triangle T = 0$ at $Kn_c \approx 0.007$, below which the temperature profile becomes unimodal. Therefore, the "unimodal-to-bimodal" transition would occur for a very small range of restitution coefficient $e_n \in (0.9997, 1)$ in the limit $Kn \to 0$. The above findings are summarized in Fig. 2.16 as a phase-digram in the $(Kn, 1 - e_n)$-plane. The red-line through circles represents a phase-boundary, to the left and right of which the temperature profile is unimodal and bimodal respectively.

Note that the region of unimodal temperature in the $(Kn,\, 1-e_n)$-plane is very small. In the bimodal region of the phase-diagram in Fig. 2.16, two distinct mechanisms compete with each other: (i) the temperature bimodality near the continuum limit ($Kn \sim 0$) is driven solely by inelastic dissipation, but (ii) the rarefaction-driven bimodality remains active beyond a critical Knudsen number $Kn > Kn_c(e) > 0$ as in a molecular gas. The latter mechanism would take over from the dissipation-driven mechanism at large enough Kn (for a given e_n) since the particle-wall collisions dominate over particle-particle collisions at large Kn and therefore the collisional dissipation is likely to have a minor role on the 'bulk' dynamics of the flow at sufficiently large Kn. These arguments suggest that there must be another phase-boundary in the $(Kn, 1 - e_n)$-plane that would demarcate (i) the dissipation-driven bimodality from (ii) the rarefaction-driven bimodality. This is marked by the blue-dashed line in Fig. 2.16, to the left and right of which the mechanisms (i) and (ii), respectively, are operative. The square symbols on this phase-boundary have been obtained from Fig. 2.15(b) as follows: each curve of $T''(0)$ is fitted via a polynomial in Kn and then we determine the value of Kn at which its slope, $d/dKn(T''(0))$, saturates approximately to zero (within 5%).

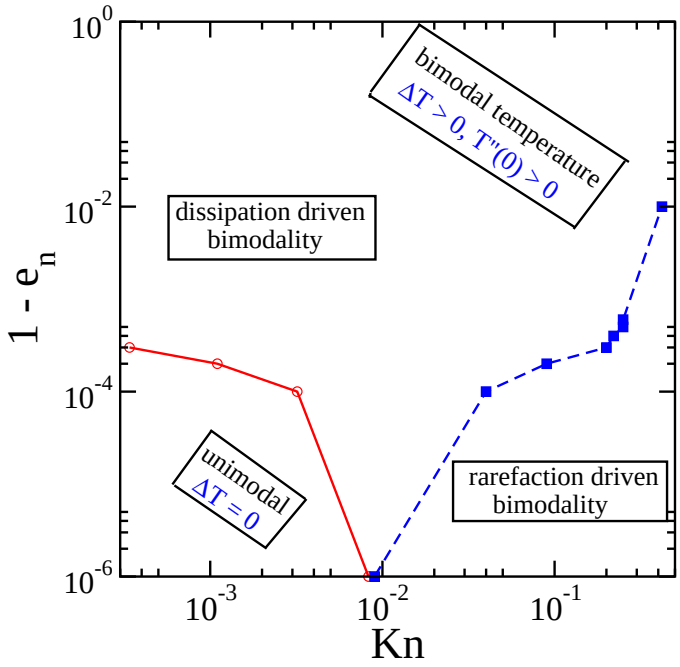

Figure 2.16: Phase diagram in the $(Kn, 1 - e_n)$-plane, delineating the regions of unimodal ($\triangle T = 0$) and bimodal ($\triangle T > 0$ and $d^2T/dy^2(y = 0) > 0$) temperature profiles. The blue-dashed line approximately splits the bimodal-regime into two parts: (i) rarefaction-induced and (ii) dissipation-induced bimodality. The parameter values are as in Fig. 2.14.

2.5.3 Excess temperature and its variation with e_n

Fig. 2.17(a) shows the temperature profiles at much lower values of e_n; these simulations have been carried out for $\nu_{av} = 0.01$ (panel a; $W/d = 400$, $L/d = 294.5$ and $N = 1500$). A clear distinction can be seen between theory (Fig. 2.17(b, c)) and simulations (Fig. 2.17(a)). The simulations show the extent of bimodality increases with increase in the dissipation of the system (see inset of Fig. 2.17(a)) whereas the theory predicts a complete opposite trend till $e_n = 0.5$ [Fig. 2.17(c)].

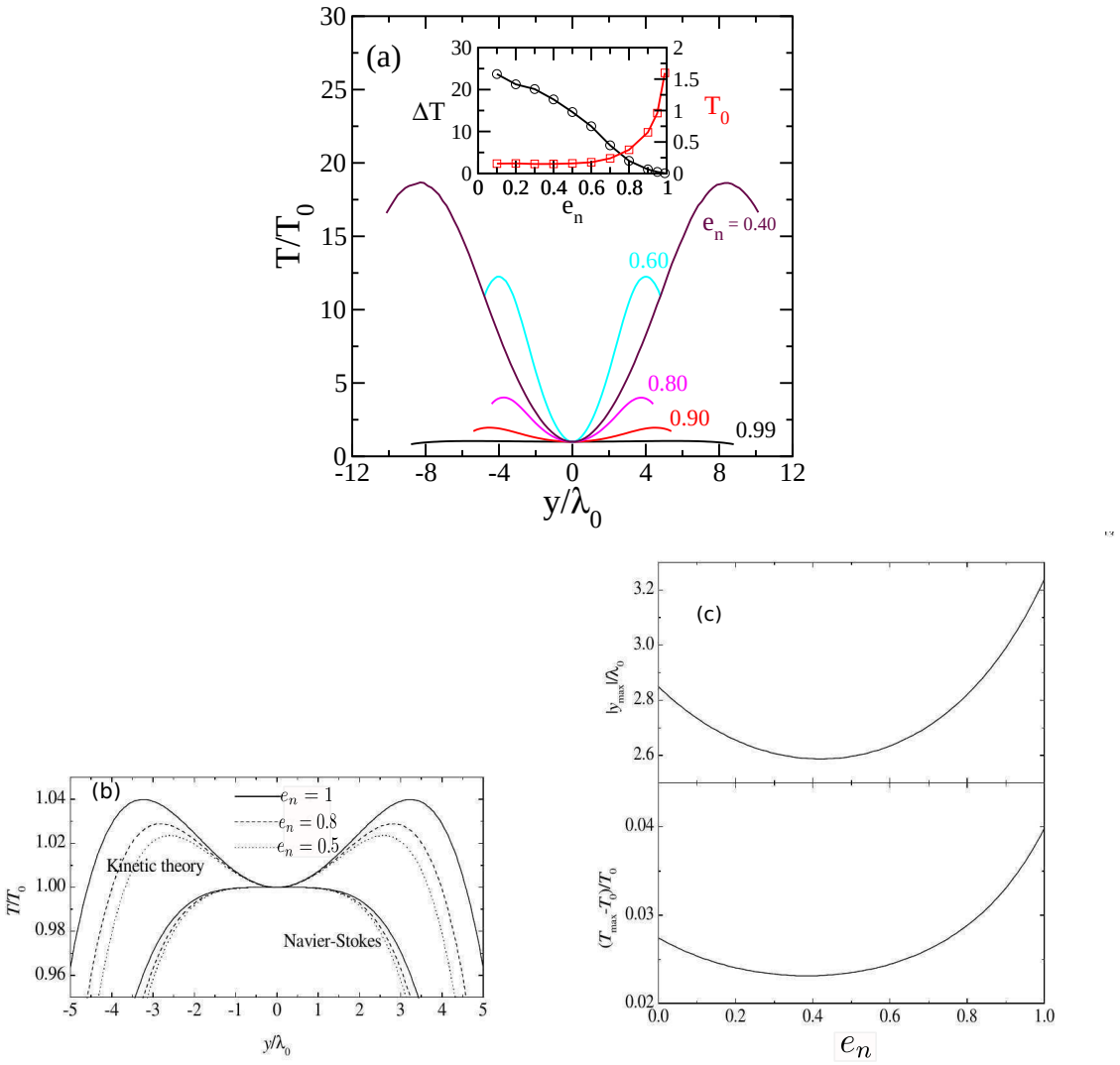

Figure 2.17: (a) Simulations showing the effect of restitution coefficient on temperature; the inset shows the variations of the excess temperature $\triangle T$ equation (2.21), denoted by black circles) and the centerline temperature T_0 (denoted by red squares) with e_n (b) Effect of restitution coefficient e_n on granular temperature profiles and (c) shows the variations of the excess temperature $\triangle T$ and distance at which T_{max} occurs with e_n (Tij & Santos (2004)). Parameter values are $\nu_{av} = 0.01$ ($W/d = 400$ and $L/d = 294.5$)

The inset of Fig. 2.17(a) indicates that the centerline temperature T_0 (marked by the red line) decreases with increasing dissipation ($\sim (1-e_n^2)$). The variation of the *excess* temperature ratio, $\triangle T$, (2.21), is also shown (marked by the black-circled line) as a function of e_n in the inset. It is clear that $\triangle T$ increases monotonically with decreasing e_n which implies that the degree of temperature bimodality becomes more pronounced with increasing dissipation/inelasticity. This finding is in contradiction with Tij & Santos (2004) who predicted that $\triangle T$ decreases with decreasing e_n from the elastic limit up-to a value of $e_n \sim 0.4$ and increases subsequently for $e_n < 0.4$ (see Fig. 2.17(c)).

2.5.4 Comparison of excess temperature with theory

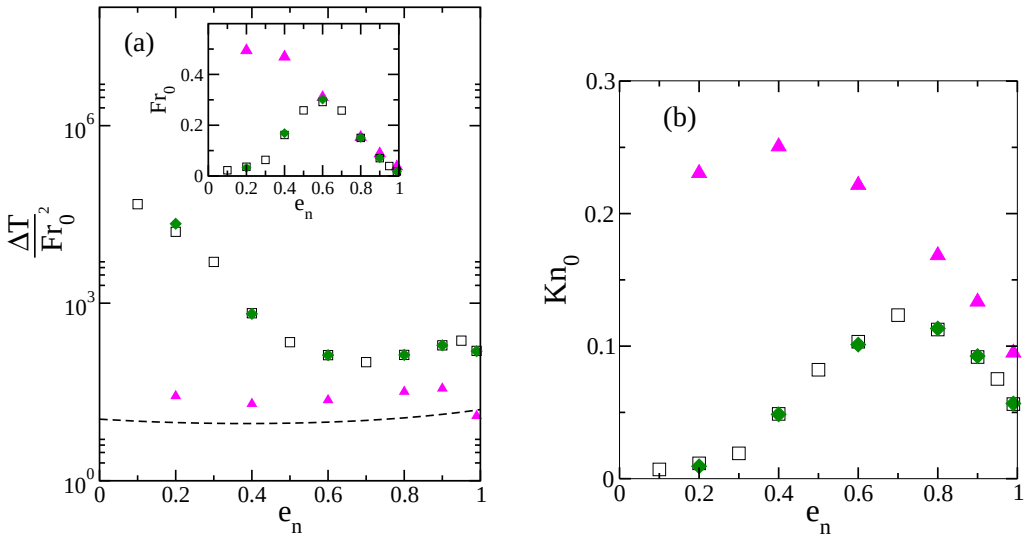

Figure 2.18: (a) Comparison between theory (dashed line - Tij & Santos (2004)) and simulation (symbols) for the normalized excess temperature $\triangle T/Fr_0^2$. Upper inset shows the variation of the centerline Froude number [Fr_0, Eqn. (2.25)] with e_n. (b) Variation of the centerline Knudsen number $Kn_0 = \lambda_0/W$ with restitution coefficient. Symbols refer to simulation data: squares ($\nu_{av} = 0.01$, $W/d = 400$), triangles ($\nu_{av} = 0.005$, $W/d = 400$) and diamonds ($\nu_{av} = 0.005$, $W/d = 800$).

Let us make a quantitative comparison of our simulation with the analysis of Tij & Santos (2004) who solved the inelastic Boltzmann equation (with a BGK-type collision model) subjected to a constant gravitational force and a stochastic (white noise) thermostat. The role of the stochastic thermostat was to heat the granular gas such that it compensates the loss of energy due to collisional cooling, yielding a 'uniform' state about which a Chapman-Enskog-type expansion was carried out by treating the body-force as a small parameter (which is proportional to the centerline Knudsen number Kn_0). Under these assumptions, they confirmed that while the Navier-Stokes equations (for a dilute granular gas) yield a temperature maximum,

$$\left(\frac{\partial^2 T}{\partial y^2}\right)_{y=0} = 0 \quad \text{and} \quad \left(\frac{\partial^4 T}{\partial y^4}\right)_{y=0} < 0, \tag{2.23}$$

at the channel centerline ($y = 0$), the incorporation of $O(Kn^2)$-corrections results in

$$\left(\frac{\partial^2 T}{\partial y^2}\right)_{y=0} > 0, \tag{2.24}$$

implying a local minimum at $y = 0$.

The major prediction of this theory (Tij & Santos 2004) is that the ratio between the excess temperature ratio $\triangle T$, (2.21), and the centerline Froude number,

$$Fr_0 = \frac{\tilde{g}\tilde{\lambda}_0}{\tilde{v}_0^2} = \frac{Kn_0}{2T_0}, \tag{2.25}$$

depends only on the restitution coefficient:

$$\frac{\triangle T}{Fr_0^2} = \frac{\mathcal{A}_2^2(e_n)}{4\mathcal{A}_4(e_n)} + O\left(Fr_0^2\right). \tag{2.26}$$

The quantity (2.26) is called 'normalized' excess temperature which is compared with simulation data in Fig. 2.18(a) as a function of e_n. The corresponding variation of Froude number (2.25) is displayed in the upper inset. The data set, denoted by squares, refer to simulations for $\nu_{av} = 0.01$ (with $W/d = 400$). These simulation data shows a disagreement with theory with $\triangle T$ decreasing with decrease in the dissipation.

The variation of the centerline Knudsen number Kn_0 $(= \lambda_0/W)$ with e_n is shown in Fig. 2.18(b). Note that Kn_0 is of $O(0.1)$ or less for the data set (squares) and approaches to 0.05 at $e_n \to 1$, again increases to a maximum of $Kn_0 \approx 0.12$ at $e_n = 0.7$ and decreases monotonically with further decrease of e_n. Recall that an inbuilt assumption of the theory is $Kn_0 << 1$ and $Fr_0 << 1$ which is not satisfied for any of the data sets shown in Fig. 2.18(a).

2.5.5 Possible role of axial inhomogeneities

For the data set, denoted by squares, in Fig. 2.18(b), the centerline Knudsen number Kn_0 increases initially as e_n is decreased, reaches a maximum and decreases thereafter. This implies that the granular gas becomes more rarefied around the channel centerline with decreasing e_n up-to $e_n \approx 0.7$, before entering into a lesser rarefied regime for $e_n < 0.7$. The critical e_n at which the above flow transition occurs is in fact tied to clustering of particles along the axial direction as we shall demonstrate below. For parameter values as in Fig. 2.17(a), the snapshots of the system for $e_n = 0.9$ and 0.2 are displayed in Figs. 2.19(a) and 2.19(b) respectively. The particle distribution appears homogeneous at $e_n = 0.9$, but there are considerable variations along both streamwise and lateral directions at $e_n = 0.2$. To better characterize the spatial organization of particles, the system is divided into $n_x \times n_y$ cells and the density (the area fraction of particles) is calculated in each cell and is stored as a matrix of size $n_x \times n_y$ from which the power spectrum is calculated using the fast Fourier transform (Liss *et al.* 2002; Alam *et al.* 2009). The coefficients $[a(k_x, k_y)]$ of the Fourier series for the coarse-grained density field.

$$a(k_x, k_y) \exp[i2\pi(k_x x/L + k_y y/W)], \tag{2.27}$$

are found and stored in a matrix X. The power spectrum $(\mathcal{P})$ of the density field is then calculated from

$$\mathcal{P}(k_x, k_y) = \frac{2X \cdot conj(X)}{(n_x n_y)^2}, \tag{2.28}$$

which is normalized by the size of the matrix to remove its dependence on the chosen mesh.

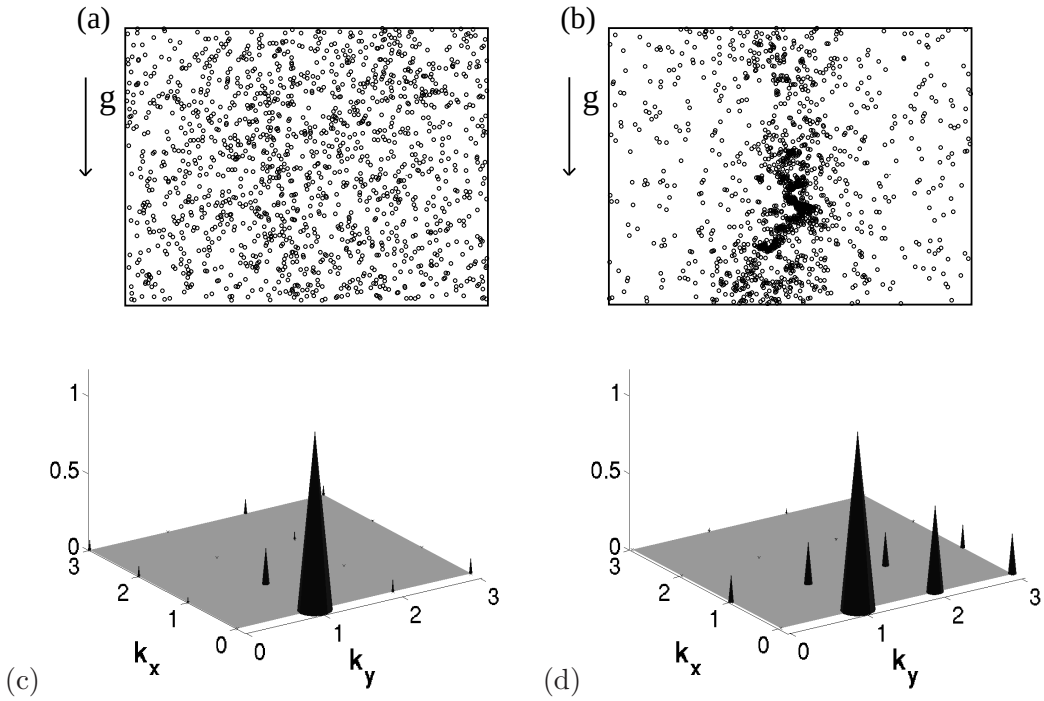

Figure 2.19: Snapshots of instantaneous particle positions for (a) $e_n = 0.9$ and (b) $e_n = 0.2$, with other parameters as in Fig. 2.17). Power spectrum of the coarse-grained density field of panels a and b are shown in bottom panels (c) and (d) respectively.

Figures 2.19(c) and 2.19(d) show the power spectra for $e_n = 0.9$ and 0.2 respectively. There is a dominant peak at $(k_x, k_y) = (0, 1)$ in Fig. 2.19(c) which is a signature of the inhomogeneous distribution of particles along the wall-normal (y) direction – this is dubbed 'plug-type' flow as expected in the Poiseuille flow. On the other hand, at $e_n = 0.2$, Fig. 2.19(d) contains an additional dominant peak at $(k_x, k_y) = (0, 2)$, along with sub-dominant peaks at $(k_x, k_y) = (1, 0)$ and $(1, 1)$. Collectively, the peaks at $(k_x, k_y) = (0, 1)$ and $(1, 0)$ imply that the particles are inhomogeneously distributed along both the streamwise and wall-normal directions, and is dubbed 'slug/clump' (Liss *et al.* 2002; Alam *et al.* 2009). Therefore, with reference to Figs. 2.17(a), the flow transcends from a plug to a slug/clump as the dissipation is increased. These axial inhomogeneities increase the centerline mean-free path λ_0, leading to a decrease of both Kn_0 and Fr_0 for $e_n < 0.6$, and are, in turn, responsible for the sharp increase of $(\triangle T/Fr_0^2)$ in the same limit as illustrated in Fig. 2.18(a).

2.6 Conclusion and Discussion

2.6.1 Conclusion: competition between rarefaction and inelastic dissipation

The roles of inelastic dissipation and wall-roughness on two well-known rarefaction phenomena, the 'Knudsen-minimum' effect and the 'bimodality' of the temperature profile, were elucidated for a dilute granular/athermal Poiseuille flow via event-driven simulations of smooth inelastic hard-disks under gravity. The wall-roughness has a crucial role in the elastic limit ($e_n \to 1$): in channels with smooth walls ($\beta_w \sim -1$, i.e. reflected-type collisions), we uncovered a local minimum in the flow rate (resembling the well-known Knudsen minimum) that occurred at a Knudsen number of $Kn \sim O(0.01)$ but the maximum flow rate occurred at a finite Knudsen number of $Kn \sim O(1)$, beyond which the flow-rate decreases. On the other hand, the Knudsen minimum was found to be absent (i) even for quasi-elastic collisions ($e_n < 0.99$), irrespective of the wall-roughness, as well as (ii) for relatively rougher walls ($\beta_w > -0.6$) at any e_n as summarized in the phase diagram in Fig. 2.9. An anomalous effect, the decreased slip velocity with increasing Kn, was uncovered in smooth-walled channels for dissipative particles, which is responsible for the continual decrease of the flow rate with increasing Kn for $e_n < 0.99$. The origin of this anomalous variation of the slip velocity seems to be tied to the competing effects of (i) the dissipation-induced 'clustering' (i.e. the inhomogeneity of the density field along the transverse/wall-normal direction) and (ii) the rarefaction-induced 'declustering' of particles along the wall-normal direction.

The granular temperature profile is found to be of 'bimodal' shape, with a minimum at the channel centerline and two symmetric maxima away from center, at any $Kn > 0$ for $e_n \leq 0.9997$. In contrast, the temperature bimodality is known to occur in the Poiseuille flow of a molecular gas ($e_n = 1$) beyond a critical value of $Kn > Kn_c \sim 0.01$ (Tij & Santos 1994). We found that the origin of temperature bimodality is inelastic dissipation in the continuum limit (i.e. at $Kn \sim 0$), but the rarefaction effects take over beyond $Kn > O(0.1)$ as in its molecular counterpart. Therefore, the observed temperature bimodality in granular Poiseuille flow is a consequence of the competition between dissipation and rarefaction as discussed in a phase diagram in the $(Kn, 1-e_n)$-plane in Fig. 2.16. Increasing inelastic dissipation increases the excess temperature ratio $\triangle T$ [eqn. (2.21)] and hence the degree of temperature bimodality is enhanced. The above finding is at odds with the predictions ($\triangle T$ decreases with decreasing e_n from the elastic limit and then increases again) of a kinetic model (Tij & Santos 2004).

2.6.2 Discussion: implications for hydrodynamic equations

Here we remark on the validity of Navier-Stokes (NS) order hydrodynamic description for granular gases. With reference to Fig. 2.16, the NS equations will hold in the "unimodal" regime of the phase diagram (to the left of the circled solid-line). On the other hand, we know that the rarefaction-driven bimodality (to the right of the dashed line in Fig. 2.16 for $Kn > 0.01$) cannot be predicted by NS-equations and requires at least Burnett-order equations. In the region lying between the solid and dashed lines in Fig. 2.16, the temperature profile remains bimodal which

is, however, driven by inelastic dissipation as discussed in section 2.5.2. In this regime, the NS-equations may hold as long as (i) the Knudsen number Kn and (ii) the inelastic dissipation $(1-e_n)$ are small. This is because the normal stress difference, which requires a Burnett-order description (Sela & Goldhirsch 1998; Saha & Alam 2014), becomes finite and measurable with increasing dissipation. The is evident from a comparison between Figs. 2.20(a) and 2.20(b) which display the profiles of scaled first normal stress difference $\mathcal{N}_1$, as defined in (2.20), for $e_n = 1$ and 0.99 respectively. Each panel further illustrates that $\mathcal{N}_1$ increases (in the bulk) with increasing Kn for specified values of e_n.

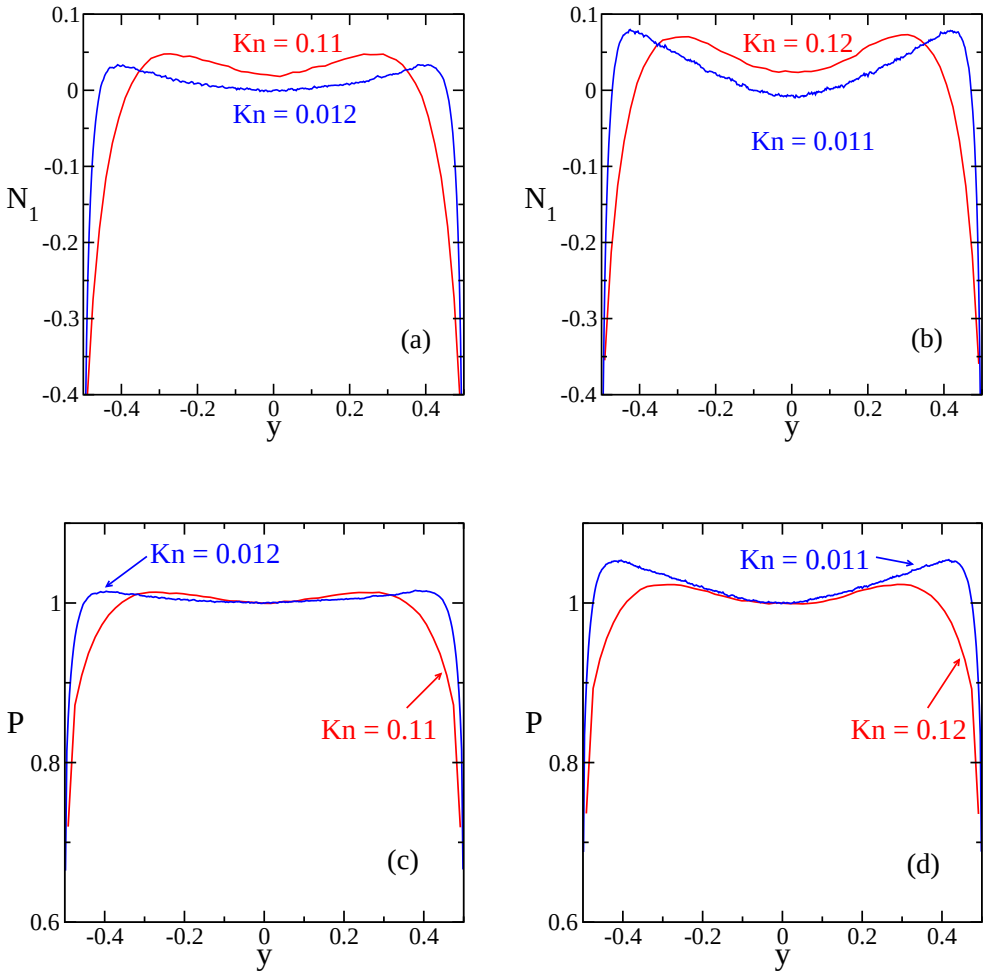

Figure 2.20: Profiles of (a,b) the first normal stress difference $\mathcal{N}_1$, (A.2), and (c,d) the normalized pressure, $P = p(y)/p(0)$, for $e_n = 1$ (left column) and $e_n = 0.99$ (right column). The parameter values are as in Fig. 2.14.

For a theoretical understanding, let us now consider the transverse momentum equation for the steady, unidirectional flow of a granular fluid:

$$\frac{\mathrm{d}p_{yy}}{\mathrm{d}y} = 0 \equiv \frac{\mathrm{d}p}{\mathrm{d}y} - \frac{1}{2}\frac{\mathrm{d}\mathcal{N}_1^*}{\mathrm{d}y} \tag{2.29}$$

where $\mathcal{N}_1^* = (p_{xx} - p_{yy})$ and $p = (p_{xx} + p_{yy})/2$. For NS-equations, $\mathcal{N}_1^* = 0$ and hence $p(y)$ should be uniform across the channel width. Figure 2.20(c) confirms that the pressure is nearly uniform

in the bulk of the channel (except near boundaries) for $Kn = 0.012$ and $e_n = 1$, but visible non-uniformity prevails at higher values of $Kn = 0.11$. Recall from Fig. 2.16 that the onset of bimodality occurs at $Kn = Kn_c \approx 0.01$ for $e_n = 1$, and NS-equations are expected to hold below Kn_c for this case. On the other hand, Fig. 2.20(d) indicates that the pressure is non-uniform for both $Kn = 0.011$ and 0.12 when the particles are slightly dissipative ($e_n = 0.99$). The origin of non-uniform pressure at $Kn = 0.011$ for $e_n = 0.99$ can be tied to the 'non-negligible' second term in (2.29) as confirmed from Fig. 2.20(b). Therefore, we conclude that, in a phase-diagram such as in Fig. 2.16, the region of validity of NS-hydrodynamics is indeed small (at least for granular Poiseuille flow).

Chapter 3

Taylor-Couette Flow and MD Simulation

3.1 Introduction

The flow between two concentric rotating cylinders, dubbed Taylor-Couette (TC) flow, has been a subject of importance since the initial studies by Newton in 1687, but it was not till Couette and Mallock (Mallock 1888; Couette 1888) did independent experiments in 1888 to measure the viscosity of water, the subject gained much attention. Rayleigh (1917) formulated a stability criterion which was based on the inviscid perturbation equations. He predicted that irrespective of the speed of the inner cylinder, the flow should be unstable for a stationary outer cylinder. Since viscosity damps the perturbations for low rotational speeds, preventing the vortices from forming, Rayleigh's stability criterion could not describe the underlying physics of the instability. Taylor's seminal paper in 1923 showed how visous forces stabilise flow at low rotational speed and contained an examination of linear stability theory for general cases of viscous flows with both cylinders rotating in the same as well as opposite directions. His paper also contained an account of his experimental apparatus, which used ink visualization, and presented the photographs and patterns of flow in the unstable regime (Taylor 1923). The TC geometry has two advantages over a normal pipe: in the small gap limit, *i.e.* if $d_w/R_i \ll 1$ (where $d_w = R_o - R_i$ is the gap-width, and R_i and R_o are the radii of inner and outer cylinders), the shear rate and thus the Reynolds number are constant across the gap and the streamlines are curved. Taylor showed, both theoretically and experimentally, that the viscometric base Couette flow was linearly unstable beyond a critical rotational speed of the inner cylinder. For a given fluid of kinematic viscosity ν and a given geometry within the small gap limit (setting d_w and R_i), Taylor obtained the stability boundary for any co- or counter-rotation of the cylinders. Experimentally, Taylor's apparatus had the advantage of allowing for flow visualization, which was absent in previous studies. Taylor showed that above the instability threshold the cellular patterns are formed in which the fluid travels in helical paths around the cylinders in layers of counter-rotating vortices, now known as "*Taylor vortices*". Since then, numerous theoretical, experimental, and numerical studies (Andereck *et al.* 1986; Chandrasekhar 1960; Clever & Busse 1997; Cole 1965; Wereley & Lueptow 1998) have been conducted regarding different aspects of Taylor-Couette flow. The recent decades have seen a burst in interest that the Taylor-Couette flow is called the "Hydrogen atom of fluid dynamics" (Tagg 1994) and has recently been compared to the *Drosophila* of biology (van Gils *et al.* 2012).

Originally the physics of flow instabilities was focused on simple pipe flow considering Newtonian fluids like water. The Reynolds number ($Re = \frac{dU\rho}{\mu}$) , where d being a characteristic length along the velocity gradient direction, U being a characteristic velocity and μ being the

shear viscosity of the fluid, is considered as a parameter to quantify the relative importance of two types of forces: *destabilizing inertial and stabilizing viscous* forces for given flow conditions. However, the TC flow is based on both inner (Re_i) and outer Reynolds number (Re_o) measured in terms of inner and outer rotations respectively. But, it is more appropriate to represent the flow in terms of Taylor number

$$Ta = \frac{\omega R_i (R_o - R_i)^3 \rho^2}{\mu^2} \tag{3.1}$$

where $\omega = (\omega_i$ or $\omega_o)$ is a characteristic angular velocity, R_o and R_i are the outer and inner radius respectively and rotation ratio $(\frac{\omega_o}{\omega_i})$ $(-ve$ for counter-rotating cylinder and $+ve$ for co-rotating cylinders). The flow is stable for outer cylinder rotating with the inner cylinder being stationary, or, the latter rotating at a lower rate. The instabilites occur only if the Taylor number exceeds a critical value (Ta_c).

The motion of a fluid confined between two concentric cylinders with the inner one rotating at angular velocity ω_i undergoes a series of transitions with increasing Reynolds number (Re_i). The initial transition is from azimuthal laminar flow to Taylor vortex flow (TVF), which is followed by a transition to wavy vortex flow (WVF). At a fixed Re_i in this wavy vortex flow regime, several steady states are possible, each characterized by different number of waves around the annulus. The transition to wavy vortex flow occurs at a radius ratio of 0.8, but for a low radius ratio of 0.5 it occurs at a higher Reynolds number. The experiments of Cole (Cole 1965) indicate that the critical Reynolds number for the onset of waves is strongly affected by end-wall effects.

It is well known that Taylor vortices appear due to the pitchfork bifurcation with a critical value of Taylor number which is dependent on the aspect and radius ratios. But Benjamin and Mullin (Benjamin & Mullin 1981) discovered that the pitchfork bifurcation is modified by the presence of stationary end-walls. They observed anomalous modes due to the confined geometry in the axial direction which was earlier observed experimentally (Benjamin 1978). Typically, the end-wall effects can be avoided in simulations by considering periodic boundary conditions, experimentally by considering long cylinders compared to the gap-width, and theoretically by assuming infintely long cylinders. In this way, the centrifugal instability is considered without the interference of the confining end-walls. However, the end-walls have an important influence on the flow throughout the Taylor-Couette cell. Figure 3.1 taken from the experimental studies of Andereck *et al.* (1986) shows the non-trivial effects of the end-walls. In the bulk, away from the end-walls the stable flow is geostropic; in other words, the centrifugal force due to the azimuthal velocity is balanced by the pressure gradient force. However, the no-slip boundary condition results in an azimuthal velocity near the end-wall which is different from that far from the end-wall. The imbalance between the pressure gradient force and the centrifugal force near the end-wall drives the fluid in two different forms depending on the nature of the end-wall boundary condition. The boundary-driven flow at the end-walls can be considered either a Bodewadt flow (Bödewadt 1940), where the end-wall is fixed and the fluid is rotating, or an Ekman flow, where the end-wall and fluid are rotating at different angular velocities. With no-slip boundary condition at the stationary end-walls, azimuthal velocity reduces near the end-walls compared to the flow in the bulk, generating a boundary layer at bottom and top (Czarny *et al.* 2003). This makes the flow radially inwards and recirculation occurs in the bulk of the system. *Ekman*

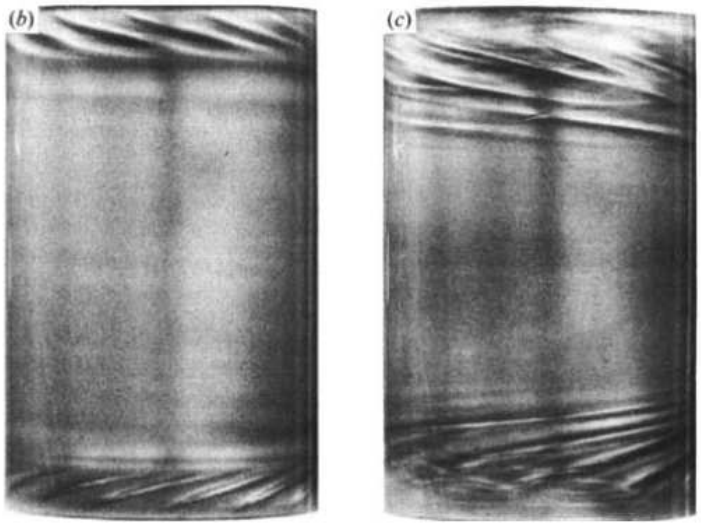

Figure 3.1: End-wall effects (Andereck *et al.* 1986)

vortices can be of the same size as Taylor-vortices for stationary outer cylinder; recent studies on independently rotating cylinders have revealed that a large-scale circulation consisting of two cells can emerge at the boundary layer near the ends (Hollerbach & Fournier 2005). Many authors have reported the importance of end-wall effects (Ahlers & Cannell 1983) analysed the vortex front propagation from an end-wall; Cliffe & Mullin ((985) presented numerical calculations of anomalous modes which was compared with their experimental observations.

Andereck *et al.* (1986) gave a detailed study of different structures being formed on varying the inner Reynolds number. It served as a guide to new experimental and theoretical studies of bifurcations and bifurcation sequences in the circular Couette system. Observed states included Taylor vortices, wavy vortices, modulated wavy vortices, vortices with wavy outflow boundaries, vortices with wavy inflow boundaries, vortices with flat boundaries and internal waves (twists), laminar spirals, interpenetrating spirals, waves on interpenetrating spirals, spiral turbulence, a flow with intermittent turbulent spots, turbulent Taylor vortices, a turbulent flow with no large-scale features, and various combinations of these flows as shown in Fig. 3.2. With initial emphasis on experiments and analytical studies, numerical simulations also gained momentum with the advancement in computer simulation techniques, to solve Navier-Stokes numerically. Since Marcus's work (Marcus 1984), after the preliminary works of Moser *et al.* (1983) and Jones (1981), where he solved the viscous Navier-Stokes equations as an intial value problem to study the non-axisymmetric time-dependent behavior of Taylor vortices, and compared his results with experiments, the numerical-based techniques have become important to understand the flow behavior in a TC setup. At higher Reynolds numbers, the axisymmetric Taylor vortices can become unstable via a Hopf bifurcation towards time-dependent flows which have the form of a rotating wave.

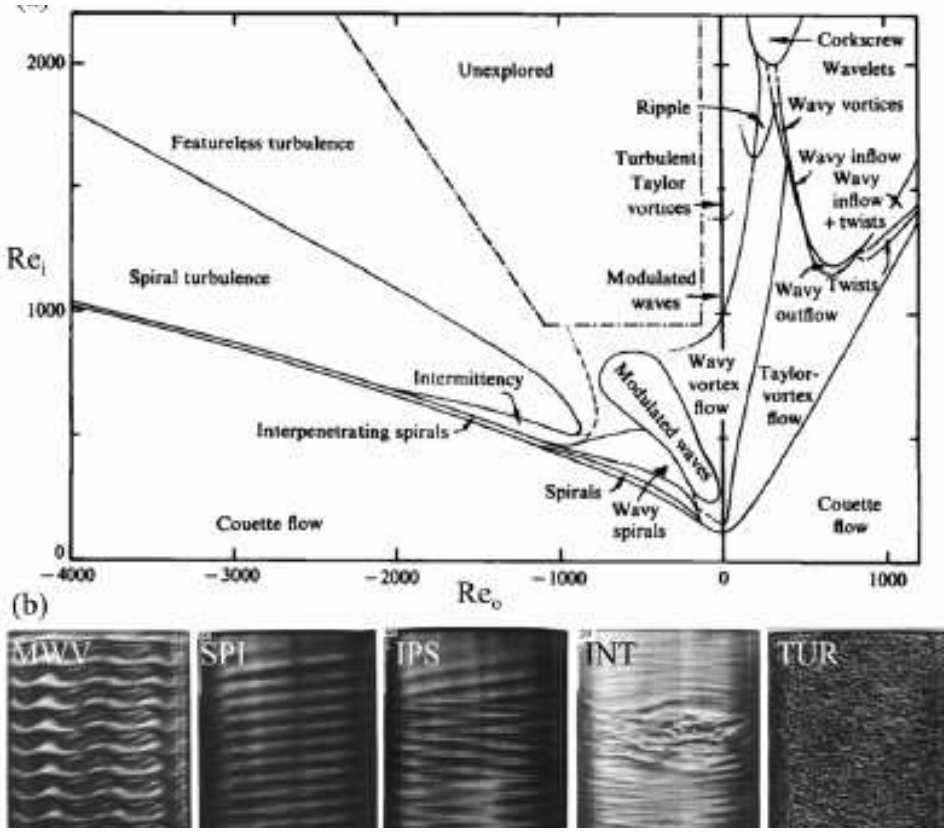

Figure 3.2: (*a*) Phase diagram in the (Re_o, Re_i)-plane in the small gap limit (*b*) Different flow states: modulated waves MWV, spiral, interpenetrating spirals, intermittent turbulent on top of spirals, and featureless turbulence (Andereck *et al.* 1986)

Molecular dynamics (MD) methods have, over the past decade, been used in the study of flow instability at microscopic scales. Work has been confined to two-dimensional flows: both vortex shedding in obstructed flow (Rapaport & Clementi 1986; Rapaport 1987) and convective roll formation in the Rayleigh-Benard problem (Mareschal & Kestemont 1987; Puhl *et al.* 1989) have been modeled. The surprising outcome of these simulations is not only that familiar macroscopic phenomena are reproduced in such minuscule systems (the typical size is no more than a few hundred angstroms), but the quantitative aspects of the flow behavior also agree with continuum results. MD has been able to reproduce many important phenomena in excellent quantitative agreement with theory and experiment (Hirshfeld & Rapaport 1998) in Taylor-Couette setup.

3.2 MD Simulation of Taylor-Couette Flow : Code Development

The code development is based on the tranformation of Cartesian co-ordinate system to polar co-ordinate when particle-wall collisions occur. The first part includes the development of two concentric cylinders, with inner cylinder rotating at ω_i as discussed in §3.2.1. To incorporate finite slip at the boundaries and to attain a steady state for elastic collision case, thermal boundary conditions (Maxwell 1867; Tehver *et al.* 1998) are employed at both the inner and outer boundaries (See §3.2.2). Each particle colliding with the wall has all the memory of

its previous velocity erased, and is reflected back into the system with a velocity taken from Maxwellian distribution; for the wall corresponding to the rotating cylinder the local (tangential) velocity is added to this random velocity vector. This mechanism is sufficient to drive the fluid rotation and dissipate the energy generated by the shear flow. Given the mean volume fraction of spheres in 3D

$$\nu_{av} = \frac{N d_p^3}{6(R_o^2 - R_i^2)L}, \tag{3.2}$$

and mean area fraction of particles in 2D

$$\nu_{av} = \frac{N d_p^2}{4(R_o^2 - R_i^2)}, \tag{3.3}$$

the gap-width ($d_w = (R_o - R_i)$) and the rotation ω_i of the inner cylinder, a collection of N smooth and rigid inelastic particles of masss $m = 1$ and diameter $d_p = 1$ are positioned randomly, and are assigned random initial velocities (chosen from a Maxwellian distribution).

3.2.1 Circular boundary

The circular boundary can be created by setting the inner and outer radius usually determined by a parameter, gap-width $d_w = R_o - R_i$, where R_o = outer radius and R_i = Inner radius. An event-driven algorithm is used to simulate the temporal dynamics of this system (Lubachevsky 1991). The particles are assigned the positions based on Cartesian co-ordinate system (x, y) but can be mapped to polar co-ordinates by using the following conversion:

$$r = \sqrt{x^2 + y^2} \tag{3.4}$$

$$\theta = tan^{-1}\left(\frac{y}{x}\right) \tag{3.5}$$

where (x, y) are Cartesian co-ordinates and (r, θ) are polar co-ordinates. The velocities are converted using:

$$\begin{pmatrix} V_r \\ V_\theta \end{pmatrix} = \begin{pmatrix} V_x \\ V_y \end{pmatrix} \begin{pmatrix} \cos\theta & \sin\theta \\ -\sin\theta & \cos\theta \end{pmatrix} \tag{3.6}$$

where V_r and V_θ are radial and azimuthal velocity respectively. The particles are removed from the system which fall outside the outer cylinder such that $\sqrt{x^2 + y^2} > (R_o - d_p/2)$ and this process is repeated till ν_{av} is achieved. The same procedure is followed for particles whose positions are such that $\sqrt{x^2 + y^2} < (R_i + d_p/2)$. The neighbour list algorithm (Chapter 2) can be modified in a similar way. Only those particles are checked for collision in the neighbouring cells for which $\sqrt{x^2 + y^2} < (R_o - d_p/2)$ and $\sqrt{x^2 + y^2} > (R_i + d_p/2)$. In order to make sure that the particles outside the system do not interact with the system, they are assigned a minuscule magnitude of velocity $\sim O(10^{-12})$. Various simulations for different values of mean volume fraction (ν_{av}) were run to check that the particle number does not exceed N by interacting with the particles outside.

Similarly, the neighbour list algorithm need to be modified for the annular geometry. The algorithm to check for the nearest neighbour is similar to the Cartesian code used in Chapter 2,

the only difference being in the method of calculating the nearest cell. For the cells near the outer boundary, a check is made everytime the code searches for its nearest neighbour, to eliminate the event of collision where a particle is out of bounds. The same procedure was implemented for the inner circle. A detailed discussion on the boundary conditions is given in the following section.

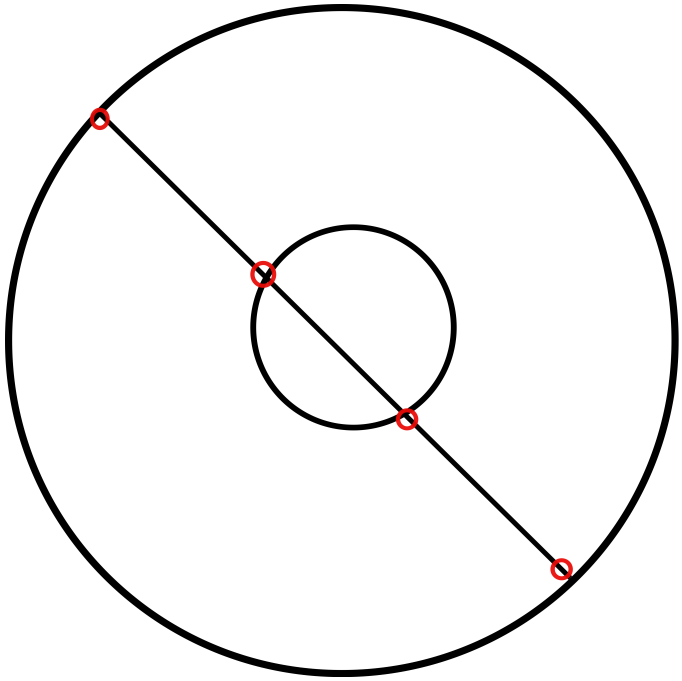

Figure 3.3: Intersection points of a circle and a line.

3.2.2 Boundary conditions

The boundary is modelled as thermal walls to supply energy into a dissipative system like a granular gas. Whenever a particle hits the wall, its velocity is chosen fom a Maxwell distribution according to a certain wall temperature T_w. There is, however, a complication which is frequently disregarded in the literature. If at wall collisions both components of the particle velocity are chosen from a Gaussian distribution, after a short time the temperature of the gas approaches an incorrect final temperature $T' < T_w$, although the gas is supposed to be in thermal equilibrium with the wall of temperature T_w. This is mainly due to over prediction of fast moving particles hitting the wall with more frquency compared to slow moving particles which lead to a distortion of the velocity distribution (Pöschel & Schwager 2005) and cool the system, since the number of fast moving particles after wall-contact is too small.

To overcome this problem, the particles close to the wall are given random normal velocities such that the statistical properties are conserved, *.i.e.* $\propto c^n N(c^n)$ particles must be assigned the normal velocity c^n. Consequently, at wall collisions the normal velocities have to be determined

according to the probability distribution (Pöschel & Schwager 2005):

$$p(c^n) = \frac{m}{T_w} c^n exp\Big[- \frac{m(c^n)^2}{2T_w} \Big], \tag{3.7}$$

where the prefactor comes from the normalization condition $\int_0^\infty p(c^n)\, dp = 1$.

The above arguments do not apply to the tangential velocities since the rate of wall collisions depends only on the normal velocity component, but is independent of the tangential component. Hence, the tangential velocities have to be chosen from a Maxwell distribution.

$$p(c^t) = \sqrt{\frac{m}{2\pi T_w}} exp\Big[- \frac{m(c^t)^2}{2T_w} \Big] \tag{3.8}$$

which is normalized as $\int_{-\infty}^\infty p(c^t)\, dp = 1$.

The above procedure is used in the present simulation to produce a finite slip at the wall and to stabilise the energy to a steady state value for elastic systems. For the wall corresponding to the rotating inner cylinder the local (tangential) velocity is added to this vector, and the post-collisional velocities in both normal and tangential directions are given by,

$$\vec{c_r}' = \sqrt{\frac{2k_B T_w}{m}} v_{BG}, \tag{3.9}$$

$$\vec{c_\theta}' = \sqrt{\frac{k_B T_w}{m}} v_G + R_i \times \omega_i, \tag{3.10}$$

respectively, where c_r' is the post-collisional radial velocity and c_θ' is its azimuthal component. Note that v_{BG} and v_G are given by (3.7) and (3.8) respectively.

The system in an event-driven simulation moves from one state to another with respect to an event, the event being the collisions. The main assumption in event-based molecular dynamics is that at any instant only one collision occurs in an infinitesimal small interval of time, the details of which were given in Chapter 2. The wall-particle collision, particle-particle collision and neighbouring cell boundary crossing are three different events with respect to which the system moves, where the minimum of the three sets the time for the system to evolve. The algorithm calculates the time taken for all three events for the particle under consideration and then moves the system based on t_{min}. The algorithm to obtain the minimum for particle-particle and wall-particle collision in the code requires indepth discussion for the reader to understand, whereas the neighbouring cell-crossing is trivial to implement.

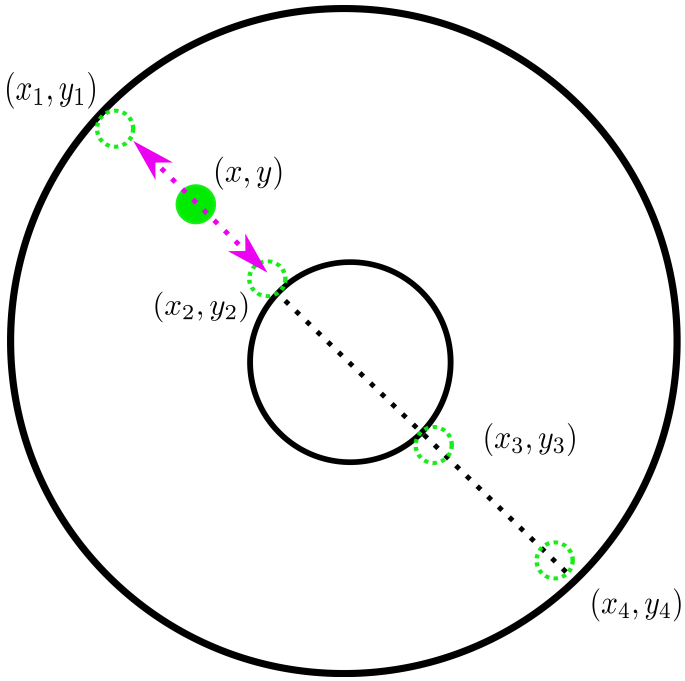

Figure 3.4: Schematic of possible collisions of a particle with circular boundaries.

The wall-particle collision is modeled as the intersection of a straight line (along the particle velocity vector) with circles. The equation of a circle and a line can be obtained from the parameters of the system namely, the gap-width and outer cylinder radius, whereas the equation of the straight line is obtained from the particle velocity vector. The equation is a quadratic equation and is solved to get the roots as shown in Fig. 3.3. There are four roots for two circles and the minimum is calculated depending on the velocity vector of the particles. The equation of outer circle

$$x^2 + y^2 = (R_o - d_p/2)^2 \tag{3.11}$$

and the inner circle

$$x^2 + y^2 = (R_i + d_p/2)^2 \tag{3.12}$$

is solved using the equation of the line

$$y = \frac{c_y}{c_x}x + k \rightarrow k = y - \frac{c_y}{c_x}x \tag{3.13}$$

Both equations (3.11) and (3.12) are solved independently using the same equation of line (3.13). The dot product of the relative position vector and the velocity vector of the particles determines the direction of the particle motion and is used to calculate the minimum time.

$$\vec{x} \cdot \vec{c} > 0, \text{if } x \in (x_1, y_1) \text{ or } (x_4, y_4) \tag{3.14}$$

The above condition is satisfied if the particle collides with the outer wall , and

$$\vec{x} \cdot \vec{c} < 0, \text{if } x \in (x_2, y_2) \text{ or } (x_3, y_3) \tag{3.15}$$

if it collides with the inner wall as shown in Fig. 3.4.

The minimum time is calculated and the particle is moved to a new position, if the particle collides with the wall, then it takes up velocity according to (3.9) and (3.10).

3.2.3 Axial length

In three dimensions, the addition of a length in the axial direction (z) is trivial and the neighbour-list algorithm needs to be modified for 3D accordingly. Another parameter which comes up is the aspect ratio L/d_w, where L is the length of the cylinder. In this study, two types of axial boundary conditions are used : *periodic* and *reflecting*. For reflecting boundary conditions, when a particle hits the axial boundary, its velocity in the z-direction reverses keeping the other two components fixed. This amounts to reflect incident particles elastically from end-walls; the use of slip boundary condition at the ends avoids creating a second source of sheared flow that would distort the vortices (an effect that is unavoidable in experiments) (Hirshfeld & Rapaport 1998). The reflecting boundary conditions are given by:

$$\vec{c_x}' = \vec{c_x} \tag{3.16}$$

$$\vec{c_y}' = \vec{c_y} \tag{3.17}$$

$$\vec{c_z}' = -\vec{c_z} \tag{3.18}$$

On the other hand, the periodic boundary conditions are used to mimic large systems as well as to avoid end boundary effects. This helps to understand the global dynamics of the vortex formation. If a particle moves out of the box in the z-direction, a periodic image of the same particle is created in the opposite direction at same x and y positions with same components of velocity. The algorithm and its implementation was discussed in detail in Chapter 3.

3.3 Hydrodynamic Properties

To extract hydrodynamic fields from simulations, we divide the circular annulus into an array of bins in the radial and azimuthal directions, each of width $w_r = (R_o - R_i)/n_{binr}$ and $w_\theta = 2\pi/n_{bin\theta}$ ($w_r, w_\theta > d_p$), respectively, as shown in Fig. 3.5 and then carry out 'binwise' averaging by collecting data in each bin after reaching a statistical steady state.

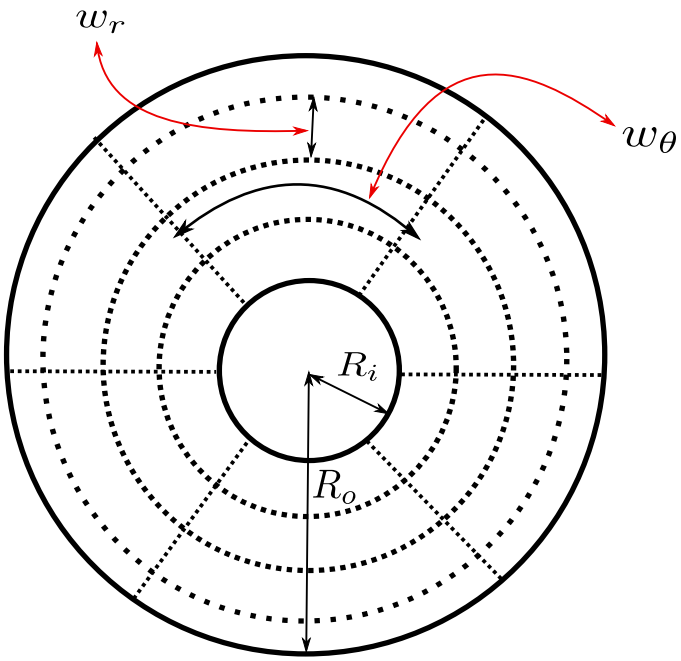

Figure 3.5: Bin wise averaging in Taylor-Couette 2D.

The volume fraction ν, radial velocity (U_r), tangential velocity (U_θ) and granular temperature T in the i^{th} bin (located at $r = r_i$ and $\theta = \theta_i$) are calculated from:

$$\nu(r,\theta) = \frac{d_p^2 \times n_{binr} \times n_{bin\theta}}{4(R_o^2 - R_i^2)} \Big\langle \sum_{i=1}^{N} \delta(r - r_i)\delta(\theta - \theta_i) \Big\rangle, \tag{3.19}$$

$$U_r(r,\theta) = \frac{\Big\langle \sum_{i=1}^{N} c_{ri}(t)\delta(r - r_i)\delta(\theta - \theta_i) \Big\rangle}{\Big\langle \sum_{i=1}^{N} \delta(r - r_i)\delta(\theta - \theta_i) \Big\rangle}, \tag{3.20}$$

$$U_\theta(r,\theta) = \frac{\Big\langle \sum_{i=1}^{N} c_{\theta i}(t)\delta(r - r_i)\delta(\theta - \theta_i) \Big\rangle}{\Big\langle \sum_{i=1}^{N} \delta(r - r_i)\delta(\theta - \theta_i) \Big\rangle}, \tag{3.21}$$

$$T(r,\theta) = \frac{\Big\langle \sum_{i=1}^{N} \mathbf{C}_i(t)\mathbf{C}_i(t)\delta(r - r_i)\delta(\theta - \theta_i) \Big\rangle}{2\Big\langle \sum_{i=1}^{N} \delta(r - r_i)\delta(\theta - \theta_i) \Big\rangle}, \tag{3.22}$$

where $\mathbf{C}_i(t) = \mathbf{c}_i(t) - U(r,\theta)$ is the peculiar velocity of particles and $\langle\cdot\rangle$ represents the time-averaging over a large number of snapshots of the system. For non-dimensionalization, the reference length, time and velocity scales are taken to be:

$$L_r = d_w, \tag{3.23}$$

$$t_r = 1/\omega, \tag{3.24}$$

$$U_r = d_w\omega, \tag{3.25}$$

$$T_r = (d_w\omega)^2. \tag{3.26}$$

For 3D, an extra dimensional length in the z-direction adds another variable with L being

the length of the cylinder. The averaging in the azimuthal and radial directions remains the same, whereas the cylinder length is divided into an array of bins of width $w_z = L/n_{binz}$. The volume fraction ν, radial velocity (U_r), tangential velocity (U_θ), axial velocity (U_z) and granular temperature T in the i^{th} bin (located at $r = r_i$, $z = z_i$ and $\theta = \theta_i$) are calculated from:

$$\nu(r,\theta,z) = \frac{d_p^3 \times n_{binr} \times n_{bin\theta} \times n_{binz}}{6(R_o^2 - R_i^2)L} \Big\langle \sum_{i=1}^{N} \delta(r-r_i)\delta(z-z_i)\delta(\theta-\theta_i) \Big\rangle, \tag{3.27}$$

$$U_r(r,\theta,z) = \frac{\Big\langle \sum_{i=1}^{N} c_{ri}(t)\delta(r-r_i)\delta(z-z_i)\delta(\theta-\theta_i) \Big\rangle}{\Big\langle \sum_{i=1}^{N} \delta(r-r_i)\delta(z-z_i)\delta(\theta-\theta_i) \Big\rangle}, \tag{3.28}$$

$$U_\theta(r,\theta,z) = \frac{\Big\langle \sum_{i=1}^{N} c_{\theta i}(t)\delta(r-r_i)\delta(z-z_i)\delta(\theta-\theta_i) \Big\rangle}{\Big\langle \sum_{i=1}^{N} \delta(r-r_i)\delta(z-z_i)\delta(\theta-\theta_i) \Big\rangle}, \tag{3.29}$$

$$U_\theta(r,\theta,z) = \frac{\Big\langle \sum_{i=1}^{N} c_{zi}(t)\delta(r-r_i)\delta(z-z_i)\delta(\theta-\theta_i) \Big\rangle}{\Big\langle \sum_{i=1}^{N} \delta(r-r_i)\delta(z-z_i)\delta(\theta-\theta_i) \Big\rangle}, \tag{3.30}$$

$$T(r,\theta,z) = \frac{\Big\langle \sum_{i=1}^{N} \mathbf{C}_i(t)\mathbf{C}_i(t)\delta(r-r_i)\delta(z-z_i)\delta(\theta-\theta_i) \Big\rangle}{3\Big\langle \sum_{i=1}^{N} \delta(r-r_i)\delta(z-z_i)\delta(\theta-\theta_i) \Big\rangle}, \tag{3.31}$$

where $\mathbf{C}_i(t) = \mathbf{c}_i(t) - U(r,\theta,z)$ is the peculiar velocity of particles and $\langle\cdot\rangle$ represents the time-averaging over a large number of snapshots of the system.

Simulations were run for different values of mean volume fraction to study the spatio-temporal features of the structures; new forms of unstable patterns and clusters were identified which are systematically dealt with in the subsequent chapters. The code is validated to the existing literature in Secs. 3.4 and 3.5

3.4 Code Validation in Two-dimensions

The code for 2D Taylor-Couette flow was validated to ensure that the algorithm used to create the circular boundary can be used for granular TC simulations. Minguito & Meerson (2007) observed that at a fixed radius ratio $\Omega = R_o/R_i$ of the annulus, the granular gas has negative compressibility in the azimuthal direction, having a "spinodal interval" of particle area fractions. The radial variation of local density field averaged in the azimuthal direction agree qualitatively with different values of radius ratio, one such case is shown in Fig. 3.6.

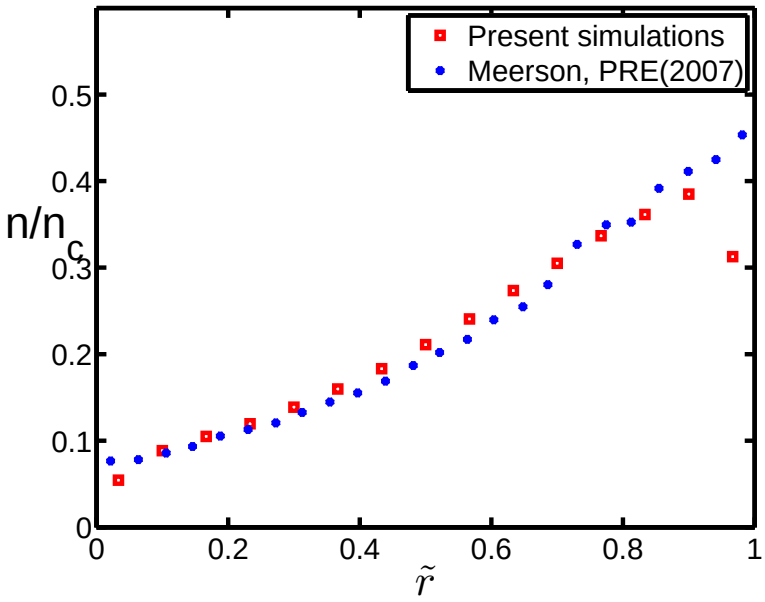

Figure 3.6: Code validation for the annular geometry. The simulations were carried out with $N = 1250$ particles, $e_n = 0.92$, $R_i = 22.0$, $\Omega = 2$ and $n_c = 2/\sqrt{3}d^2$ is the hexagonal close packing density.

Note that the outer and inner cylinders remain stationary in simulations of Minguito & Meerson (2007), but the "driving" interior wall is modeled as a thermal wall kept at temperature T_0, whereas particle collisions with the exterior wall are considered elastic. The energy transferred from the thermal wall to the granulate dissipates in the particle inelastic collisions, and the system reaches a "non equilibrium" steady state with a zero mean flow.

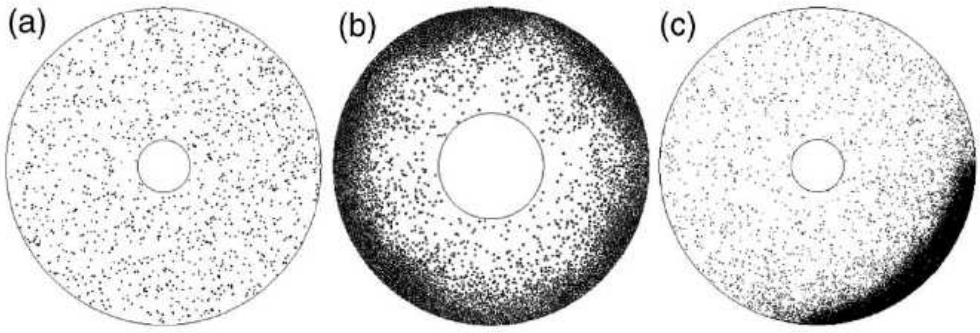

Figure 3.7: Typical snapshots for (a) $N = 1250$ and $\Omega = 6$, (b) $N = 5267$ and $\Omega = 3$, (c) $N = 6320$ and $\Omega = 6$, (c) broken-symmetry state, all simulations for $e_n = 0.92$ (Minguito & Meerson 2007).

As shown in Fig. 3.7(a) (taken from Minguito & Meerson (2007)), for low values of N, a homogeneous state is observed, and as N is increased, the clusters form near the outer wall (panel b). As N is increased further, an annular state appears as in Fig. 3.7c. This time, however, the

annular state is denser, while its local structure varies from a solidlike state with imperfections such as voids and line defects to a liquid-like state. The present simulation results with parameters as in Fig. 3.7 are shown in Figs. 3.8(a,b,c). Overall, there is a good qualitative agreement between present simulations and those of Minguito & Meerson (2007). Figure 3.9(a, b, c) displays density profiles with parameter values as in Fig. 3.8.

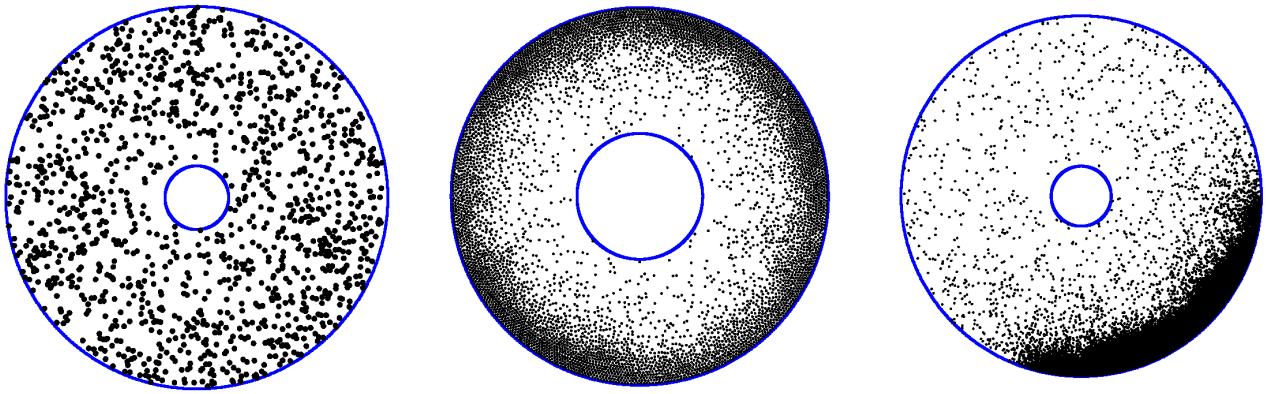

(a) (b) (c)

Figure 3.8: Typical snapshots for (a) $N = 1250$ and $\Omega = 6$, (b) $N = 5267$ and $\Omega = 3$, (c) $N = 6320$ and $\Omega = 6$ (present simulations).

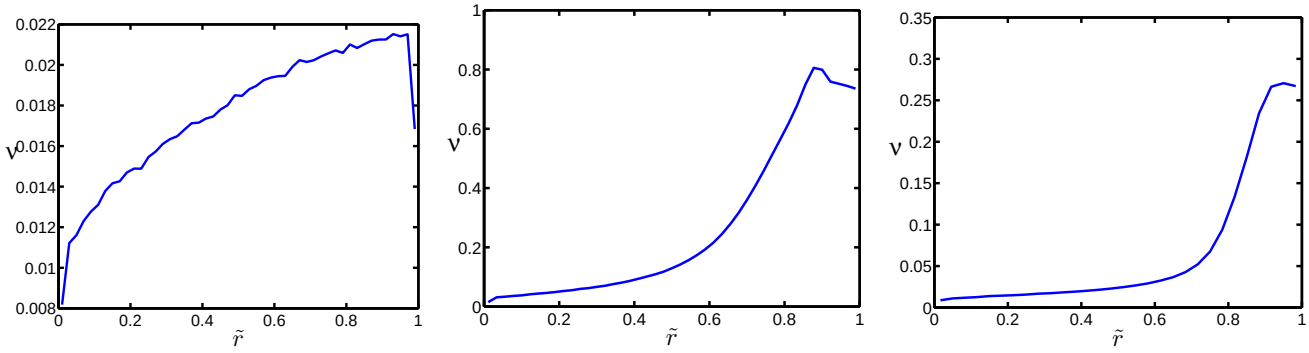

(a) (b) (c)

Figure 3.9: Radial variation of density (a) $\nu_{av} = 0.018$, (b), $\nu_{av} = 0.34$ and (c) $\nu_{av} = 0.094$ for parameter values as in Fig. 3.8.

3.4.1 Particle overlap and tolerance

An important issue that needs to be highlighted in this section is the possibility of overlap of particles in event-driven simulations. This occurs due to very small collision time difference between different particle collisions (events). This can cause overlapping which has been observed in the present study especially in a dense dissipative system where particles tend to cluster. This happens when the code enter into the collision time calculation which involve two step checks: (i) $\vec{c}_{12}.\vec{r}_{12} < 0$ and (ii) $(d - \vec{r}_{12})/d \leq 0$ as given in chapter 2 (Fig. 2.3). The check (ii) is a crude implementation for a highly clustered system and even a small overlap of particles on the

order of $(d - \vec{r}_{12})/d \sim 10^{-8}$ can make the particles to miss a potential collision. To avoid this situation, a small value of tolerance is added to the above check (ii) such that

$$(d - \vec{r}_{12})/d \leq dr_{tol} \tag{3.32}$$

Figure 3.10 shows the variation of collision time with number of collisions. The collision time can attain a value as low as $O(10^{-13})$ as seen in Fig. 3.10 for paramter values as in Fig. 3.8(c). Note that the collision time is a function of mean volume fraction and the dissipation of the system. Figure 3.11 shows the probability distribution of the collision times. The distribution has been calculated using a variable grid size. The distribution gives an idea of the probable collision time which in turn can be used to fix a tolerance value, Eq. (3.32). In order to draw a histogram, the collision time is normalised with standard deviation

$$\sigma_{tcol} = \sqrt{\frac{\sum_{i=1}^{N_{col}} (t_{col_m} - t_{col_i})^2}{N_{col}}} \tag{3.33}$$

where t_{col_m} is the mean of the collision times and the y-axis $(P(t_{col}/\sigma_{tcol}))$ is normalised by the area under the curve.

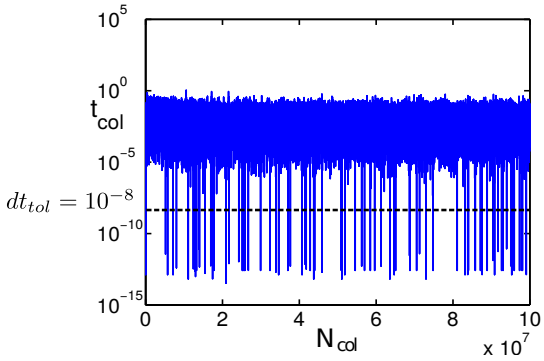

Figure 3.10: Variation of collision time with number of coliisions for paramters as in Fig. 3.8(c). Time is scaled with $d_w/\sqrt{\frac{k_BT}{m}}$ where d_w is the gap-width and $\sqrt{\frac{k_BT}{m}}$ is thermal velocity corresponding to wall temperature.

The value of spatial tolerance is set to $dr_{tol} = 10^{-8}$ in the code and the temporal tolerance is calculated using

$$dt_{tol} = dr_{tol}/\sqrt{\frac{k_BT}{m}} \tag{3.34}$$

where $\sqrt{\frac{k_BT}{m}}$ is the thermal velocity corresponding to wall temperature. In order to ensure that the value of dr_{tol} used in the code does not affect calculated collision times, we analyse the probability distribution of collision times in Fig. 3.11. The calculated value of temporal tolerance should satisfy $dt_{tol} << tcol_{mp}$, where $tcol_{mp}$ is the most probable collision time which falls in the range of $10^{-3} - 20$ in the present analysis after normalising it with σ_{tcol}. The values of standard deviation can be found in table 3.1. Therefore, the true range of $tcol_{mp}$ will be $10^{-5} - 0.1$. The value of temporal tolerance (dt_{tol}) obtained from Eq.(3.34) is 10^{-8} which is very small compared to lower bounds of $tcol_{mp}$ (see Fig. 3.10 and Fig. 3.11(c)).

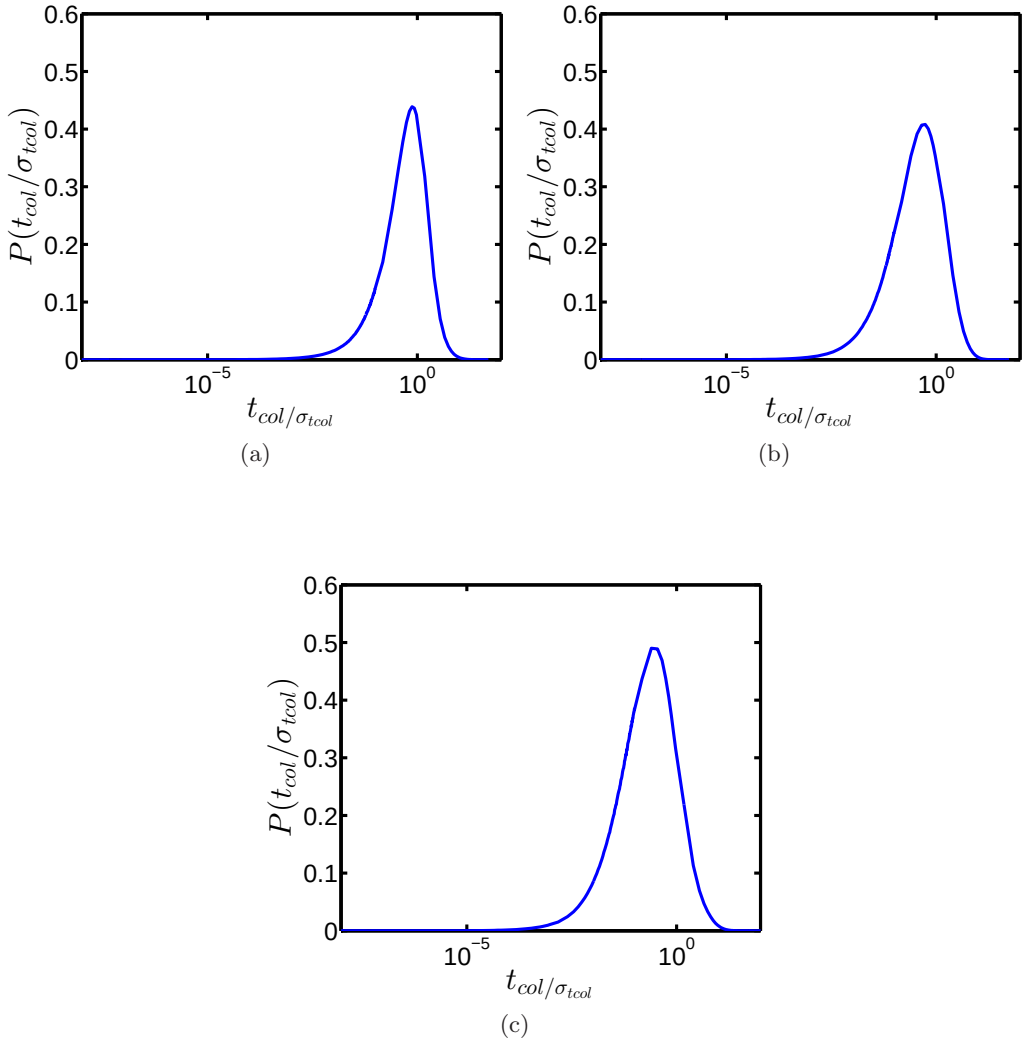

Figure 3.11: Probability distribution of collision time for parameters as in Fig. 3.8(a, b, c) in the same order using variable grid size.

Table 3.1 shows the tolerance used for different cases with the corresponding parameter values. The particle overlapping is significant when $dr_{tol} = 0$ and hence cannot be neglected. The time is scaled with the available scales in the problem : thermal velocity $\sqrt{\frac{k_B T}{m}}$ and the gap-width d_w. No overlapping of the particles was observed when $dr_{tol} = 10^{-8}$, see table 3.1.

ν_{av}	N	e_n	σ_{tol}	Particles overlapped (N_o) without tolerance $(dr_{tol} = 0)$	$dt_{tol} = dr_{tol}/\sqrt{\frac{k_B T}{m}} = 10^{-8}$
0.0188	1276	0.92	2.27 10^{-2}	0	$N_o = 0$
0.34	5280	0.92	3.02 10^{-2}	285	$N_o = 0$
0.094	6392	0.92	2.41 10^{-2}	41	$N_o = 0$

Table 3.1: Table showing effects of using tolerance. Parameters are same as in Fig. 3.8.

As can be seen from table 3.1, the number of overlapped particles (with $dr_{tol} = 0$) are comparatively smaller (Fig. 3.8(a, c)) when the average volume fraction of the system is small as

compared to Fig.3.8(b) for which $\nu_{av} = 0.34$. To sum up the above discussion, Fig. 3.12 shows the effect of particle everlapping on the density profiles of the system. A clear difference between the two suggests that this problem can not be avoided and must be handled carefully. The above tables and figures will be also be shown for the case of rotationg cylinder (Taylor-Couette flow) in the next chapter wherever necessary.

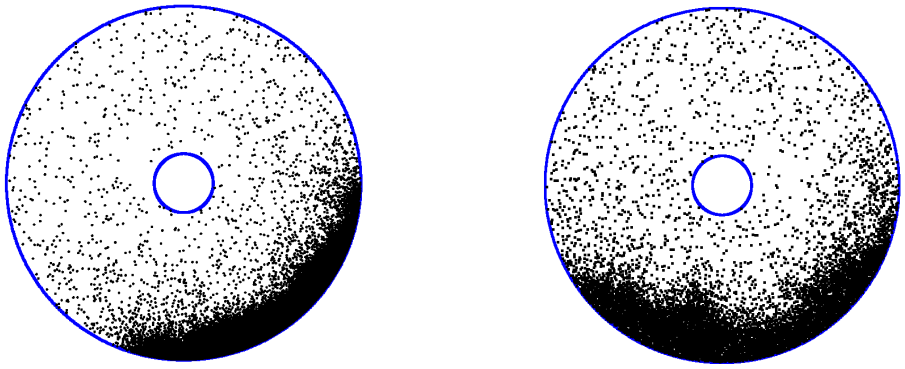

(a) (b)

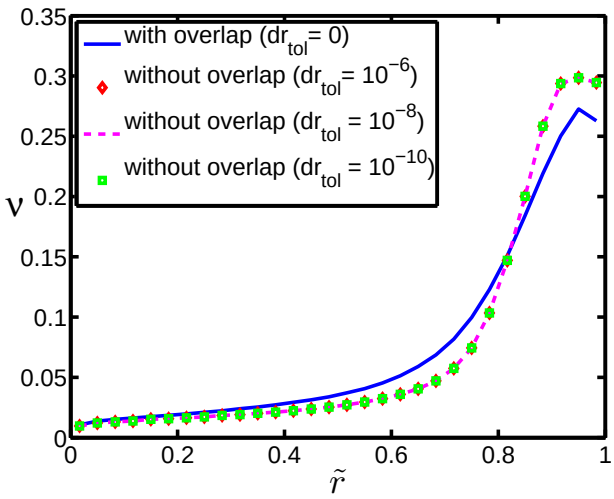

(c)

Figure 3.12: Typical snapshots for parameter values as in Fig. 3.8(c) for (a) without overlap ($dr_{tol} = 10^{-8}$) and (b) overlap system ($dr_{tol} = 0$). (c) Effect of particle overlapping on the density profiles with different values of tolerance.

3.5 Code Validation in Three-dimensions

The 3D code is validated from the first paper on TC flow using MD simulations (Hirshfeld & Rapaport 1998). Hirshfeld & Rapaport (1998) was successful to study the flow instability using particle-based simulations. The formation of toroidal vortices was qualtitatively examined

over a range of supercritical Taylor numbers. Despite of the microscopic system size, an excellent agreement was observed for Fourier amplitudes of the fundamental mode with theory and experiments.

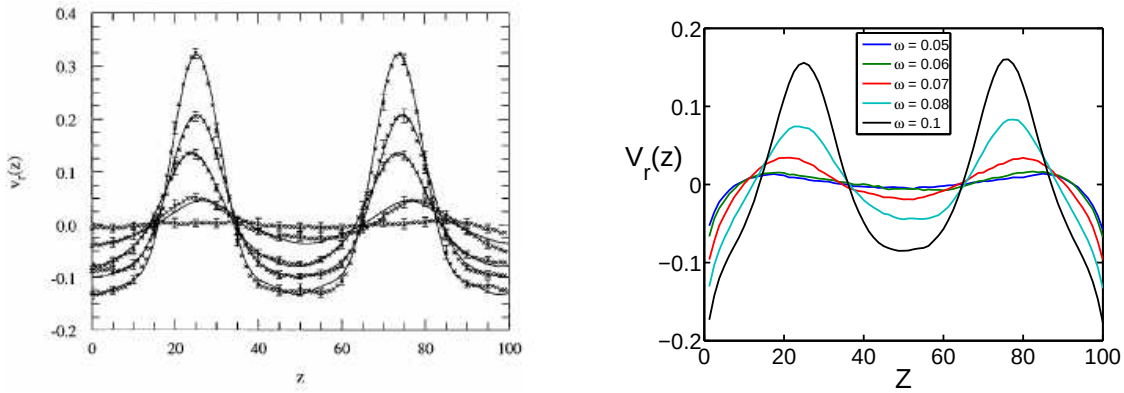

(a) (b)

Figure 3.13: Axial variation of radial velocity (a) (Hirshfeld & Rapaport 1998) (b) present simulations.

In present simulations, the annular width $d_w = 25$, with $R_i = 50$ and $R_o = 75$, is the minimum gap-width for which well developed vortices were observed. The cylinder length (L) is set to 100 with particles colliding elastically, though the particle-particle collision model used by Rapaport was a soft sphere model. We show below that the observations are qualitatively similar even with a hard sphere model with the coefficient of restituion being $e_n = 1$. The mean volume fracion is $\nu_{av} = 0.26$ (3.2) with the particle number of $N = 125000$. In order to reduce the number of particles required for the simulation, only one quadrant of the annular cell is modeled. Special periodic boundaries were used to account for the effect of particles in the absent quadrants as in Hirshfeld & Rapaport (1998). A particle leaving the quadrant returns via the perpendicular boundary with its position and velocity components interchanged accordingly with signs adjusted. These boundary conditions are valid only if the secondary flows remain axisymmetric. Measurements are made only after the system attains a steady state where the energy attains a constant value.

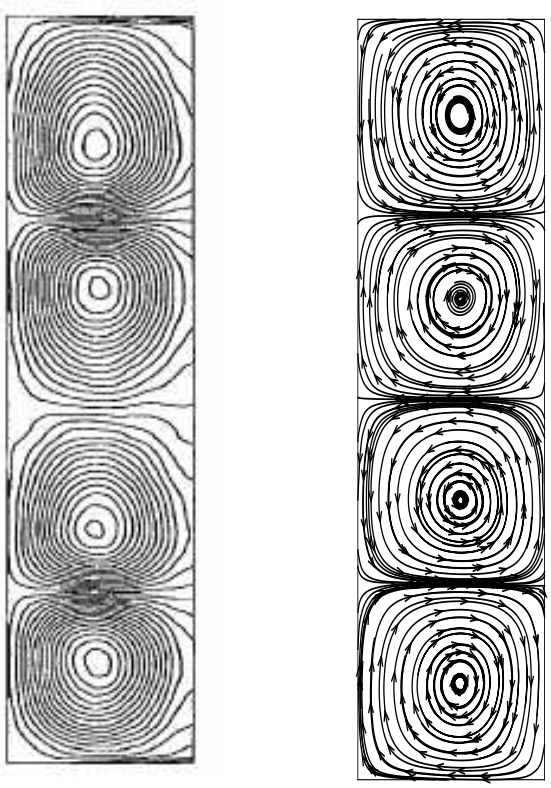

(a) (b)

Figure 3.14: Snapshot of final stage of vortices for $\omega = 0.1$ (a) Hirshfeld & Rapaport (1998)) (b) present simulatons.

The axial variation of radial velocity is shown in Fig. 3.13, and the final picture of the vortex patterns is shown in Figs. 3.14. Even number of vortices are formed, which increases with an increase in the aspect ratio. The magnitude of the radial velocity is different (Fig. 3.13) from the predicted values of Rapaport, possibly because of the soft sphere model and different radial wall boundary conditions (see Hirshfeld & Rapaport (1998)). Note that the vortices obtained in the present simulations are the result of averaging the velocity vectors over the entire simulation period whereas Hirshfeld & Rapaport (1998) uses a window averaging method where each image at a particular time instant (see Fig. 3.14(a)) represents the average over 5000 steps. They stated that the final stage persists for the rest of the run, and hence it can be assumed to be the final stage of the vortices. The qualtitative agreement is considered sufficient to proceed for further study. In the subsequent chapters, the dynamics of 2D and 3D granular Taylor-Couette flows are addressed and discussed in detail.

Chapter 4

Taylor-Couette Flow in Two-dimensions

Rapidly rotating shear flows are ubiquitous in geophysical and astrophysical settings such as planetary atmospheres, stellar interiors, and accretion disk. Recent studies on rarefied gas flows in Taylor-Couette system has garnered a lot of attention in the scientific community with the advent of microfluidic systems. The higher Knudsen number (Kn) flows are particularly an important class of flows because the wall effects play a pivotal role in the dynamics of the system and hence cannot be ingnored. The study by Stefanov & Cercignani (1993) using direct simulation Monte Carlo (DSMC) method found that the critical Taylor number at which the instability occurs is higher than its classical value for incompressible Taylor-Couette flow. They considered the problem of a hard sphere gas in axisymmetric Taylor-Couette flow and found that, contrary to the claims of Kao & Chow (1992), increasing Mach number (Ma) had a stabilising effect for a radius ratio of $R_o/R_i = 2$. Stefanov & Cercignani (1993) related this disagreement to the effects of rarefaction which were not considered by the former authors who used compressible Navier-Stokes equations for stability analysis. Only a few studies have concentrated on the compressible Taylor-Couette problem so far, but none for a granular system. At high Knudsen number, the Knudsen layer develops and covers the entire system, where the Naviers-Stokes equations with no-slip boundary conditions become invalid. The system becomes more complex at intermediate Kn where all the effects (dissipation, rarefaction and inertial) are difficult to separate out. The first experimental investigation of the effects of transonic Mach numbers ($Ma \approx 1$) on the TC instability of dry air was done by Kuhlthau (1960). The onset of instability was identified with sharp increase in the torque measured on the outer cylinder. Knudsen number was varied by varying the density keeping the inner rotation speed fixed. The experiments were carried out for $0.7 \leq Ma \leq 1.5$ showing an increase in the critical Knudsen number (Kn_c) with increasing Ma. The axisymmetric problem has principally been studied by means of the direct simulation Monte Carlo (DSMC) method (Bird 1994). The numerical simulations follow the evolution of the system through its terminal state which, in turn, serves to classify the system response as stable or unstable. Riechelmann & Nanbu (1993) studied this problem for a Maxwell gas. Aoki *et al.* (1999) and Yoshida & Aoki (2006) applied the DSMC method to study the influence of varying both temperature and velocity ratios on the neutral curve. All of the above-mentioned studies demonstrate that TC instability is a small $O(10^{-2})$ Knudsen phenomenon.

The couette flow between two concentric rotating cylinders has interesting features such as "velocity inversion" (Einzel *et al.* 1990) which implies that the azimuthal velocity of the flow increases with distance from a rotating cylinder to a stationary cylinder compared to decrease for the case of an incompressible fluid. The velocity inversion phenomenon has been studied by using

analytical and numerical tools. Einzel *et al.* (1990) first predicted, by suggesting a generalized slip boundary condition for incompressible flow over curved or rough surfaces, that the velocity profile would become inverted in the case of large velocity slip at the wall surfaces. Tibbs *et al.* (1997) did the formulation for the rarefied gases. This was achieved by defining the slip length $\zeta_0 = \alpha(2/\sigma - 1)\lambda$, where λ is the mean-free path of the gas molecules, $\alpha \approx 1.15$ and σ is the tangential momentum accommodation coefficient which can vary from zero for specular reflection and up to unity for diffuse reflection.

The cylindrical Couette flow has also been studied by Aoki *et al.* (2003) using several alternative approaches: a systematic asymptotic analytical solution at small Knudsen numbers, a direct simulation Monte Carlo method, and a direct numerical solution of the Boltzmann equation using a finite difference method based on the Bhatnagar-Gross-Krook (BGK) approximation. Their results again confirmed the existence of an inverted velocity profile for small values of accommodation coefficient, and also showed that the occurrence of velocity inversion could be related to a critical accommodation coefficient.

The two-dimensional (2D) granular shear experiments in an annular cell were carried out by Jasti & Higgs III (2008) to extract solid fraction, velocity, and granular temperature data as a function of the wall roughness factor and wheel rotation rate. In general, the steady-state results show two distinct regions: a high-velocity and dilute-gas-like kinetic region near the moving wall and a high-solid-fraction liquid-like frictional flow regime away from the moving wall. Parametric studies were also conducted to show that the normalized slip near the moving wall decreases with increasing wall roughness and decreasing wall rotation rate.

Instead of implementing Maxwell's boundary conditions based on accomodation coefficients, the current analysis uses the "thermal-wall" boundary conditions as discussed in Chapter 3. In this chapter, 2D simulations of smooth hard disks are carried out in an annular geometry with a rotating inner disk. This type of flow is common in extra-terrestrial flows mainly asteroids and space dust. Effects of inner rotation are considered over a range of densities. This chapter also probes the effects of varying Kn for different ranges of mean densities (ν_{av}) and rotation speeds (ω_i). A similar analysis as done in chapter 3(§3.4.1) on the overlapping of particles is discussed in §4.2 for the case of maximum volume fraction (ν_{av}) simulated in a dissipative system ($e_n = 0.6$).

4.1 Inner Cylinder Rotation: Finite ω_i and Zero ω_o

The system is a circular annulus with inner and outer cylinders. The important parameters in the study are the gap-width d_w, rotation rate (ω_i), inner radius (R_i), coefficient of restitution e_n and mean density ν_{av}. Different parameters are varied to study their corresponding effects on the system. The domain under consideration is divided into an array of bins as shown in Fig. 3.5. The macroscopic properties are calculated based on Eqns.(3.19, 3.20, 3.21, 3.22). Later, an effort will be made to explain the phenomenon of cluster formation for a large gap-width. All simulations are carried out for a range of Knudsen number (Kn) and mean density (ν_{av}), and the macroscopic properties are calculated when the system attains a statistical steady state for which the energy fluctuates around a mean value. Here we will consider the effect of varying the rotational speed (ω_i) of the inner cylinder with a fixed outer cylinder. Cluster dynamics is one important aspect covered in this section along with steady state hydrodynamic profiles, and their dependence on different parameter values.

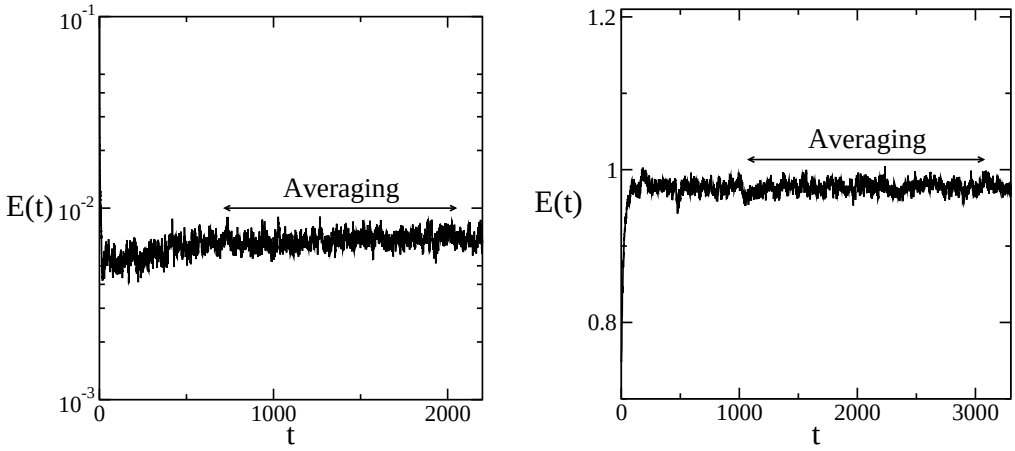

Figure 4.1: Evolution of kinetic energy versus time for (a) $e_n = 0.6$ and (b) $e_n = 1.0$. The system reaches a statistical steady state when $E(t)$ fluctuates around a mean value; the parameters are $R_o = 100$, $d_w = 75$ and $\nu_{av} = 0.40$.

Figure 4.1 shows the temporal variation of kinetic energy, $E(t) = \sum_{i=1}^{N}(c_{xi}^2 + c_{yi}^2)/2N$, per particle for ($a$) $e_n = 0.6$ and (b) $e_n = 1$. In each panel, the initial period of transients continues till a few hundreds of collisions per particle, beyond which the data are collected to calculate the hydrodynamic fields and related coarse-grained quantities. For $e_n = 1$, the thermal-wall boundary conditon plays a crucial role in balancing the increasing energy of the system by maintaining a local equilibrium near the wall, as thermal walls can act as a source or sink depending on the temperature of the system.

4.1.1 Hydrodynamic profiles ($\nu_{av} = 0.05$)

In this section, an average density of $\nu_{av} = 0.05$ is simulated with inner cylinder rotating at different speeds $\omega_i = 0.05 - 1$. The rest of the parameters has been fixed (see table 4.1). The number of particles (N) simulated varies from 1888 for the largest gap-width ($d_w = 75$) to 396

for the smallest gap-width ($d_w = 10$) considered in this study.

$d_w = 75, N = 1888$			$d_w = 10, N = 396$
e_n	ω_i	Kn	Kn
0.6	0.05	0.00016	0.58
	0.1	0.00082	0.611
	0.5	0.0045	0.59
	1	0.0073	0.59
0.99	0.05	0.065	0.56
	0.1	0.0658	0.60
	0.5	0.057	0.67
	1	0.051	0.72
1	0.05	0.0656	0.56
	0.1	0.066	0.61
	0.5	0.057	0.678
	1	0.052	0.724

Table 4.1: Parameters used in simulations to vary the average Knudsen number for mean density $\nu_{av} = 0.05$, $R_o = 100$ ($d_w = R_o - R_i$) and $\omega_o = 0$. The average Knudsen number is defined as $Kn = \lambda_{av}/d_w$.

Density

The variation of density in Fig. 4.2(a) can be explained by the clustering mechanism that occurs in a granular system. The decrease in pressure in high dense regions lead to a movement of particles from high pressure (low density) region to a low pressure (high density) region. This effect due to in-built inelasticity in the system gives rise to numerous patterns and structures. Figure 4.2 ($a - f$) shows the radial variation of local density averaged over multiple snapshots for different values of normal restitution coefficient (rows) and gap-width (columns). However, due to asymmetry in both radial and azimuthal direction, the temporal study becomes essential to study the formation of localised structures. Different parameter values have been simulated to observe the effects of ω_i, d and e_n on the local hydrodynamic fields. The density in Fig. 4.2(a) shows a peak near the centre which start to drift towards the outer radial direction with increase in the value of ω_i for the largest gap-width considered in the simulations. This shift in the density peaks is due to the increase in the centrifugal force on each particle with increase in ω_i and is also observed for $e_n = 0.99, 1$. For the maximum value of $\omega_i = 1$ simulated in the present study, the particles accumulate at the outer boundary, showing a maxima at the outer disk as shown in Fig. 4.2(c, e).

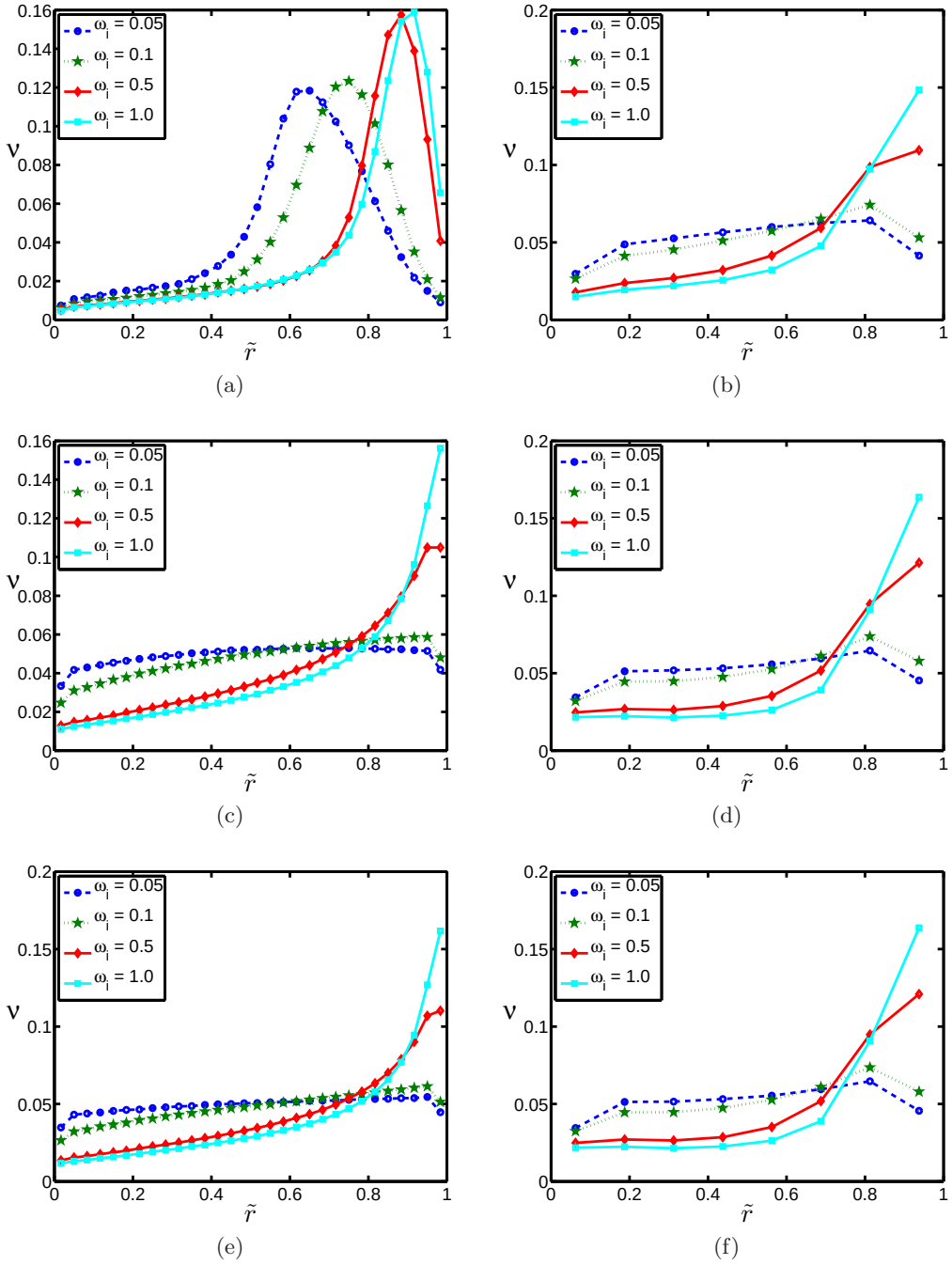

Figure 4.2: Radial density profiles for parameter values of outer radius $R_o = 100$, $\tilde{r} = (r - R_i)/d_w$, gap-width (a, c, e) $d_w = 75$, (b, d, f) $d_w = 10$, mean density $\nu_{av} = 0.05$ and (a, b) $e_n = 0.6$, (c, d) $e_n = 0.99$ and (e, f) $e_n = 1.0$.

For elastic collisions as shown in Fig. 4.2(e, f), the density is uniform throughout both radially and axially, till the inertial force exceeds a critical value where all the particles will be pushed out towards the outer boundary giving a maxima at the outer boundary. A non-trivial phenomenon is observed in Fig. 4.2(b, d, f) for the small gap-width case ($d_w = 10$). All the profiles for ($e_n = 0.6$, $e_n = 0.99$ and $e_n = 1$) show similar behaviour, independent of dissipation in the system. The dissipative mechanism no longer controls the dynamics of the system in the small gap limit, and only centrifugal forces are dominant. These effects are the result of

large Knudsen number as can be seen from table. 4.1. No clustering is observed for this case as wall-particle collisions are more dominant than the particle-particle collision. The Knudsen number for the small gap limit is high $\sim O(1)$, where the boundary effects cannot be avoided. For higher densities ($\nu_{av} = 0.1$ & $\nu_{av} = 0.4$), a subtle difference can be seen for the two gap limits which is discussed in the next section.

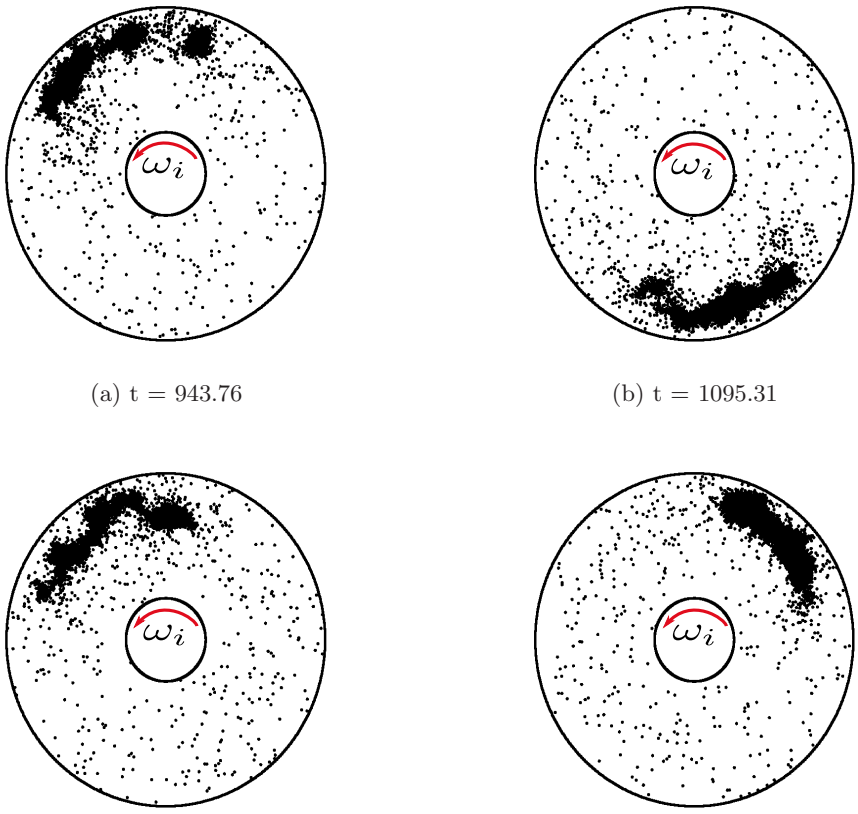

(a) t = 943.76 (b) t = 1095.31

(c) t = 1584.10 (d) t = 2508.74

Figure 4.3: Snapshots showing different stages of cluster - *stretching*(b, c), *compression*(d) *and breaking* (a). Parameter values are $\nu_{av} = 0.05$, $e_n = 0.6$, $d_w = 75$ and $\omega_i = 0.1$.

Figure 4.3 shows the temporal variation of structures for $e_n = 0.6$ with same parameter values as in Fig. 4.2. The cluster goes through different stages - compression, breaking and stretching, which occurs consistently over the time period of the simulation. The formation of localised structures starts due to the dissipation in the system, followed by compression and stretching. A tail of dilute granular gas is always present behind the cluster at every instant. The stretching is observed to occur only when the structure is compressed to a critical/maximum extent where it can no longer sustain the maximum number density, and leads to an outburst of particles. This causes a sudden increase in the velocity, which stabilises instantaneously due to dissipation in the system.

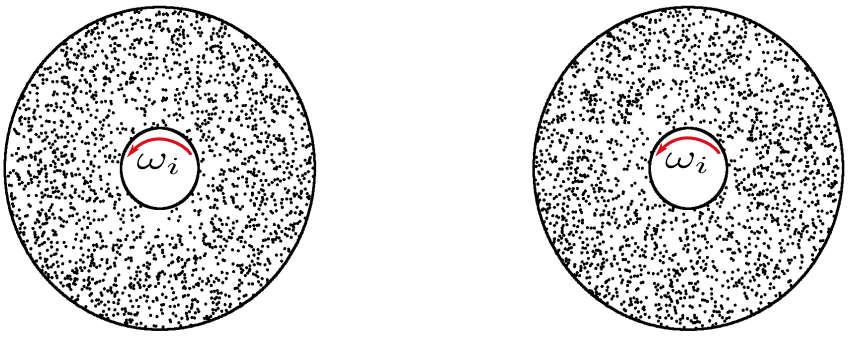

(a) t = 15631.16 (b) t = 40870.477

Figure 4.4: Snapshots showing temporal evolution of the system. Parameter values are as in Fig. 4.3 except $e_n = 0.99$.

Figures 4.4 and 4.5 show the temporal evolution of the system with mild ($e_n = 0.99$) and no dissipation ($e_n = 1.0$) respectively. The homogeneous distribution at $e_n = 0.99$ reflects that the inelasticity does not play significant role in the system due to the absence of clustering in Fig. 4.4(a, b). The larger velocity slip values at the walls (see Fig. 4.6) demonstrates that the rarefaction effects are more dominant at this density regime which are discussed in the next section. Also, the homogeneity is much more prominent in elastic system as given in Fig. 4.5(a, b).

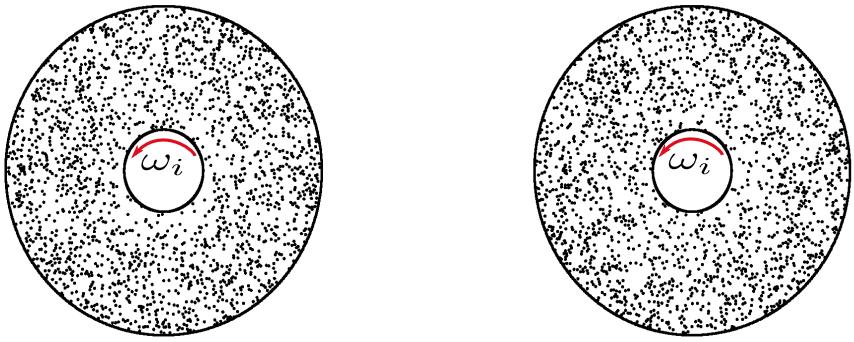

(a) t = 14591.63 (b) t = 38146.07

Figure 4.5: Snapshots showing temporal evolution of the system. Parameter values are as in Fig. 4.3 except $e_n = 1.0$.

Velocity and angular momentum

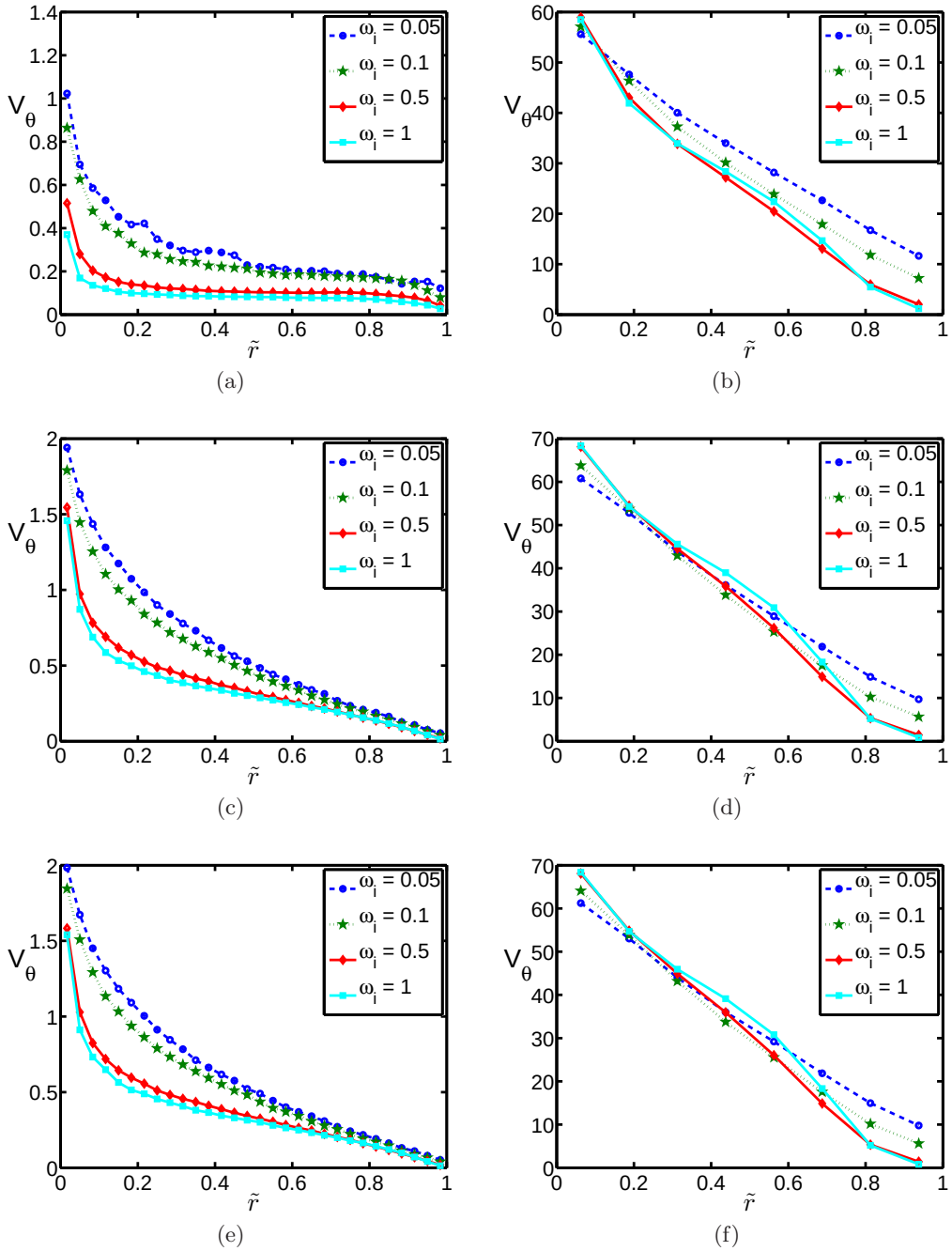

Figure 4.6: Radial variation of azimuthal velocity for parameter values as in fig. 4.2.

Velocity, on the other hand, Fig. 4.6(a, c, e) shows a behavior similar to an irrotational vortex in the large gap limit. The trend is similar to an irrotational vortex flow ($V_\theta \sim \frac{1}{r}$), for an unbounded liquid with inner cylinder rotating. The dip in the profile in Fig. 4.6(a) increases and becomes flat with the increase in the inner rotation. The velocity profile decreases slowly over a certain range, where the cluster formation has taken place. This is due to the instant transfer of momentum due to higher particle-particle collision in the high density clustered region, the velocity drops after that and approaches the value of slip velocity at the outer wall. An important observation

is that when the collisions are elastic (Fig. 4.6(e)), the slip velocity tends to zero for all values of ω_i which is completely opposite to a system where the collisions are inelastic (Fig. 4.6(a)). The finite slip velocity for dissipative system can be explained by clustering mechanism explained above, making the region near the walls particle deficient. The rarefied region leads to a higher slip at the outer wall. The homogenous density distribution ($\omega_i = 0.05$) and high density near the wall ($\omega_i = 1$) for non-dissipative system, leads to negligible slip velocity at the wall as shown in Fig. 4.6(e). Similar inference can be drawn for small gap-width cases shown in Fig. 4.6(b), (d) and (f). The velocity profiles for the small gap-width are similar for elastic and inelastic case, implying that dissipation does not play a role when Knudsen number is higher. In the narrow gap limit, the velocity profiles vary linearly radially approaching plane Couette flow (Taylor 1923). The high density cases are discussed in the subsequent sections.

Further, we focus on angular momentum and angular velocity of the system at low density ($\nu_{av} = 0.05$). The angular momentum ($l(r,\theta)$) and angular velocity ($\omega(r,\theta)$) are calculated as:

$$\omega(r) = \left\langle \omega(r,\theta) \right\rangle_\theta = \left\langle V_\theta(\tilde{r},\theta) \right\rangle_\theta / r, \tag{4.1}$$

$$l(r) = \left\langle l(r,\theta) \right\rangle_\theta = \left\langle \nu(r,\theta) V_\theta(r,\theta) \right\rangle_\theta r, \tag{4.2}$$

where $V_\theta(r,\theta)$ is the azimuthal velocity, $\nu(r,\theta)$ is the local density and r is the radial distance from the centre. Figure 4.7 ($a-f$) shows the radial variations of θ-averaged angular momentum (main panel) and angular velocity (inset). As shown in Fig. 4.7(b, d, f), both angular momentum and velocity show similar variation for the small gap-width ($d_w = 10$) but it changes completely for large gap-width ($d_w = 75$) as shown in Fig. 4.7(a, c, e). Angular velocity shown in the insets of Fig. 4.7 decreases with increase in $\tilde{r}$ which is expected as the angular velocity will be higher near the inner wall (rotating) and lower at the outer wall (stationary), whereas angular momentum depends on both coefficient of restitution and the rotation rate. Angular momentum is nearly independent of e_n for small gap-widths as there are few particle-particle collisions compared to particle-wall collisions. Coming back to large gap-width, angular momentum decreases with increasing $\tilde{r}$ for low ω_i, as shown in Fig. 4.7(c, e), due to rapid decrease of velocity (see Fig. 4.6(c, e)) compared to $\tilde{r}$. The constant density for low rotation rates throughout $\tilde{r}$ shown in Fig. 4.2(c, e) does not not affect $l(\tilde{r})$. Similarly for higher dissipation ($e_n = 0.6$), the increase in density and $\tilde{r}$ is much higher compared to decrease in V_θ which results in a profile as shown in Fig. 4.7(a) similar to density.

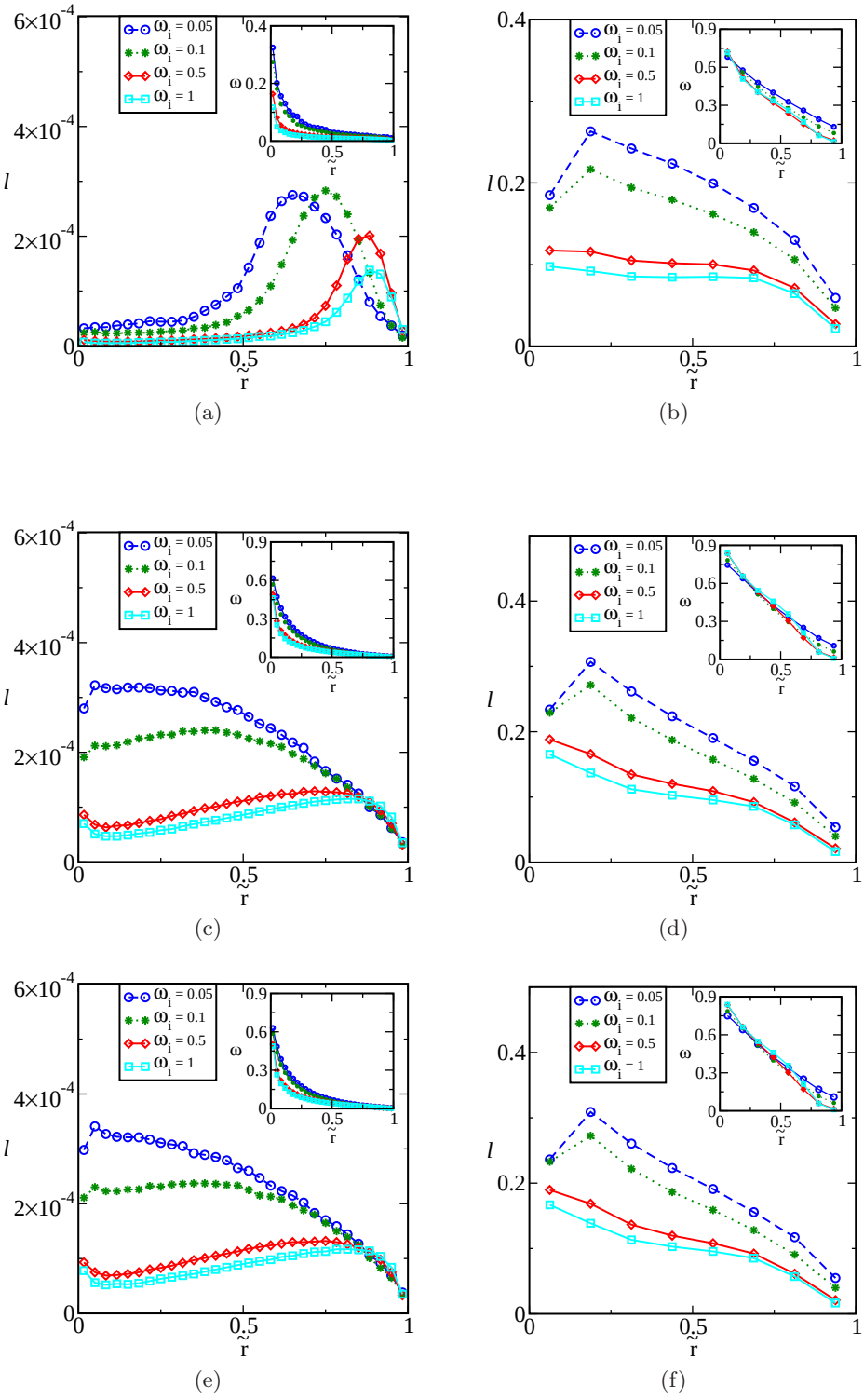

Figure 4.7: Radial variation of angular momentum and angular velocity (inset) for parameter values same as in Fig. 4.2.

Granular temperature

Figure 4.8$(a-f)$ shows the radial variation of granular temperature. The temperature is lower for dissipative systems as seen in Fig. 4.8(a) due to the continuous loss of energy on collisions, which is not prominent in small gap limit [.i.e. at $Kn \sim O(1)$] as shown in Fig. 4.8(b). Also,

a small addition of inelasticity into the system ($e_n = 0.99$) does not not affect the temperature due to relatively less particle-particle collisions as evident from the Fig. 4.8(c) when compared to the elastic case in Fig. 4.8(e).

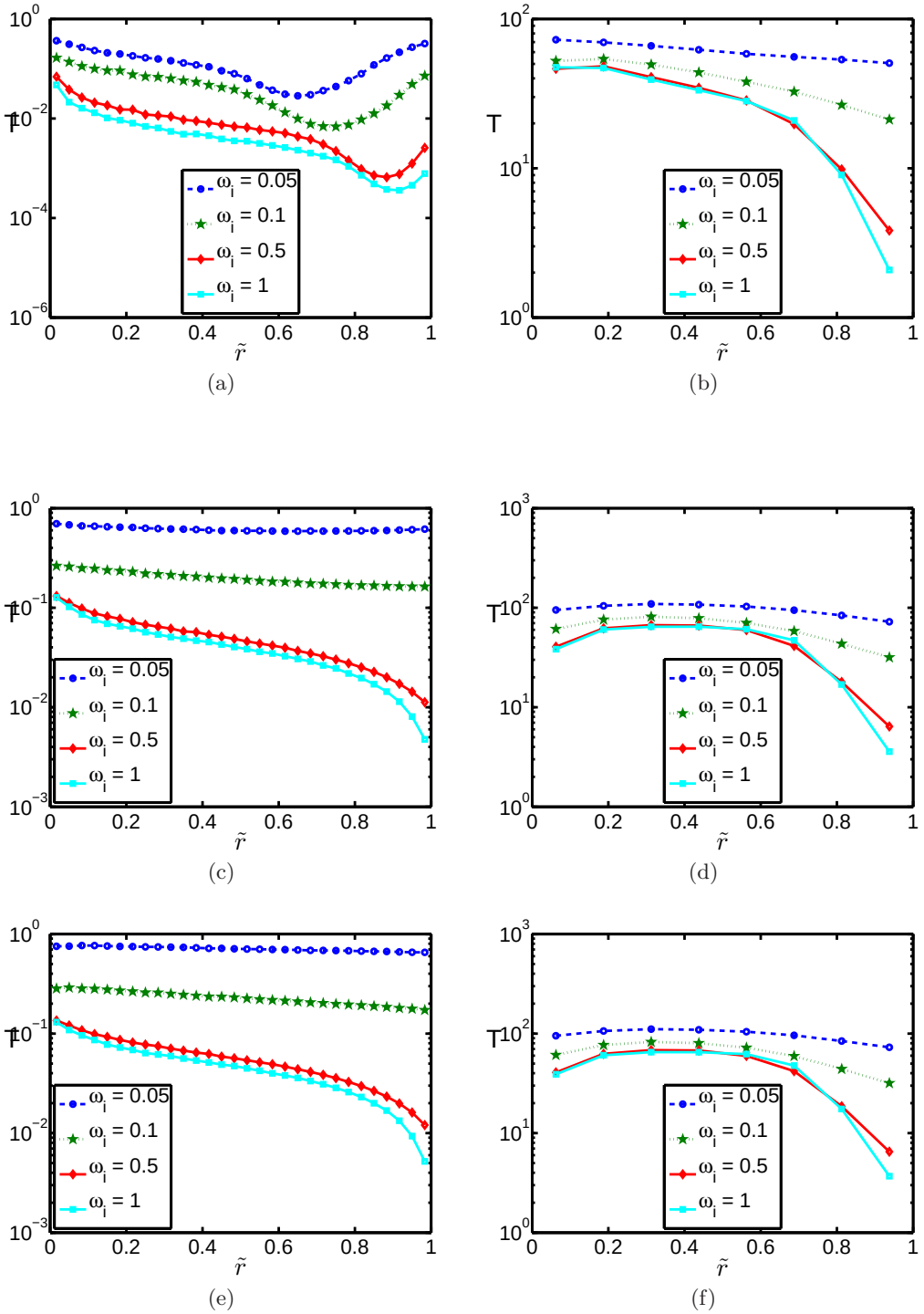

Figure 4.8: Radial variation of granular temperature for parameter values as in fig. 4.2.

The granular temperature appears to be constant for lower values of rotation rates ($\omega_i = 0.05, 0.1$) for non-dissipative and moderately dissipative system due to the homogeneous distribution of particles as shown in Fig. 4.2(c, e), but on observing individual profiles for high

rotation rates at low dissipation as in Fig. 4.8(c) and (e), the temperature decreases with increasing $\tilde{r}$ which is due to large number of particle-particle collisions. The density in Fig. 4.3(c) and (e) increases with radius. This increase in number of particles locally causes a decrease in temperature. The rarefied regime will have a higher temperature which can be seen near the inner cylinder. Similar inferences can be drawn for highly dissipative systems as shown in Fig. 4.8(a)

4.1.2 Hydrodynamic profiles ($\nu_{av} = 0.1$)

$d_w = 75, N = 3788$			$d_w = 10, N = 780$
e_n	ω_i	Kn	Kn
0.6	0.05	0.0000154	0.07
	0.1	0.000053	0.067
	0.5	0.000079	0.053
	1	0.000121	0.53
0.99	0.01	0.031	0.297
	0.1	0.031	0.33
	0.5	0.0254	0.375
	1	0.022	0.395
1	0.01	0.031	0.296
	0.1	0.031	0.332
	0.5	0.0256	0.376
	1	0.0226	0.396

Table 4.2: Parameters used in simulations to vary the mean Knudsen number for mean density $\nu_{av} = 0.1$, $R_o = 100$ ($d_w = R_o - R_i$) and $\omega_o = 0$

In this section, an average density of $\nu_{av} = 0.1$ is simulated with inner cylinder rotating at different speeds $\omega_i = 0.05 - 1$. The rest of the parameters has been fixed (see table 4.2). The number of partticles (N) simulated varies from 3788 for the largest gap-width ($d_w = 75$) to 780 for the smallest gap-width ($d_w = 10$) considered in this study.

Density

High density system will have a different mechanism as dissipation will become more dominant. This is visible from F Fig. 4.9(b), where a small bump in density near the centre is present for a small gap-width system, which was absent for low mean density ($\nu_{av} = 0.05$) in the previous section. This maxima is due to dissipation induced clustering which usually occurs due to frequent interaction of particles with each other. The rarefaction effects were more prominent in the lower density case, whereas, dissipation effects starts to dominate at high and moderate densities. Fig. 4.9(b) shows that the density variation becomes more significant with further increase in mean density. In general, the steady-state results show the two distinct regions as expected: a high-velocity and dilute-gas-like kinetic region near the moving wall and a high-solid-fraction liquid-like frictional flow regime away from the moving wall as shown in snapshots in Fig. 4.10.

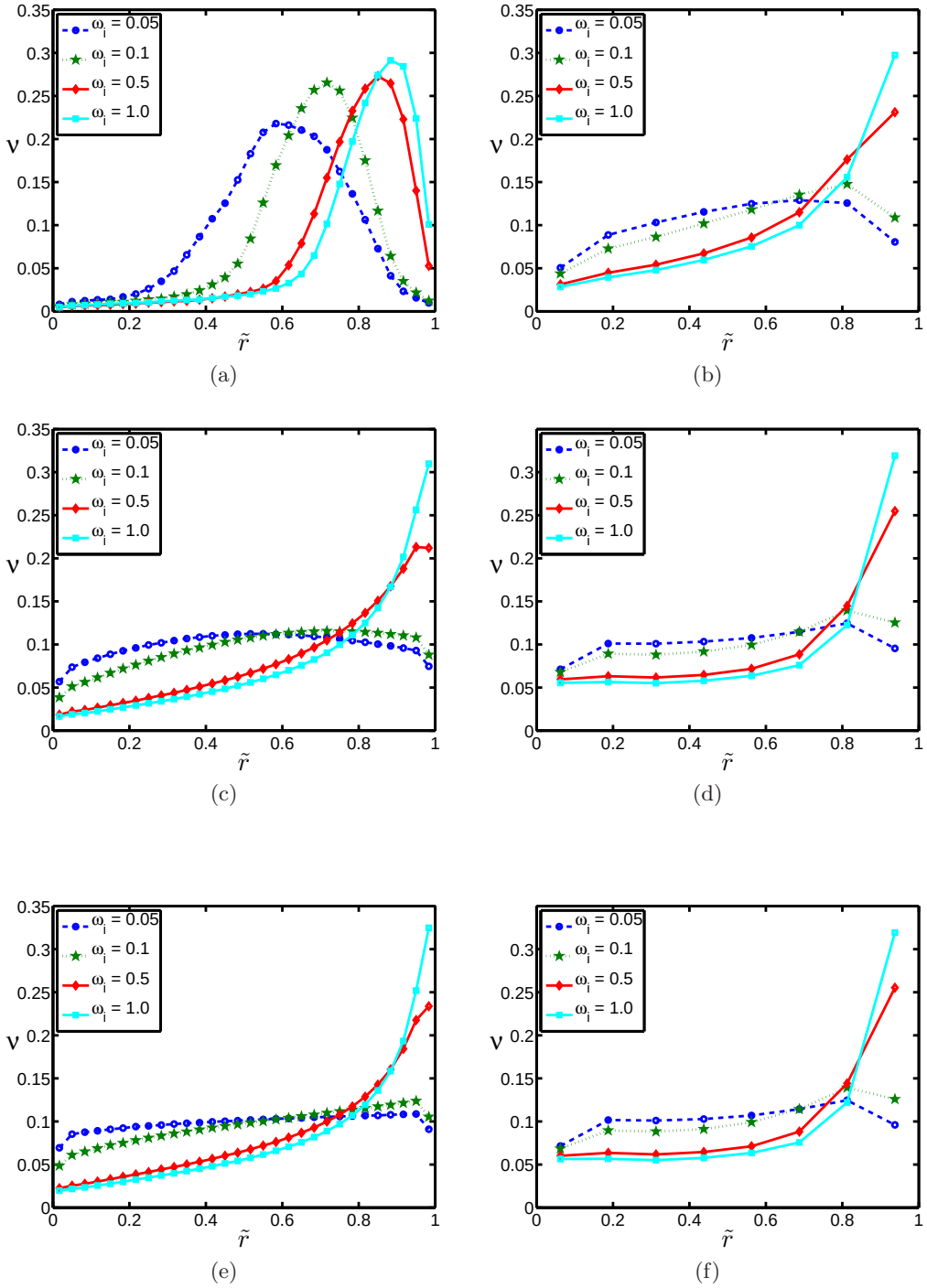

Figure 4.9: Radial variation of density for parameter values outer radius $R_o = 100$, gap-width (a, c, e) $d_w = 75$, (b, d, f) $d_w = 10$, mean density $\nu_{av} = 0.1$ and (a, b) $e_n = 0.6$, (c, d) $e_n = 0.99$ and (e, f) $e_n = 1$.

Figure 4.10 shows different phases of cluster in 2D annular flow with inner cylinder rotating and fixed outer cylinder. The snapshots are for $\nu_{av} = 0.1$, $\omega_i = 0.1$ and $e_n = 0.6$, moving in an anti-clockwise direction. The initial phase is the formation stage, where all the particles agglomerate to form a single cluster (*multiple small clusters* $\rightarrow$ *single large cluster*)as shown in Fig 4.10(a). The second stage is where they move as a single cluster. At certain instant, the cluster become extremely compact to move as a single structure and no longer able to sustain

the momentum and energy. The stretching up of the cluster takes place at this stage as seen in Fig. 4.10(c) which is followed by breaking again as shown in Fig. 4.10(d). The cluster velocity is observed to decrease with increase in the particle number. With high density, the cluster gets more bulky and less agile and high particle-particle interaction makes it slower compared to $\nu_{av} = 0.05$.

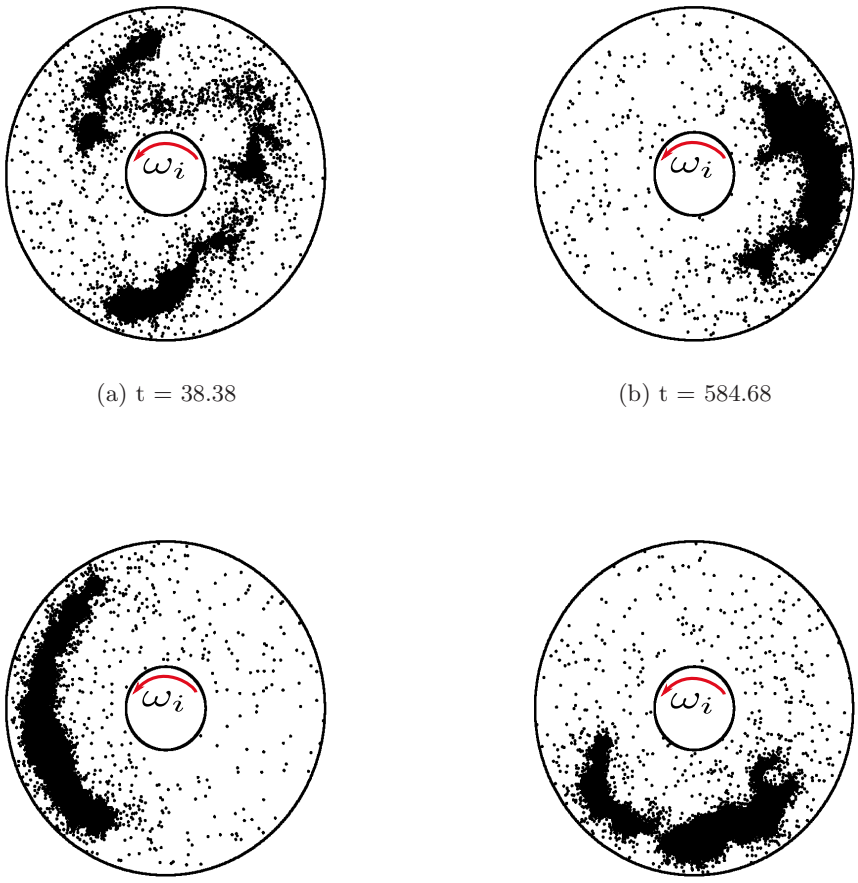

(a) t = 38.38 (b) t = 584.68

(c) t = 778.79 (d) t = 863.59

Figure 4.10: Snapshots showing different stages of cluster for an inelastic system - *stretching*(b, c), *compression*(d) *and breaking*(a). Parameter values are same as in Fig. 4.9 for $\omega_i = 0.1$ and $e_n = 0.6$.

Typical snapshots for elastic case is also shown in Fig. 4.11. The homogeneity in particle distribution is trivial and can be seen from Fig. 4.9(e, f). The maxima at the outer boundary at higher ω_i is again due to the increase in centrifugal force acting on each particle which diffuses due to paticle-particle collision.

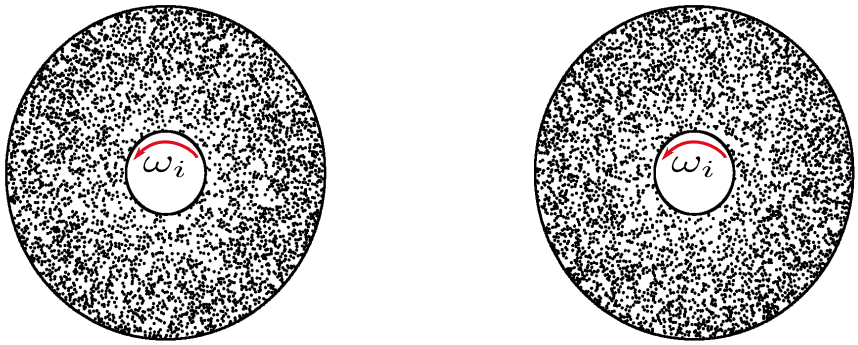

(a) t = 18.43 (b) t = 34150.73

Figure 4.11: Snapshots showing particle positions at different time for an elastic system. Parameter values are same as in Fig. 4.9 for $\omega_i = 0.1$ and $e_n = 1.0$.

Velocity and angular momentum

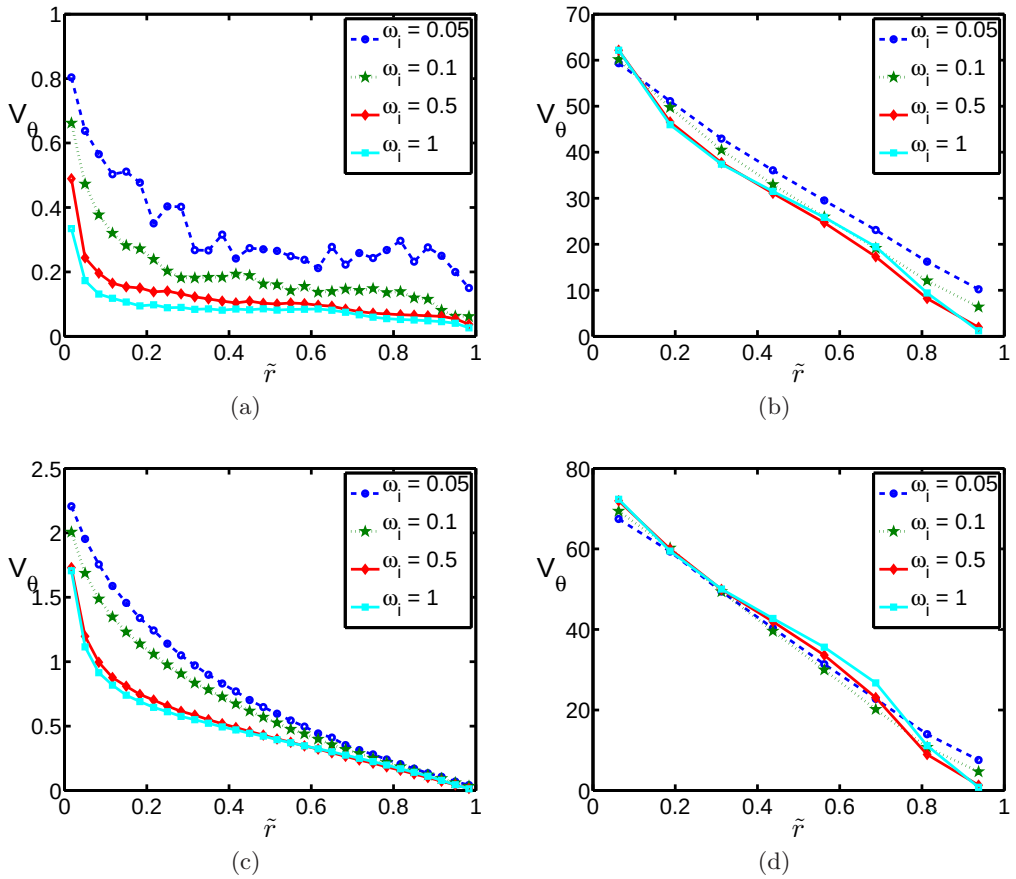

(a) (b)

(c) (d)

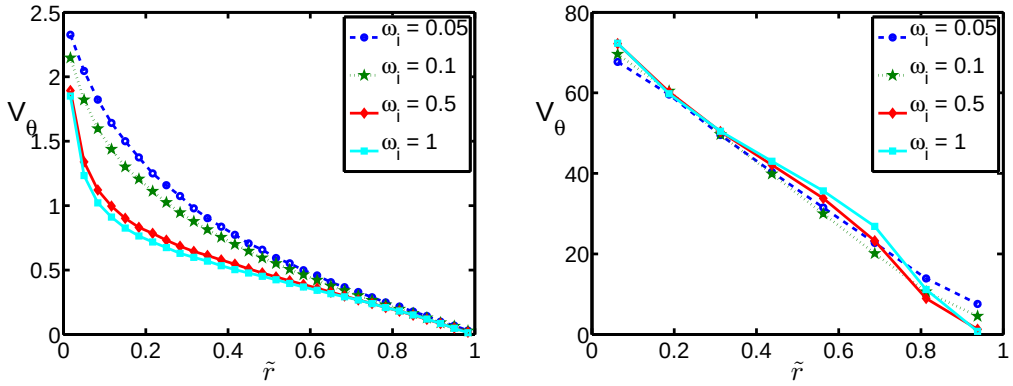

(e) (f)

Figure 4.12: Radial variation of azimuthal velocity. Parameter values are same as in Fig. 4.9.

The velocity profile is similar to irrotational vortex flow ($V_\theta \sim \frac{1}{r}$), for an unbounded liquid with inner cylinder rotating. In the narrow gap limit, the profiles falls linearly radially approaching plane Couette flow and is evident from the Fig. 4.12(e, f). The velocity profile in Fig. 4.12(a) for higher ω_i becomes almost constant within a certain range, where the clustering is taking place. The radial range of constant velocity is larger compared to the low density case in the previous section. The velocity drops after $\tilde{r} \sim 0.9$ and approaches the value of slip velocity at the wall. Another important observation is the coinciding of velocity profiles for small gap limit as can be seen in Fig. 4.11(b, d). The velocities are linear for small gap-widths, showing that the rarefaction effects are not prominent at this Knudsen number. The Kn for all these cases are lower compared to low density simulated in the previous section.

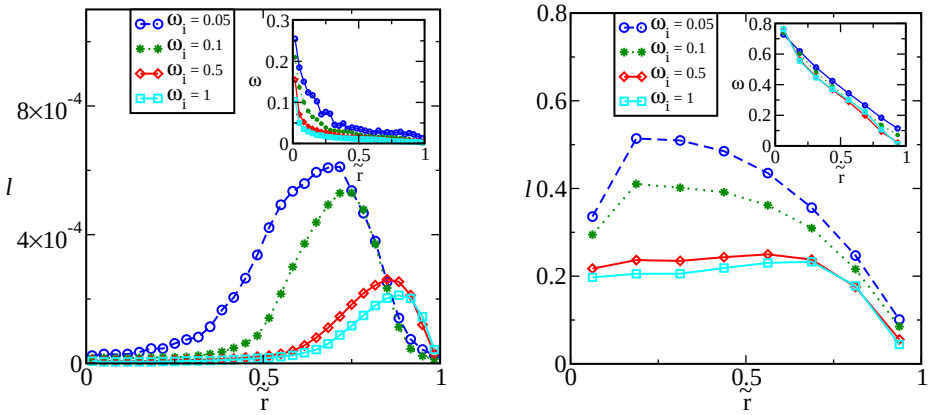

(a) (b)

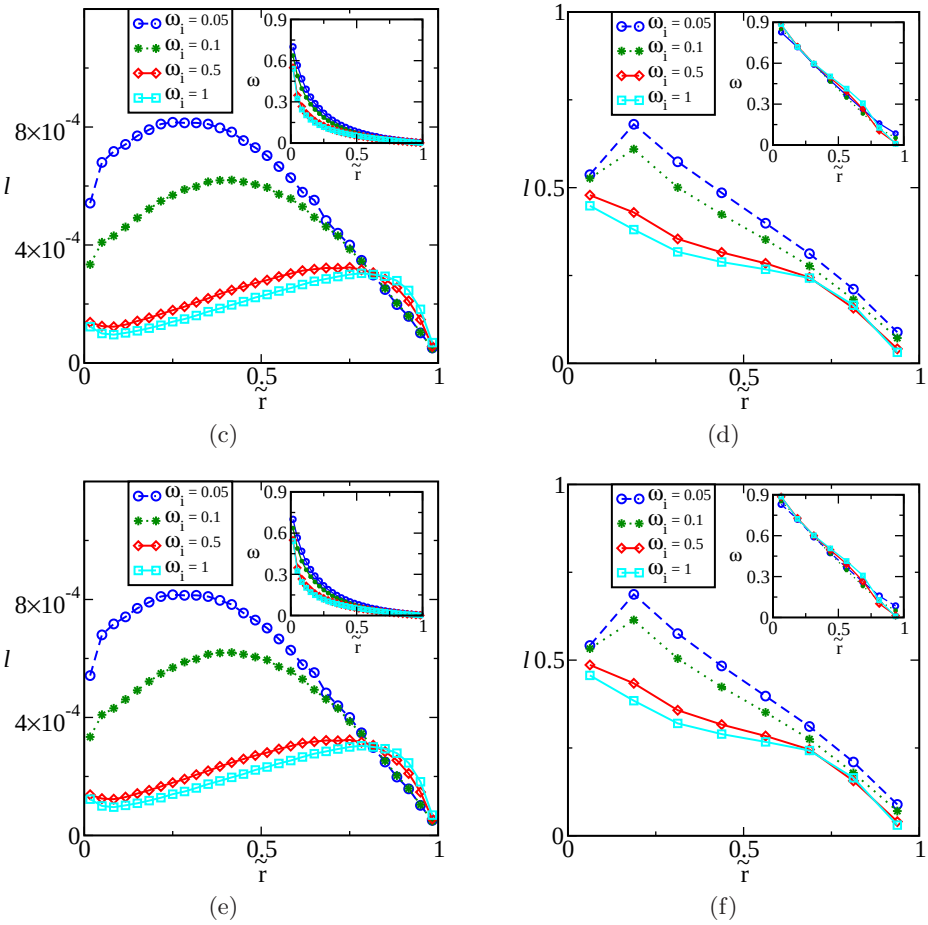

Figure 4.13: Radial variation of angular momentum and angular velocity (inset) for parameter values same as in Fig. 4.9.

Figure 4.13 shows the radial variation of angular momentum and angular velocity for $\nu_{av} = 0.1$. The qualitative behavior of the both momentum and velocity are similar for small gap-width except for $e_n = 0.6$ as shown in Fig. 4.13(b) where the dissipation effects are considerable. The lower momentum near the outer wall is due to lower velocity and low density region near the outer wall for $\omega_i = 0.05$ &0.1. Even though the density near the outer wall for $\omega_i = 0.5$ &1 is higher than the bulk, the velocities are small that the system ends up having a lower angular momentum near the outer wall. Also, the angular momentum in $(a - f)$ for lower rotation rates $\omega_i = 0.05$ &0.1 is higher near the inner wall compared to high rotation rates, due to the combined effect of both high density region (see Fig. 4.9) and high angular velocity (see inset Fig. 4.13) near the inner wall which results in a higher angular momentum near the inner wall for $\omega_i = 0.05$ & 0.1.

Granular temperature

Figure 4.14$(a - f)$ shows the radial variation of granular temperature. The temperature is lower for dissipative systems as in Fig. 4.6(a) due to continuous loss of energy on collisions, which is not prominent in small gap-width as in Fig. 4.14(b). Also, even a small addition of inelasticity into the system ($e_n = 0.99$) does not affect the temperature of the system due to relatively less particle-particle collisions as evident from Fig. 4.14(d, f).

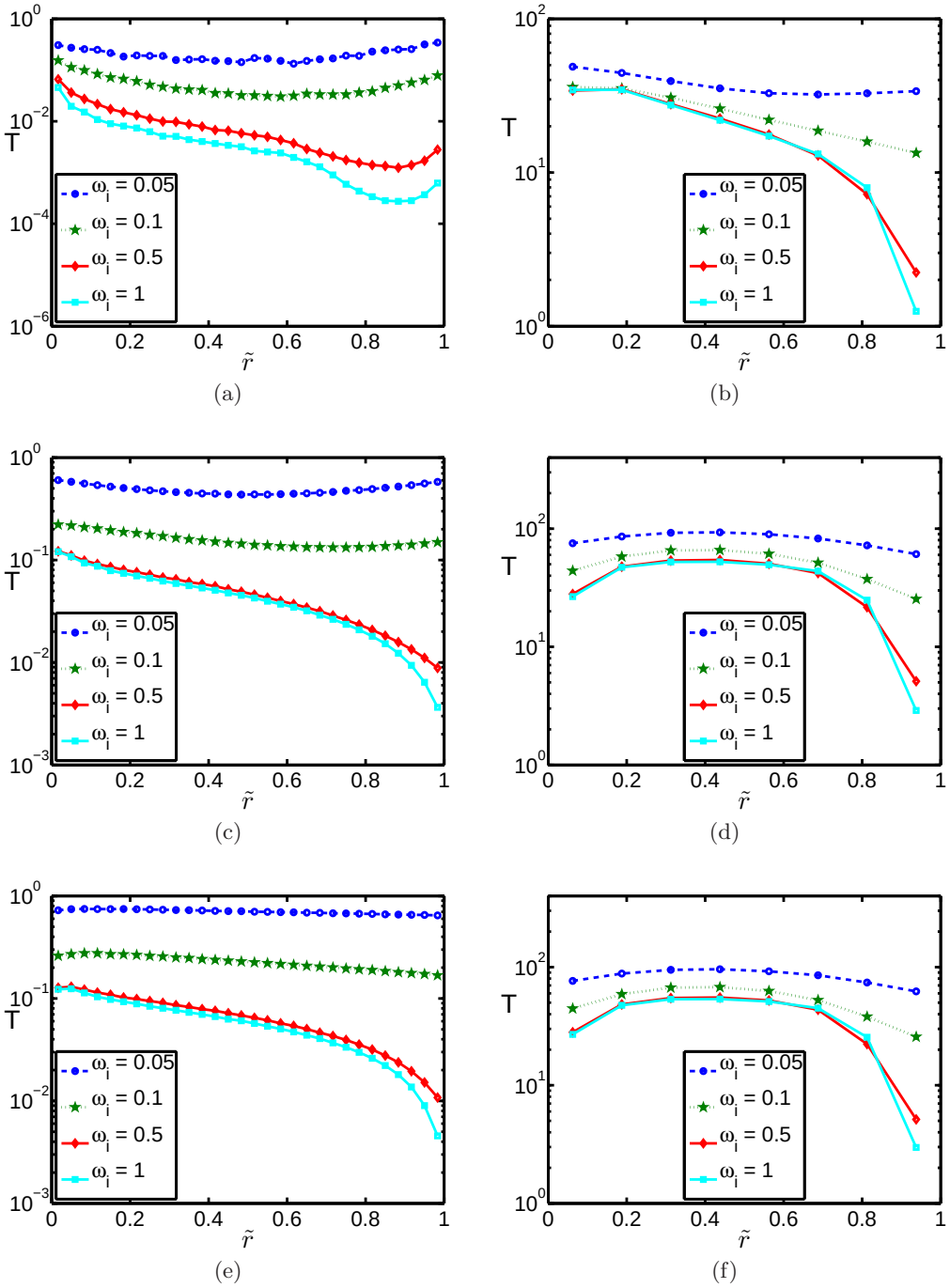

Figure 4.14: Radial variation of granular temperature. Parameter values are same as in Fig. 4.9.

Concentrating on the temperature for large gap-width and high ω_i for moderately dissipative system ($e_n = 0.99$), the inertial force pushes the particles to move towards the outer boundary. This causes a build-up of particles and the resulting increased dissipation leads to lower temperature as shown in Fig 4.15(d). The temperature shows linear decrease with radius except closer to the inner boundary where rarefaction effects are dominant. At lower ω_i, the particles accumulate near the centre and cause an increase in the local density and a simultaneous decrease in temperature as shown in Fig. 4.15(b).

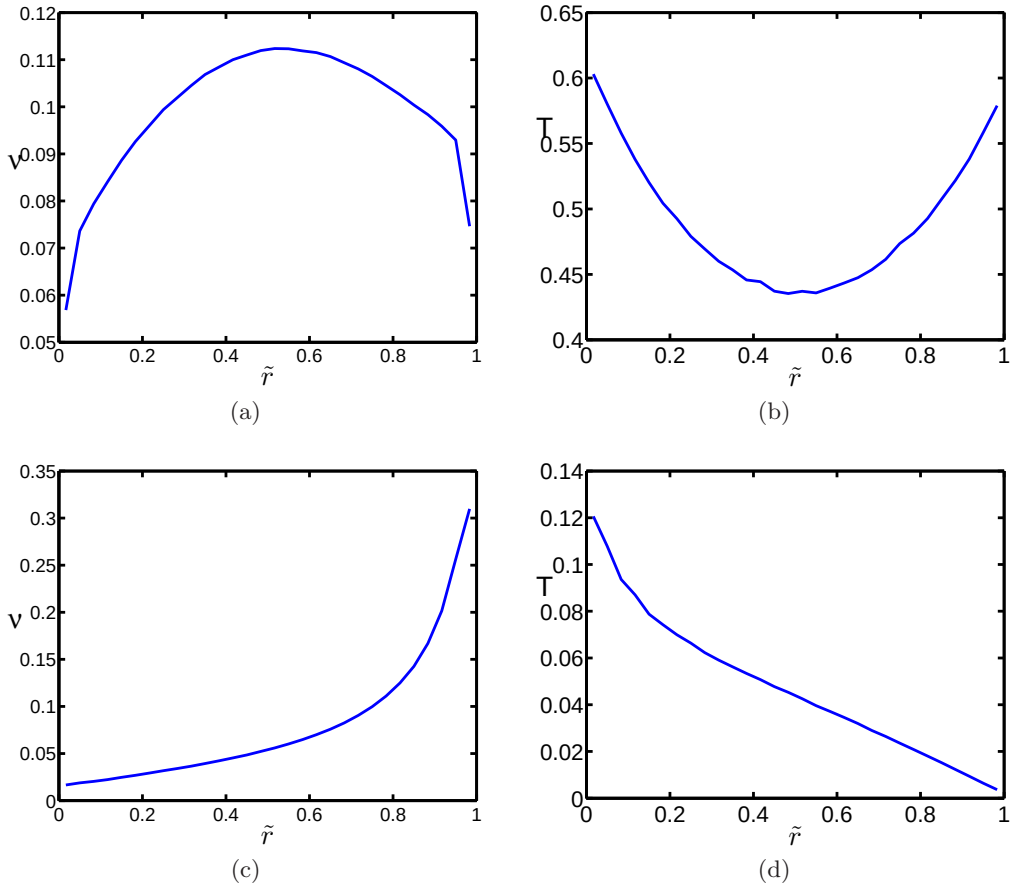

Figure 4.15: Radial variation of density for ($e_n = 0.99$) and parameter values same as in Fig. 4.9, (a) $\omega_i = 0.05$ and (c) $\omega_i = 1.0$. Radial temperature profiles for $e_n = 0.99$ and parameter values same as in Fig. 4.9 for (b) $\omega_i = 0.05$ and (d) $\omega_i = 1.0$.

4.1.3 Hydrodynamic profiles ($\nu_{av} = 0.4$)

In this section, an average density of $\nu_{av} = 0.4$ is simulated with inner cylinder rotating at different speed $\omega_i = 0.05 - 1$. The rest of the parameters has been fixed (see table 4.3). The number of partticles (N) simulated varies from 15072 for the largest gap-width ($d_w = 75$) to 3036 for the smallest gap-width ($d_w = 10$) considered in this study.

Density

The clustering effect becomes more prominent for the highest density case shown here. Even for the small gap-width at low rotation rate, a maxima in density can be observed in Fig. 4.16(b), which wasn't significant in the previous two cases ($\nu_{av} = 0.05$ and $\nu_{av} = 0.1$). The dissipation effects are driving the system for the small gap-width, even though wall-particle collisions are non-negligible (about 5-8%). At higher ω_i, centrifugal forces overcome the dissipative forces and result in a density maxima near the outer cylinder. For large gap-width, the density maxima for the low rotation rate occurs near the centre because the inertial force is not sufficient enough to move the particles towards the outer cylinder, which can be shown in Fig. 4.16(c) for $\omega_i = 0.05$. Even a small amount of dissipation into the system as shown in Fig. 4.16(c) lead to a clustering of particles, thereby showing a density maxima near the centre. For small gap-widths as in

$d_w = 75, N = 15072$			$d_w = 10, N = 3036$
e_n	ω_i	Kn	Kn
0.6	0.05	$8.21\times\ 10^{-7}$	0.0694
	0.1	$1.01\times\ 10^{-6}$	0.067
	0.5	$1.91\times\ 10^{-6}$	0.058
	1	$2.85\times\ 10^{-6}$	0.054
0.99	0.05	0.0035	0.049
	0.1	0.00375	0.061
	0.5	0.0031	0.071
	1.0	0.0023	0.075
1	0.05	0.0041	0.048
	0.1	0.0042	0.059
	0.5	0.0035	0.071
	1	0.0030	0.074

Table 4.3: Parameters used in simulations to vary the mean Knudsen number for mean density $\nu_{av} = 0.4$, $R_o = 100(d_w = R_o - R_i)$ and $\omega_o = 0$.

Fig. 4.16(d) and (f), the density peak occurs at the outer wall. Another important feature is the shift of the density maximum towards the inner wall on increasing dissipation. This is possibly due to the lower momentum of the gaseous region near the inner wall (see Fig. 4.25). The momentum transferred from the inner wall to the cluster through the gaseous region is the only source of energy for the cluster which is lower compared to the case where $e_n = 0.99$. This is also seen from the granular temperature plots in Fig. 4.27 where the temperature near the wall and the clustered region for $e_n = 0.6$ (see Fig. 4.27(a)) is much lower than the temperature in Fig. 4.27(c).

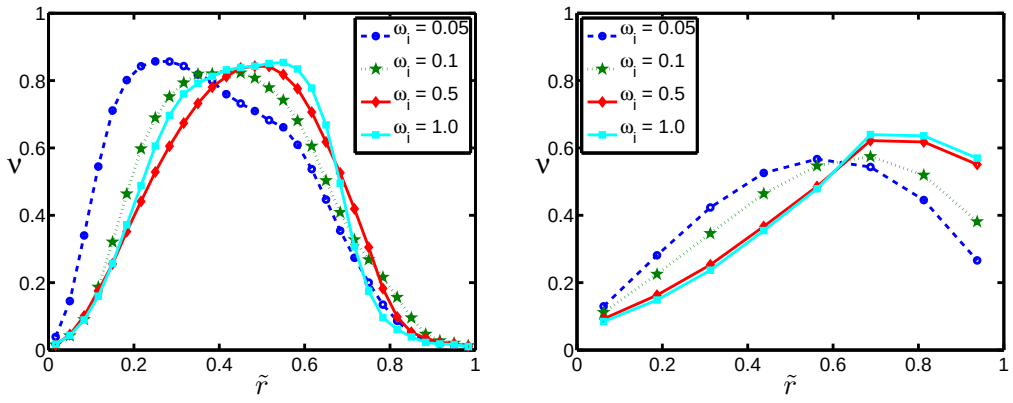

(a) (b)

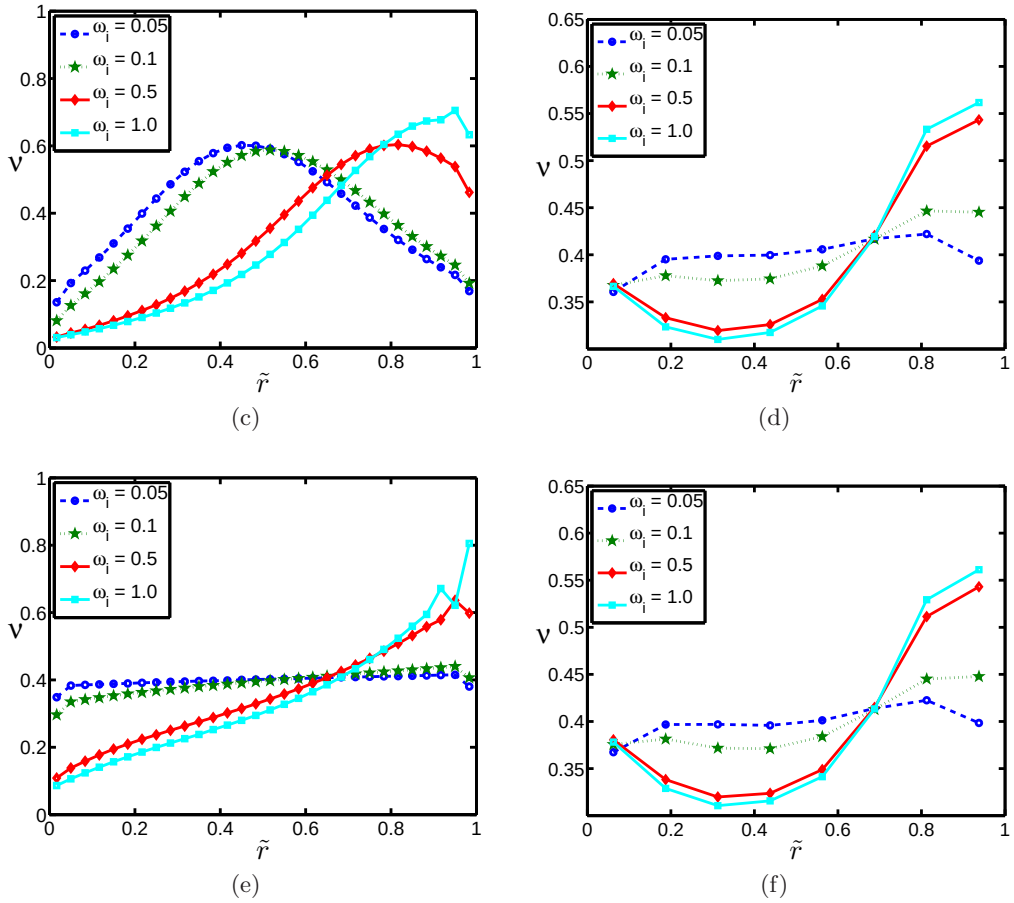

Figure 4.16: Radial variation of density for parameter values outer radius $R_o = 100$, gap-width (a, c, e) $d_w = 75$, (b, d, f) $d_w = 10$, mean density $\nu_{av} = 0.4$ and (a, b) $e_n = 0.6$, (c, d) $e_n = 0.99$ and (e, f) $e_n = 1$.

An interesting feature observed at high density ($\nu_{av} = 0.4$) is the slow movement of the cluster and the co-existence of a solid and a gas regime. A single cluster revolving slowly around the innner cylinder is observed to behave like a solid as seen in snapshots of particle position in Fig. 4.18 at different time for $\omega_i = 0.1$. This behaviour is also evident from the velocity profiles which shows the tangential velocity approaching zero at $\tilde{r} = 0.2$ in Fig. 4.25(a). This peculiar property of driven granular particles to undergo transition from a liquid to a solid-like state has also been observed recently by Peters *et al.* (2016) in a Taylor-Couette setup.

The centre-of-mass of all particles is defined as:

$$x_{cm} = \frac{\sum_{i=1}^{N} m_i x_i}{\sum_{i=1}^{N} m_i}, \quad y_{cm} = \frac{\sum_{i=1}^{N} m_i y_i}{\sum_{i=1}^{N} m_i}. \tag{4.3}$$

Figures 4.17(a) and (b) show the radial and azimuthal movement of the centre-of-mass over a period of $N \times 40000$ collisions respectively. The cartesian components in Eq. 4.3 are converted to polar components by the following expressions.

$$r_{cm} = \sqrt{x_{cm}^2 + y_{cm}^2}, \quad \theta_{cm} = tan^{-1}\left(\frac{y_{cm}}{x_{cm}}\right) \tag{4.4}$$

where r_{cm} is non-dimensionalised by the diameter of the particle (d_p). The continual increase of r_{cm} with time in Fig. 4.17(a) suggests that the particle distribution is not symmetric around the azimuthal direction as it is evident from snapshots in Fig. 4.18.

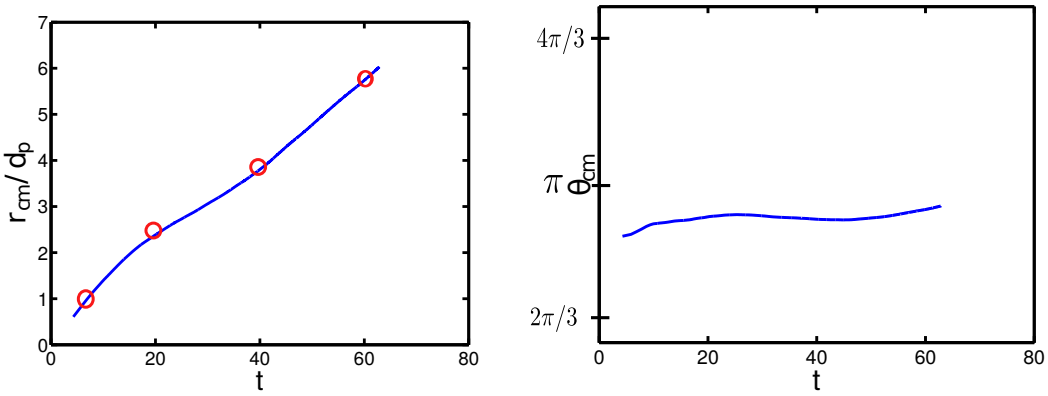

(a) (b)

Figure 4.17: Temporal evolution of the centre-of-mass of the system in the (a) radial (r_{cm}), (b) azimuthal (θ_{cm}) direction for $\omega_i = 0.1$. Parameter values are same as in Fig. 4.16 with $e_n = 0.6$.

Figure 4.18 shows the temporal evolution of the system at $\nu_{av} = 0.4$ with $\omega_i = 0.1$ and $e_n = 0.6$. No intermediate stages are observed as seen in the previous section for $\nu_{av} = 0.05$ and 0.1. One single large cluster at different time intervals moves slowly due to the centrifugal force imparted by the inner cylinder. Two regions of granular gas are observed near the outer and inner walls, which may be responsible to impart the momentum gained from the rotation to the giant inner cluster.

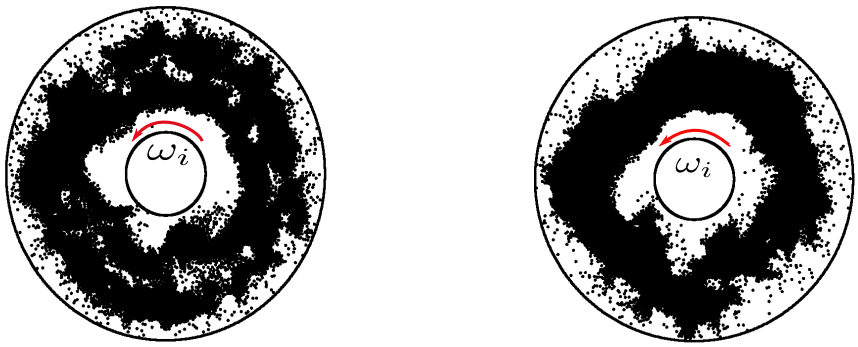

(a) t = 4.28 (b) t = 20.59

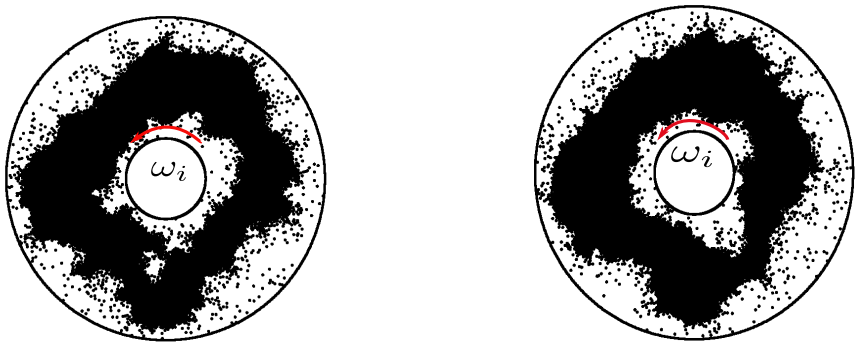

(c) t = 40.13 (d) t = 62.86

Figure 4.18: Snapshots showing different stages of cluster *co-existence of gas + solid* at different times marked in Fig. 4.17(a) (red points). Parameters are same as in Fig. 4.16 for $\omega_i = 0.1$, $d_w = 75$ and $e_n = 0.6$.

A further slowing down has been observed for higher rotation rate ($\omega_i = 1$) in Fig. 4.19(a). While Fig. 4.17(a) indicates a continual movement of the cluster towards the outer wall, Fig. 4.19(a) at $\omega_i = 1.0$ indicates that the centre-of-mass of the cluster seems to have reached a quasi-steady state (in terms of its radial position) after $t = 150$. The slow inner and outer movement of the cluster is expected as the centrifugal force is smaller in Fig. 4.17(a) compared to Fig. 4.19(a). The four snapshots in Fig. 4.20, for times marked by red points in Fig. 4.19(a), depict the motion of the cluster towards the outer disk due to high centrifugal force followed by motion towards the inner disk. The collective inner motion is due to the gain of thermal energy from the outer wall (thermal walls) after losing all the momentum from collisions near the outer boundary. This gain of energy allows the cluster to move inwards followed by a solid-like behaviour near the inner wall.

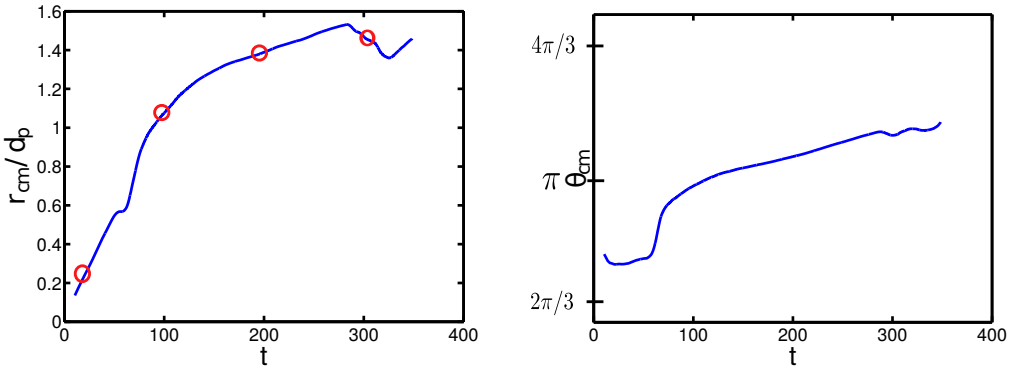

(a) (b)

Figure 4.19: Temporal evolution of the centre-of-mass of the system in the (a) radial (r_{cm}), (b) azimuthal (θ_{cm}) direction for $\omega_i = 1$. Parameter values are same as in Fig. 4.16 with $e_n = 0.6$.

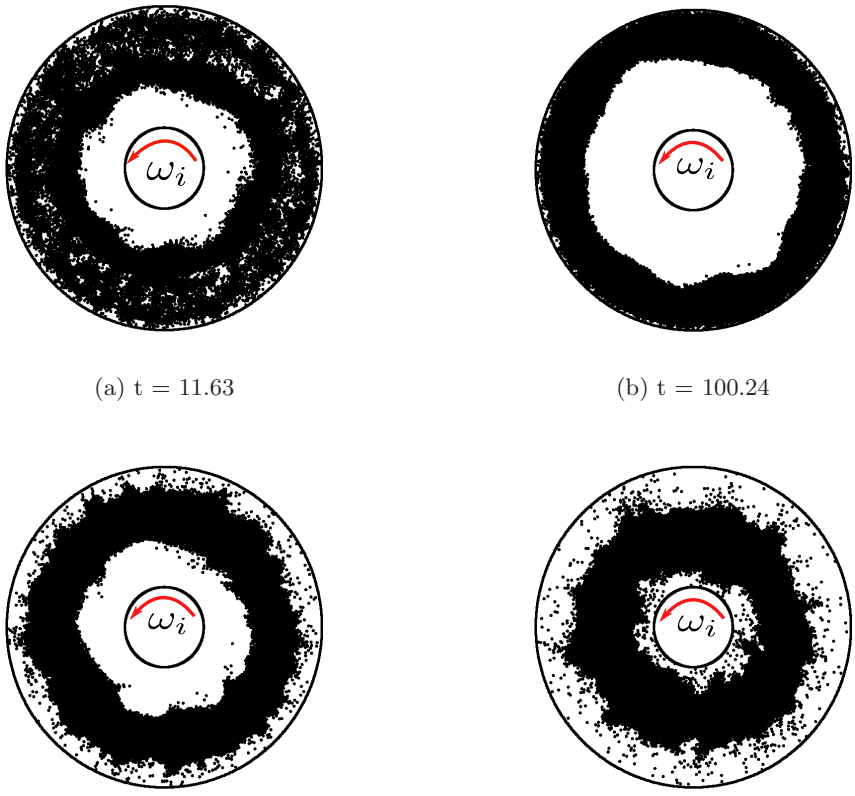

(a) t = 11.63 (b) t = 100.24

(c) t = 200.48 (d) t = 300.15

Figure 4.20: Snapshots showing different stages of cluster at different times marked in Fig. 4.19(a) (red points). Parameters are same as in Fig. 4.19.

A similar analysis for $e_n = 0.99$ shows that the cluster has reached a steady state and the centre-of-mass fluctuates around a mean value as shown in Fig. 4.21(a) and Fig. 4.23(a) Figure 4.22 shows typical snapshots of particles for $e_n = 0.99$ and low centrifugal force ($\omega_i = 0.1$). A clear dense region near the centre of the annulus can be seen throughout the simulation which can also be seen in the density profiles in Fig. 4.16(c) for $\omega_i = 0.1$.

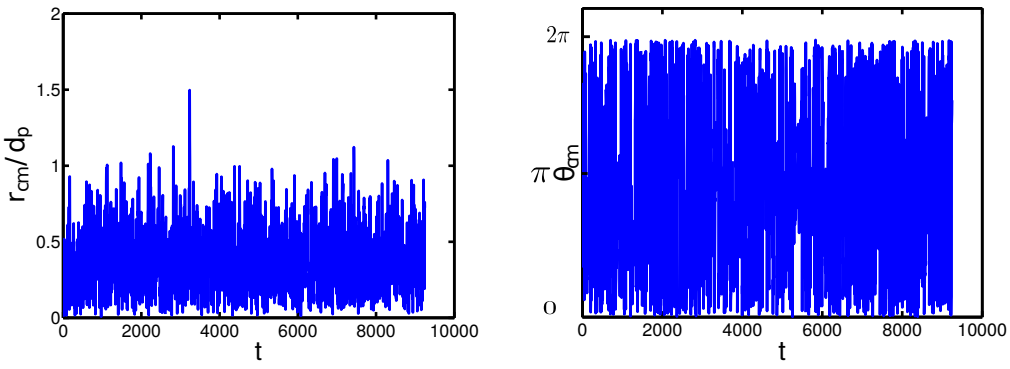

(a) (b)

Figure 4.21: Temporal evolution of the centre-of-mass of the system in the (a) radial (r_{cm}), (b) azimuthal (θ_{cm}) direction for $\omega_i = 0.1$. Parameter values are same as in Fig. 4.16 with $e_n = 0.99$

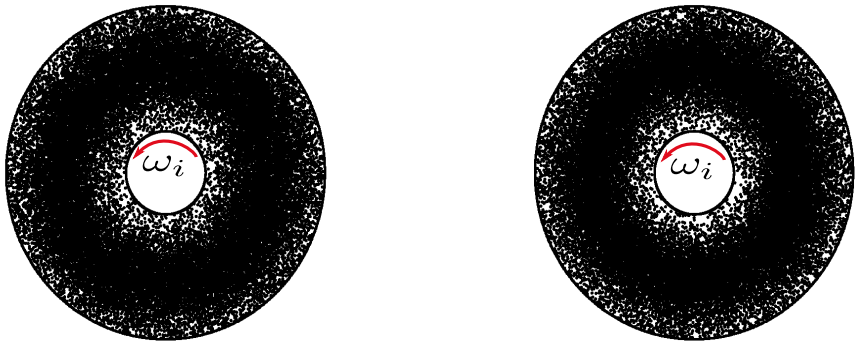

(a) t = 9.18 (b) t = 4623.23

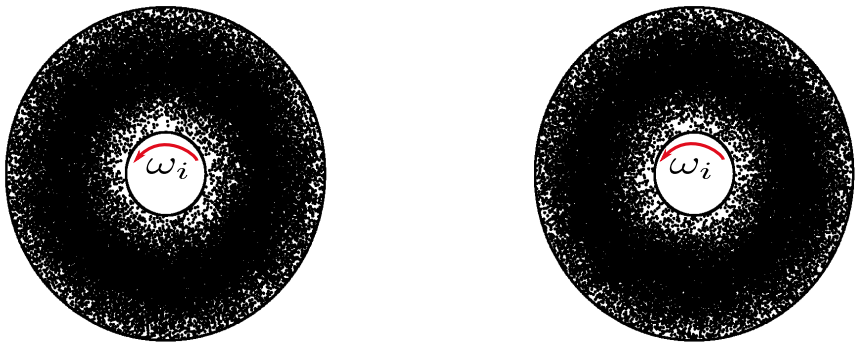

(c) t = 6935.66 (d) t = 9212.44

Figure 4.22: Snapshots showing different stages of cluster at different times. Parameters are same as in Fig. 4.16 for $\omega_i = 0.1$ and $e_n = 0.99$.

For higher rotation rate ($\omega_i = 1$), the cluster stays near the outer wall. Typical snapshots at different times are shown in Fig. 4.24. Clearly a dense clustered region is seen near the outer wall which is due to the combined effect of both dissipation and higher centrifugal force.

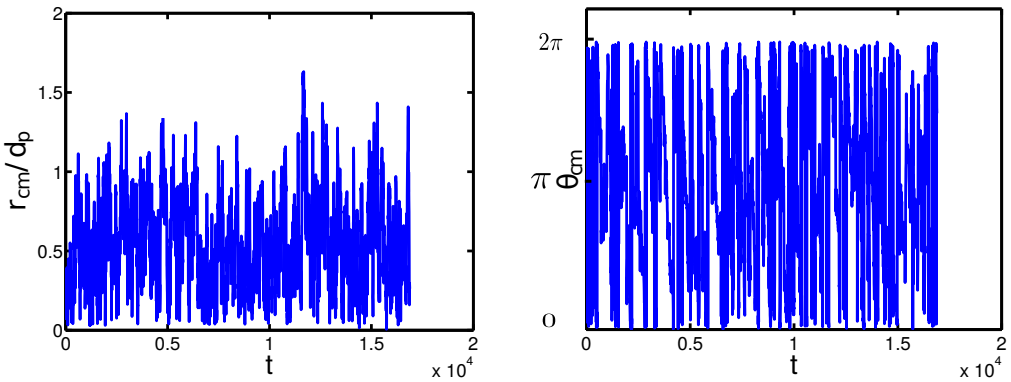

(a) (b)

Figure 4.23: Temporal evolution of the centre-of-mass of the system in the (a) radial (r_{cm}), (b) azimuthal (θ_{cm}) direction for $\omega_i = 1$. Parameter values are same as in Fig. 4.16 with $e_n = 0.99$

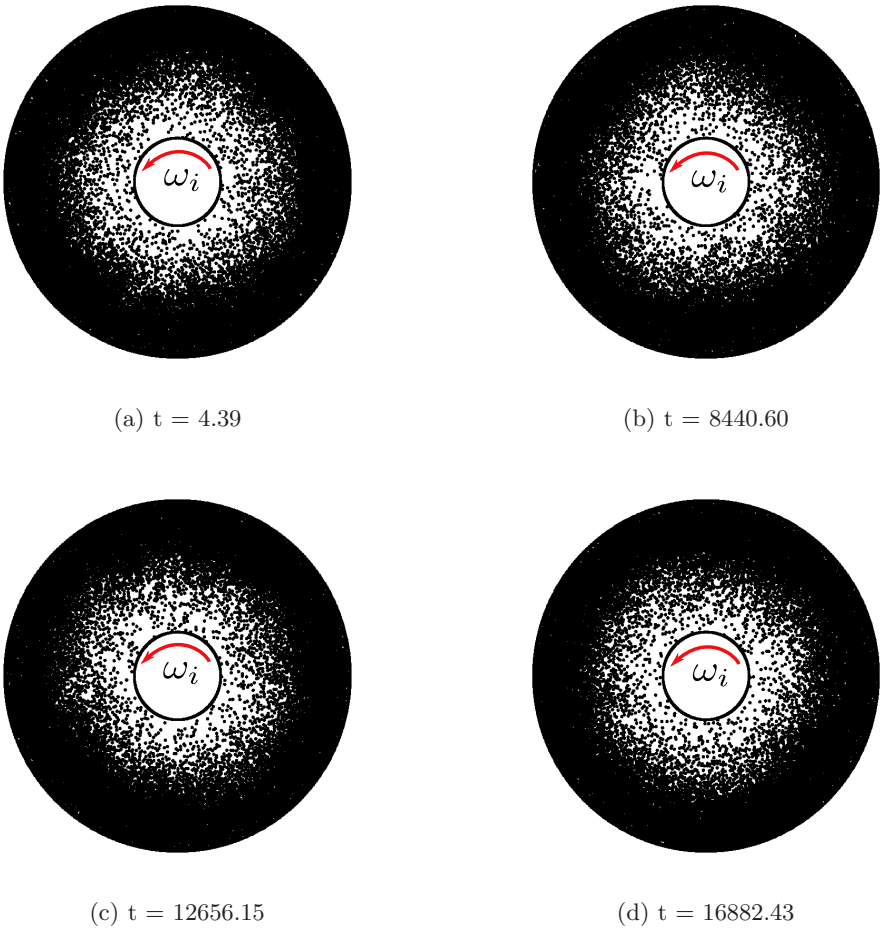

(a) t = 4.39 (b) t = 8440.60

(c) t = 12656.15 (d) t = 16882.43

Figure 4.24: Snapshots showing different stages of cluster at different times. Parameters are same as in Fig. 4.16 for $\omega_i = 1.0$ and $e_n = 0.99$.

Velocity and angular momentum

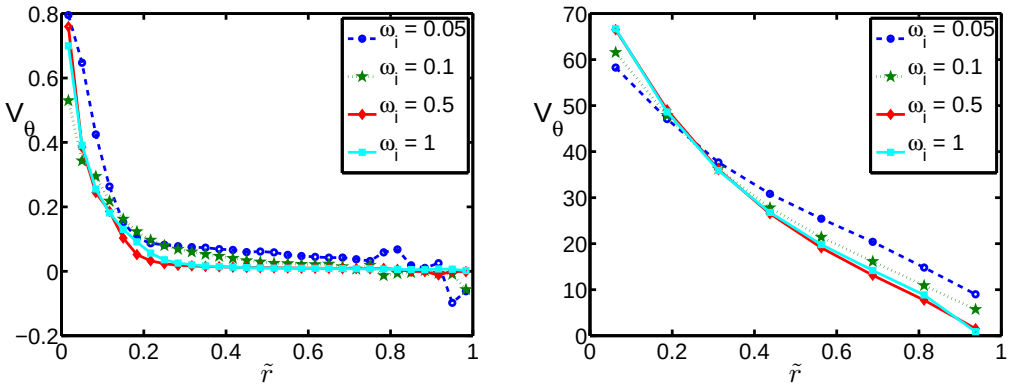

(a) (b)

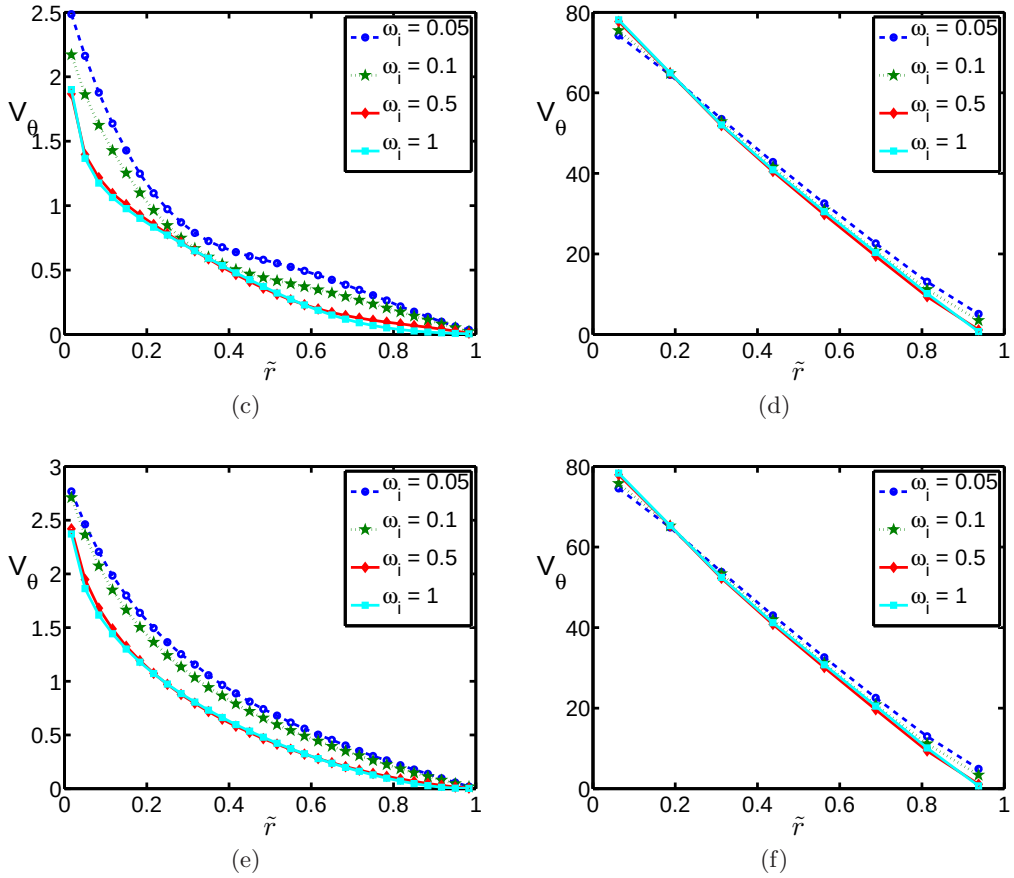

Figure 4.25: Radial variation of azimuthal velocity for parameter values same as in Fig. 4.16.

The azimuthal velocity profiles flattens out and approach zero towards the outer cylinder for the high density case as shown in Fig. 4.25(a). All the profiles start to coincide with each other with the increase in e_n at small gap-widths. The centrifugal force become less dominant at higher densities for $d_w = 10$, which is due to low inertial force required to move the particles towards the outer wall. The profiles also fall on top of each other for large gap-width, but it is more prominent for small gap-widths. The apparent negative slip velocity in Fig. 4.25(a) for low rotation rate ($\omega_i = 0.05$) is due to the small number of particles near the outer walls and is because of the inability to average out fluctuations near the walls. This can also be seen from the snapshots taken at different times in Fig. 4.18.

Figure 4.26 shows the radial variation of angular momentum and angular velocity for high density system ($\nu_{av} = 0.4$). The linear variation of angular momentum for small gap-width as shown in Fig. 4.7(b) and Fig. 4.13(b) is replaced by non-monotonic variation in angular momentum shown in Fig. 4.26(b) due to higher contribution of dissipation even at low gap-width. The prominence of dissipation can be seen in FIg. 4.26(c) where the profiles are completely different from Fig 4.26(e) which was not seen in the earlier cases for $\nu_{av} = 0.05$ and 0.1.

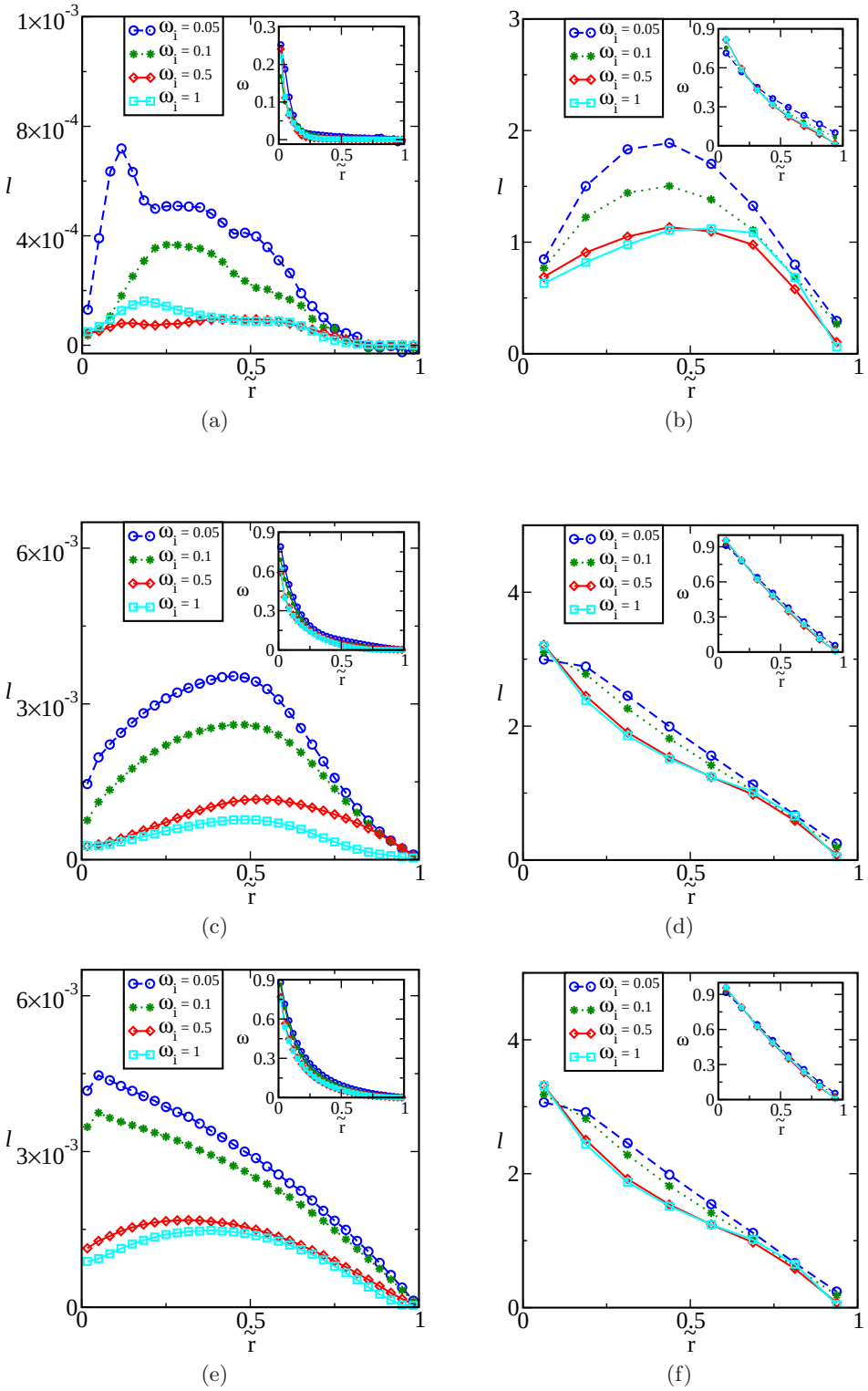

Figure 4.26: Radial variation of angular momentum and angular velocity (inset) for parameter values same as in Fig. 4.16.

Granular temperature

Figure 4.27$(a-f)$ shows the radial variation of granular temperature. We will concentrate on the case of low dissipative system ($e_n = 0.99$). The temperature profiles show a bimodal nature in the case of mild dissipation in the system as shown in Fig. 4.27(c) which is due to the density

maxima near the centre and minima at the walls as shown in Fig. 4.16(c).

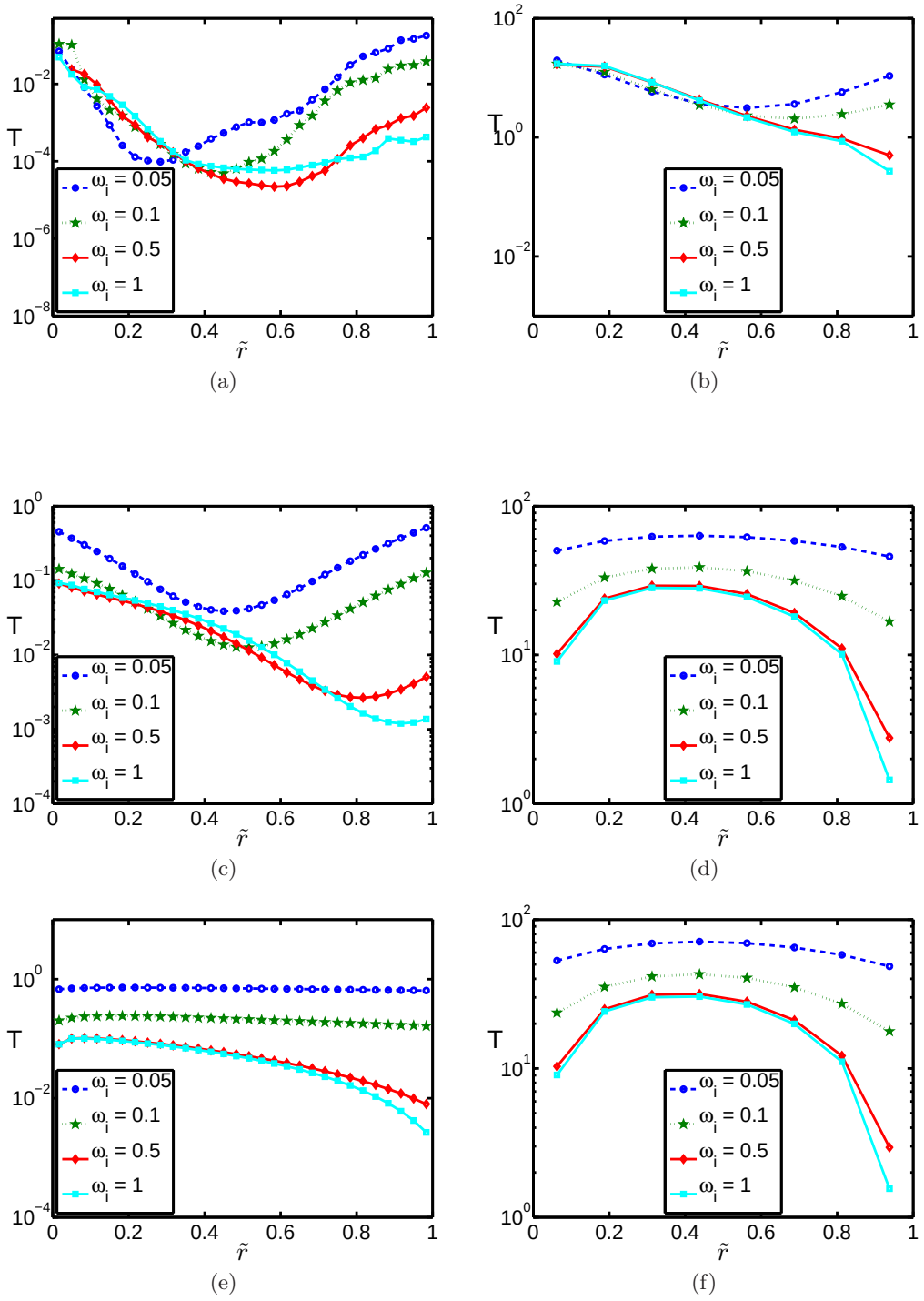

Figure 4.27: Radial variation of granular temperature for parameter values same as in Fig. 4.16.

The central region of the Couette-gap consists of a particle-rich zone (see Fig. 4.22) which leads to more collisions and hence a lower temperature, whereas the region near the walls is particle-depleted and this leads to a higher temperature near the walls as shown by green and blue lines in Fig. 4.27(c). The opposite is true for higher rotation rates where the near-wall (outer cylinder, see Fig. 4.24) region has higher number of particles and more collisions lead to

a lower temperature as shown by red and cyan lines in Fig. 4.27(c). The same trend can also be seen in Fig. 4.27(a) but the fluctuations are higher for highly dissipative systems. It is alse noted that this effect is seen only for the high density system ($\nu_{av} = 0.4$).

A better understanding of the effect of inelasticity on the system can be gained from this case($\nu_{av} = 0.4$). The density profile for $e_n = 0.99$ shows a peak near the centre of the Couette gap for low centrifugal force ($\omega_i = 0.05$) as shown in Fig 4.28(a). This density peak along with loss in energy lead to a lower temperature near the centre of the Couette gap which is reflected as a temperature minimum in Fig. 4.28(b). Increasing the rotational speed to $\omega_i = 1.0$ pushes the density-peak towards the outer-wall, see Fig. 4.28(c), with a corresponding temperature-minimum as seen in Fig. 4.28(d).

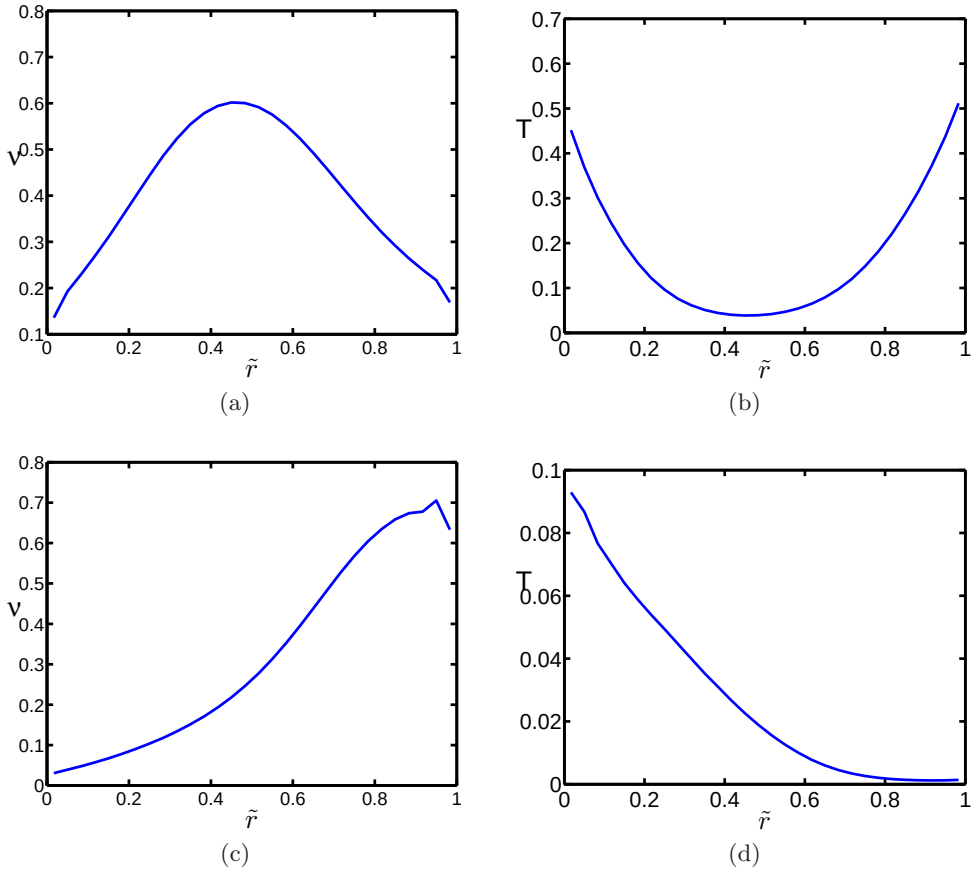

Figure 4.28: Radial variation of density for ($e_n = 0.99$) and parameter values same as in Fig. 4.16, (a) $\omega_i = 0.05$ and (c) $\omega_i = 1.0$. Radial granular temperature profiles for $e_n = 0.99$ and parameter values same as in Fig. 4.16 for (b) $\omega_i = 0.05$ and (d) $\omega_i = 1.0$.

4.2 Particle Overlap and Tolerance

An important aspect that needs to be discussed is the overlap of particles and appropriate selection of the tolerance value ($dr_{tol} = (d - \vec{r}_{12})/d$) to detect particle collisions. This analysis is similar to the what has already been done in Chapter 3(§3.4.1). The parameter values considered are same as in Fig. 4.16 for $\omega_i = 0.1$ and $e_n = 0.6$. Figure 4.29(a) shows the variation of collision time with collision number and Fig. 4.29(b) shows the probability distribution of collision time.

The value of spatial tolerance has been chosen as $dr_{tol} = 10^{-12}$ to avoid overlapping of particles. The value of temporal tolerance ($dt_{tol} = dr_{tol}/d_w\omega_i$) calculated is 10^{-14}. This choice of the temporal tolerance is appropriate as it falls below the most probable collision time ($tcol_{mp}$) shown in Fig. 4.29(a). The range of $tcol_{mp}$ is $10^{-8} - 200$ and note that the collision time is normalized by the standard deviation σ_{col} which has a value of 2.3×10^{-3} in order to get the normalised distribution. Therefore, the true range of the most probable collision time is $10^{-11} - 0.1$. This also confirms that the value of dt_{tol} is well below the lower bound of the most probable collision time (10^{-11}).

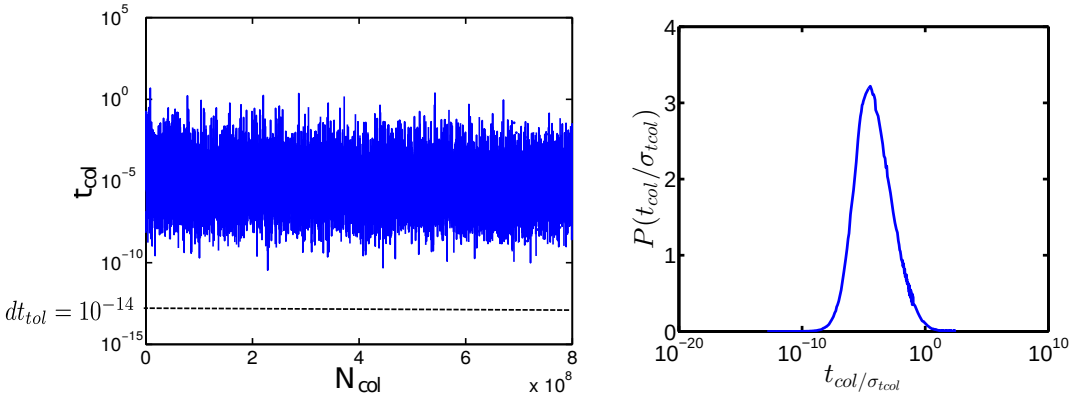

(a) (b)

Figure 4.29: (a) Variation of collision time with number of coliisions and (b) Probability distribution of collision times for parameters as in Fig. 4.16 using variable grid size. Time is scaled with $1/(\omega_i)$.

Figure 4.30(a) shows the effect of overlapping of particles on density profiles for different values of tolerance. A clear distinction can be seen between the density profiles with and without tolerance. The snapshots for two cases are shown in Fig. 4.30(b, c).

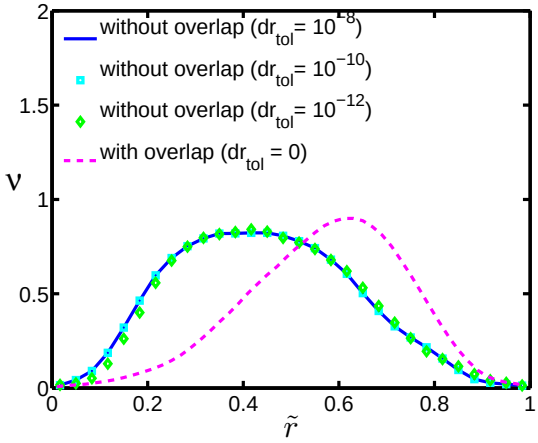

(a)

(b) t = 972.53 (c) t = 62.86

Figure 4.30: (*a*) Effect of overlapping of particles on the density profiles. Typical snapshots for parameter values as in Fig. 4.16 for $\omega_i = 0.1$, $\nu_{av} = 0.4$, $d_w = 75$ and $e_n = 0.6$, (*b*) with overlap and (*c*) without overlap.

4.3 Summary and Discussion

In this chapter, the effects of varying different parameters for 2D granular Taylor-Couette flow was discussed with the roles of rarefaction, inertia and dissipation being the driving forces. The inner cylinder rotation leads to the formation of structures which show different behaviour with varying ν_{av} and ω_i. Rarefaction was observed to domainate the dynamics for low density systems ($\nu_{av} = 0.05, 0.1$) in the large gap limit. This is mainly due to large Knudsen effects, whereas at high densities ($\nu_{av} = 0.4$) dissipation appears to take control of the dynamics. Both effects play their respective roles till the centrifugal force starts to push the particles towards the outer wall and the density maximum (of azimuthal-averaged density) starts to move towards the outer wall with an increase in ω_i. Another important observation was the occurence of solid-gas co-existence for a highly dissipative ($e_n = 0.6$) system. The gaseous region is mainly confined near the walls surrounding a massive dense structure around the centre of the annulus.

For an incompressible fluid, the Rayleigh criterion for stable flow (Chandrasekhar 1960; Dubrulle *et al.* 2005)

$$\frac{d}{dr}(l(\tilde{r})) > 0, \tag{4.5}$$

suggest that the specific angular momentum ($l(\tilde{r})$) must increase radially. For the case with radial granular temperature gradient, the Rayleigh criterion for stability is modified into (Chen & Kuo 1990):

$$\frac{\omega_i}{\tilde{r}}\frac{d}{d\tilde{r}}(l(\tilde{r})) - \beta\tilde{r}\omega_i^2\frac{dT}{d\tilde{r}} > 0 \tag{4.6}$$

where β is the thermal expansion coefficient. It must be noted that both Eqns.(4.5) & (4.6) are valid for an incompressible fluid in the inviscid limit. For the present case of compressible TCF with (i) rarefaction ($Kn > 0$), (ii) temperature gradient and (iii) density gradient, the original Rayleigh criterion is likely to be further modified. Moreover, it is known that rarefaction ($Kn \sim O(1)$) inhibits well-known fluid instabilities. The Rayleigh criterion is shown in a graphical representation in Fig. 4.31. The linear line (dashed line) $\frac{\omega_i}{\omega_o} = \left(\frac{R_o}{R_i}\right)^2$ represents Rayleigh criterion

for inviscid and incompressible fluid and the non-monotonic variation (solid line) represents the neutral stability curve for viscous incompressible fluid given by Taylor (1923).

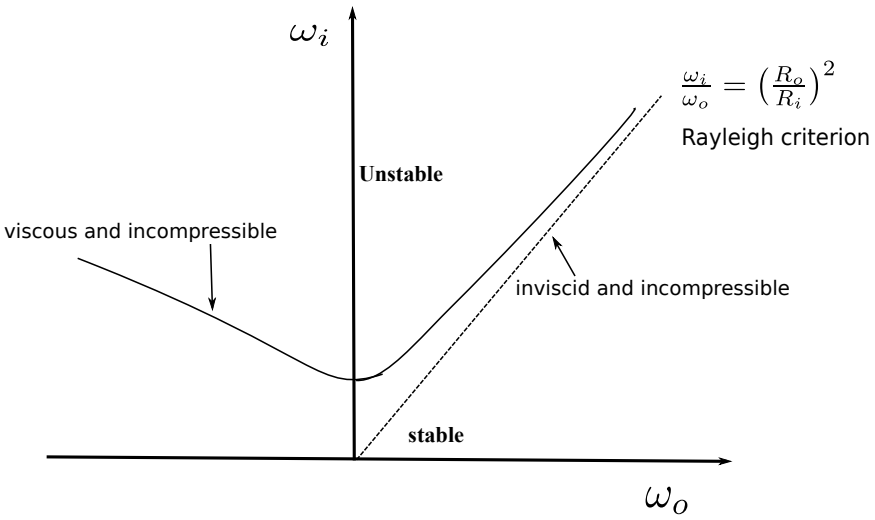

Figure 4.31: Pictorial representation of Rayleigh stability criterion taken from Taylor (1923).

The angular momentum profiles for granular TCF (Fig. 4.7, 4.13 & 4.26) does not follow Rayleigh criterion and additional theoretical anaylsis is necessary to accomodate compressibility, density and temperature effects into the hydrodynamic equations to make any comment on the stability of the granular TCF based on the profiles of angular momentum.

In the next chapter, the formation of vortices in a 3D Taylor-Couette system is analysed with the main focus being the effects of end-walls and different boundary conditions on the transient dynamics uof such vortical patterns over a range of normal restitution coefficient and mean density. The effect of inelastic dissipation on the formation of Taylor vortices will be the highlight of the next chapter.

Chapter 5

Taylor-Couette Flow in Three-dimensions

Ample work has been done so far experimentally, analytically and numerically to study various aspects of Taylor-Couette flow for fluids and the existing literature have already been highlighted in Chapter 3. There have been very few experimental studies for granular flows in Taylor-Couette setup (Conway *et al.* 2004; Mehandia *et al.* 2012; Peters *et al.* 2016; Tardos *et al.* 1998), but has showed a lot of potential to challenge the existing theories on both particle and fluid flows. The experimental works on granular Taylor-Couette flows has gathered attention after the work by Conway *et al.* (2004) in a fluidised bed. Evolution of axisymmetric structures and patterns were observed with increase in shear rate. The system evolves from a single band to four bands, and finally to seven bands over a period of time and several other features common to Taylor vortex instability were found. A rheometric anomaly of dense granular TC-system was discovered by Mehandia *et al.* (2012) where they found that the stress profile varies differently from that of fluids. They argued that the anomalous stress profile is due to an anisotropic fabric caused by the combined action of gravity and shear. More recently, Krishnaraj & Nott (2016) seem to have resolved the above stress anomaly via soft-particle simulations. Murdoch *et al.* (2013) discusses the effect of gravity and secondary flows which occurs in the form of radial flow towards the inner cylinder; this radial flow was absent for zero gravity system. The absence of radial flow is important in the present study since only the effect of centrifugal forces can be studied in the absence of gravity. It has been shown [Murdoch *et al.* (2013)] that friction plays a deciding role in whether secondary flows occur in TC flow geometry. They concluded that the gravity acts as an amplifier for frictional effects.

Cheng *et al.* (2006) investigated the evolution of granular shear flow as a function of height in a split-bottom Couette cell (van Hecke & van de Meent 2004). They observed that radial and axial shear profiles are qualitatively different. While the radial extent is wide and increases with height, the axial width remains narrow and fixed like a traditional shear band. Tardos *et al.* (1998) concluded that the normal force compressing the powder is not constant but varies significantly with layer depth. Specifically, for a variety of fine powders with different physical properties such as bulk density and internal friction angle, normal and shear stress increase linearly with depth in a shearing column. It was also found that for the fine powders used in their experiment, the torque varied linearly with the upward flowing gas velocity to the point of minimum fluidization where the torque becomes negligibly small and torques were practically independent on the rotation rate, i.e., shear rate. Bocquet *et al.* (2001) analyzed the main features of granular shear flow through experimental measurements in a Couette geometry and a comparison to a locally Newtonian, continuum model of granular flow. The model was based on earlier hydrodynamic models, adjusted to take into account the experimentally observed

coupling between fluctuations in particle motion and mean-flow properties. Experimentally, the local velocity fluctuations are found to decrease more slowly with distance from the shear surface than the velocity. The flow was confined to a small shear band, fluctuations decay approximately exponentially away from the sheared wall, and the shear stress was approximately independent of the shear velocity.

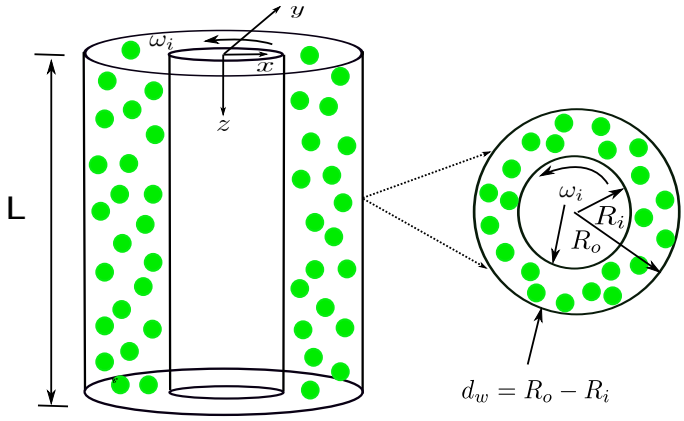

Figure 5.1: Simulation geometry (TC) with granular particles in the annular region

Figure 5.1 shows the Taylor-Couette setup in three dimensions with granular particles in between the annular region. The absence of gravity inhibits the formation of secondary structures in this flow, such as those found by Tardos *et al.* (1998), Cheng *et al.* (2006), Mehandia *et al.* (2012) and Murdoch *et al.* (2013). Hence the effects of walls and other parameters in the study will help to elucidate the onset of pattern formation and other complicated structures observed in this TC-geometry. In contrast to previous chapter, this chapter deals with the consequences of adding an additional direction (z) to the flow. Two types of boundary conditions along the axial (z) direction are used: (i) reflecting and (ii) periodic boundary conditions at end-walls. The presence of stationary end-walls with reflecting boundary conditions in the axial direction avoids creating a secondary source of shear that would distort the vortices, which is usually unavoidable in experiments [Hirshfeld & Rapaport (1998)]. The periodic boundary condition is an essential tool to avoid any interaction of the flow with the end walls; the setup can be assumed to be infinitely long in the z-direction to suppress any end-wall effect. Both types of boundary conditions have been used to understand the dynamics of Taylor vortices in a recent paper which focuses on the development of wavy-vortices using molecular dynamics simulations [Trevelyan & Zaki (2016)].

This is the first study to understand pattern formation in Taylor-Couette setup using hard spherical particles, and its dependence on the end walls. The difficulty to simulate high density system using hard sphere simulations has affected the present study, but an attempt has been made to explain many critical phenomena observed. The end walls appear to have a significant effect for low L/d_w where L is the length of the cylinder and d_w is the gap-width ($R_o - R_i$), in the nucleation of primary and secondary structures. The effect of restituion coefficient on Taylor-vortices is discussed in the later part of this chapter.

5.1 Taylor-Couette Flow of Elastic Particles: Onset of Taylor Vortices

A system of smooth hard spheres is simulated in an annular geometry with the inner wall rotating at a certain rotation rate, a necesarry condition for the flow to be unstable, is considered Taylor (1923). The transfer of momentum takes place due to streaming and collision in the absence of gravity. The system attains a statistical steady state when the average kinetic energy reaches a constant value or fluctuates about a mean value, see Fig. 5.2. The gain in energy due to inertial centrifugal force and loss due to the presence of thermal- walls (which act as a source or a sink) reaches a balance after some time and the system attains a statistical steady state. Figure 5.2 shows the temporal variation of the energy, $E(t) = \sum_{i=1}^{N}(c_{xi}^2 + c_{yi}^2 + c_{zi}^2)/2N$, per particle for $e_n = 1$.

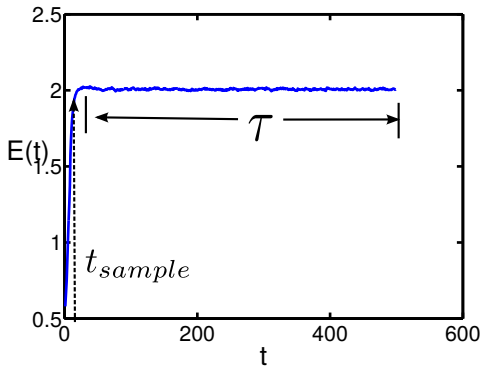

(a)

Figure 5.2: Evolution of total kinetic energy versus time when the system reaches a statistical steady state for reflecting-type boundary condition. Parameter values are $d_w = 25$, $N = 47295$ (one quadrant considered), $n_{binr} = 15$, $n_{binz} = 80$, $R_o = 75$, $L/d_w = 4$, $\tilde{r} = (r - R_i)/d_w$, $\nu_{av} = 0.2$, $e_n = 1.0$ and $\omega_i = 0.1$

The system remains homogeneous in the azimuthal direction but becomes inhomogeneous in both axial and radial direction (Hirshfeld & Rapaport 1998) due to the formation of vortices. This is true if Taylor number is less than the critical Taylor number for the onset of wavy vortices. The homogeneity along the azimuthal direction helps in reducing the computational time by concentrating only in one quadrant of the geometry since the number of particles required for the simulations reduces to 1/4 of the actual number. Special periodic boundaries are used to account for the effect of particles in the absent quadrants as discussed by Hirshfeld & Rapaport (1998). Whenever a particle exits out of the slice/quadrant, it is returned via the perpendicular boundary with its position and velocity components suitably interchanged and sign-adjusted. All the characteristic quantites have been averaged over a large number of snapshots in θ direction.

5.1.1 Periodic axial boundary conditions

The implementation of periodic boundary conditions is trivial and has been explained in many classical texts on MD simulations and other numerical techniques. If a particle moves out of the

system, an image of the same particle enters into the system from the opposite end at the same value of (r, θ). The new z position will be

$$z_i = (z_i + 2L)\%L,$$

where % represents the mathematical notation for modulo or the remainder, as shown in Fig. 5.3. A particle with axial velocity c_{z1} leaves the system at $z = 0$ and re-enters into the system at $z = L$ with same axial velocity; its radial and azimuthal velocities remain same too. The same procedure is applied to all particles like the particle with axial velocity c_{z2} leaving at $z = L$ and coming back at $z = 0$.

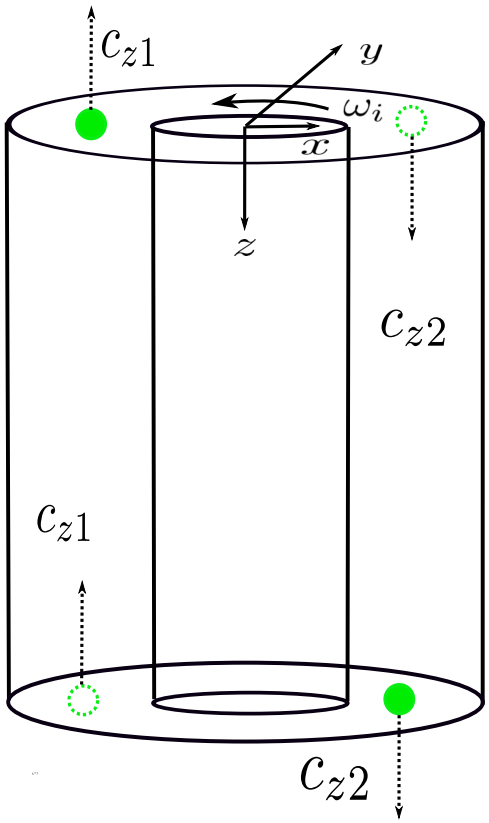

Figure 5.3: Periodic boundary conditions, replica or image particle is represented by *dotted green* and actual particle by *solid green*

Figure 5.4 shows the temporal evolution of Taylor vortices with parameters $d_w = 25$, $R_o = 50$, $L/d_w = 2$, $\nu_{av} = 0.2$, $e_n = 1.0$ and $\omega_i = 0.1$. The averaging of the hydrodynamic profiles are carried out over N $\times$ 5000 collisions after the system attains a steady state at around $N \times 3000$ collisions and snapshots are taken after every $N \times 20$ collisions starting from $N \times 3000$ collisions. The vortices shown in Fig. 5.4 is obtained by averaging the velocity snapshots temporally over N $\times$ 7500 collisions with snapshot taken after every $N \times 20$ collisisons to get the velocity vector plot of vortices. The code ends at $N \times 8000$ collisions. Note that the time at which the first snapshot (denoted by t_{sample}) is taken to calculate velocity vectors is $N \times 500$ whereas time for other hydrodynamic properties(density, granular temperature, velocities) is $N \times 3000$, though for both cases the system has reached a steady state.

For calculating velocity vectors the reference time has been shifted to a different scale and is represented in terms of $\tau = t - t_{sample}$ where t_{sample} represents the time at which the code starts calculating the averages (after N $\times$500 collisions). The velocity vectors at a particular time τ is calculated by averaging velocities over all the snapshots from 0 - τ in the modified time scale which is represented by:

$$u(\tilde{r}, z, \tau) = \frac{1}{2\pi\tau} \int_0^{2\pi} \int_0^{\tau} u(\tilde{r}, \theta, z, t) dt d\theta, \tag{5.1}$$

where t denotes the actual time of the simulation, $\tau = t - t_{sample}$ represents the modified time scale and $u(\tilde{r}, z, \tau)$ represents the azimuthally averaged velocity. Note that this definition does not give the instantaneous picture of the vortices but the time taken to have a fully developed vortex as given in Fig. 5.4. The entire setup is divided into an array of bins of size $w_r = (R_o - R_i)/n_{binr}$ in the radial direction and $w_z = L/n_{binz}$ in the axial direction, where w_r and w_z are widths of the bins in the radial and axial direction, respectively; n_{binr} and n_{binz} are number of bins in the radial and axial direction respectively. The details of bin size will be mentioned from here after for averaging details. Note that only one quadrant is considered for all the results with elastic collisions in order to reduce the computation cost.

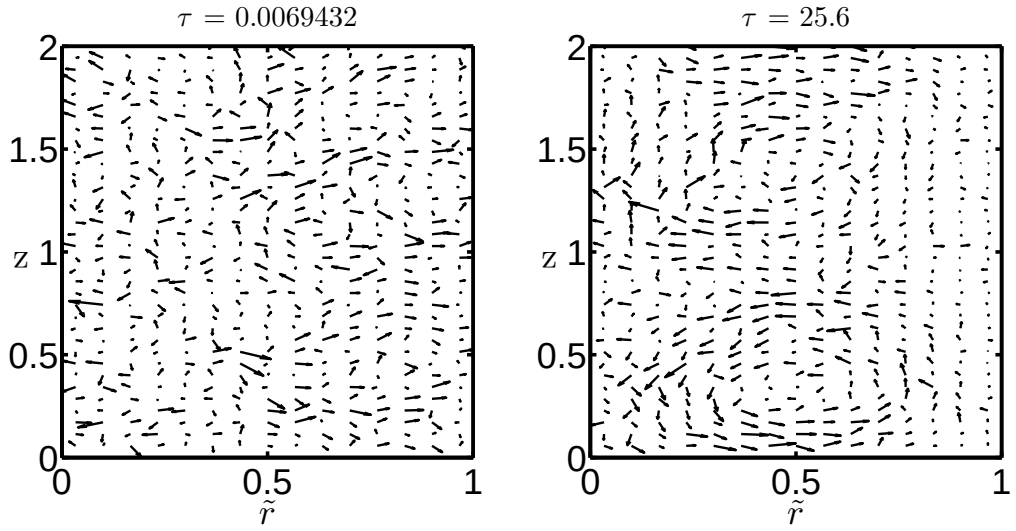

(a) (b)

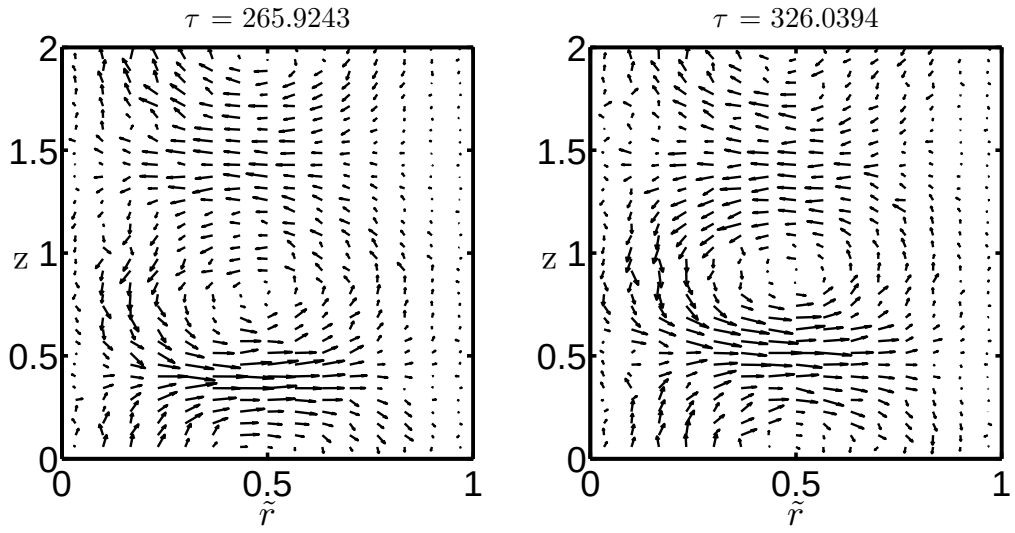

(c) (d)

Figure 5.4: Snapshots showing different stages of vortex formation averaged using Eq. 5.1 for periodic boundary conditions in the axial direction (*two vortices*). Parameter values are $d_w = 25$, $N = 47295$ (one quadrant considered), $n_{binr} = 15$, $n_{binz} = 35$, $R_o = 75$, $L/d_w = 2$, $\tilde{r} = (r - R_i)/d_w$, $\nu_{av} = 0.2$, $e_n = 1.0$ and $\omega_i = 0.1$

Figure 5.5 shows the final fully developed vortices for different aspect ratio ($\frac{L}{d_w} = 2, 4, 5$) at the end of each simulation averaged over multiple number of snapshots. Even number of vortices are formed for all the cases simulated in this study, with the number of vortex pairs increasing with increase in length of the system.

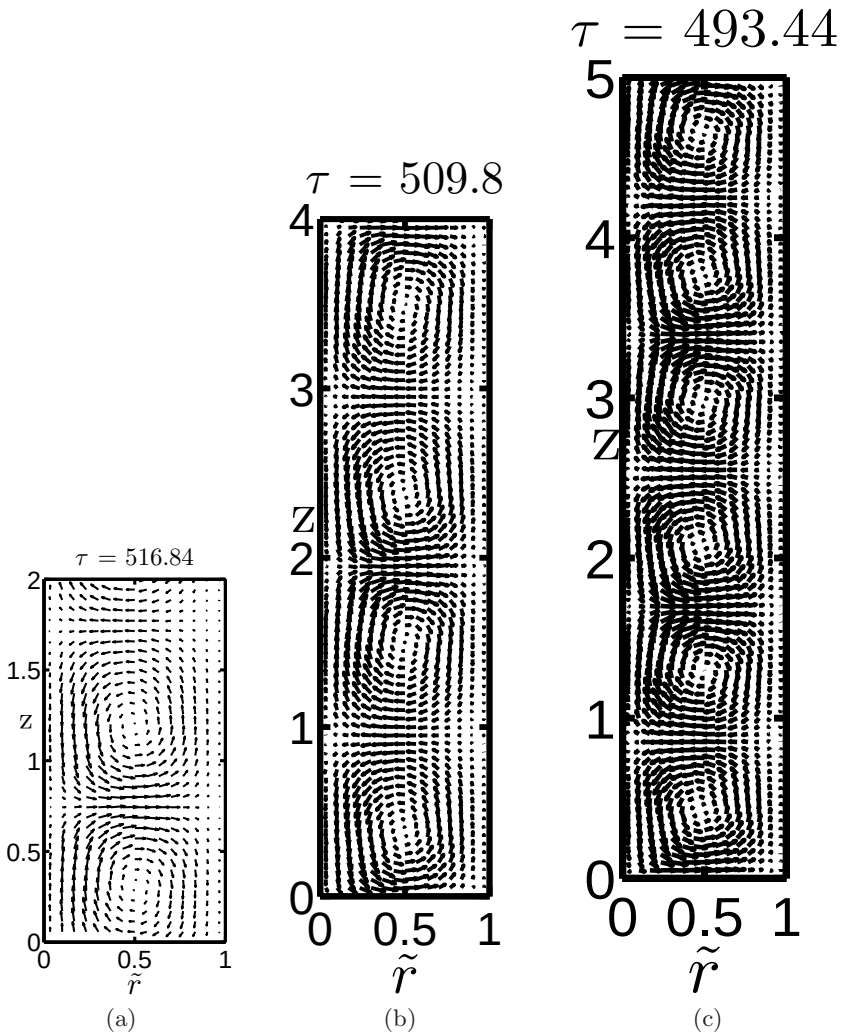

Figure 5.5: Fully developed vortices for periodic boundary conditions in the axial direction for (*a*) $L/d_w = 2$ (two vortices), (*b*) $L/d_w = 4$ (four vortices) and (*c*) $L/d_w = 5$ (six vortices). Parameter values are $d_w = 25$, $R_o = 75$, $\tilde{r} = (r - R_i)/d_w$, $\nu_{av} = 0.2$, $e_n = 1.0$, $\omega_i = 0.1$, $n_{binr} = 15$ for (*a*) $n_{binz} = 35$, (*b*) $n_{binz} = 80$ and (*c*) $n_{binz} = 100$

5.1.2 Reflecting axial boundary conditions

The reflecting-type boundary conditions are implemented such that when the particles hit the end walls, they are reflected back into the system with no loss in energy and with the same magnitude of velocity. The velocity components after a collision changes as given by eqns. (5.2, 5.3, 5.4), where the components with prime represents velocity after collision.

$$\vec{c_x}' = \vec{c_x} \tag{5.2}$$

$$\vec{c_y}' = \vec{c_y} \tag{5.3}$$

$$\vec{c_z}' = -\vec{c_z} \tag{5.4}$$

Figure 5.6 shows a schematic representation of the reflecting boundary at the end walls with particles being pushed back into the system. As mentioned before, this boundary condition is

more realistic compared to periodic boundaries, and can be realized in experiments.

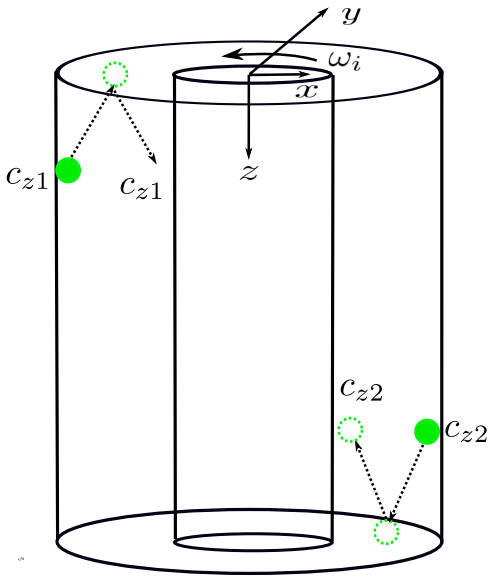

Figure 5.6: Reflecting boundary conditions, replica or image particle *dotted green* and actual particle *solid green*

Figure 5.7 shows fully developed vortices formed with the inner cylinder rotating at $\omega_i = 0.1$. Equal number of vortices is formed for both types of boundary conditions with the same set of parameter values as given in Fig. 5.5. The increase in the length of the cylinder to 125 adds another pair of vortex to the flow as shown in Fig. 5.7(c), with negligible change in the dynamics of their formation. This is the longest cylinder considered in the present study and the effect of the inelasticity present in the system is discussed with $L/d_w = 4$ in section 5.2 and the rest of the parameters are kept same.

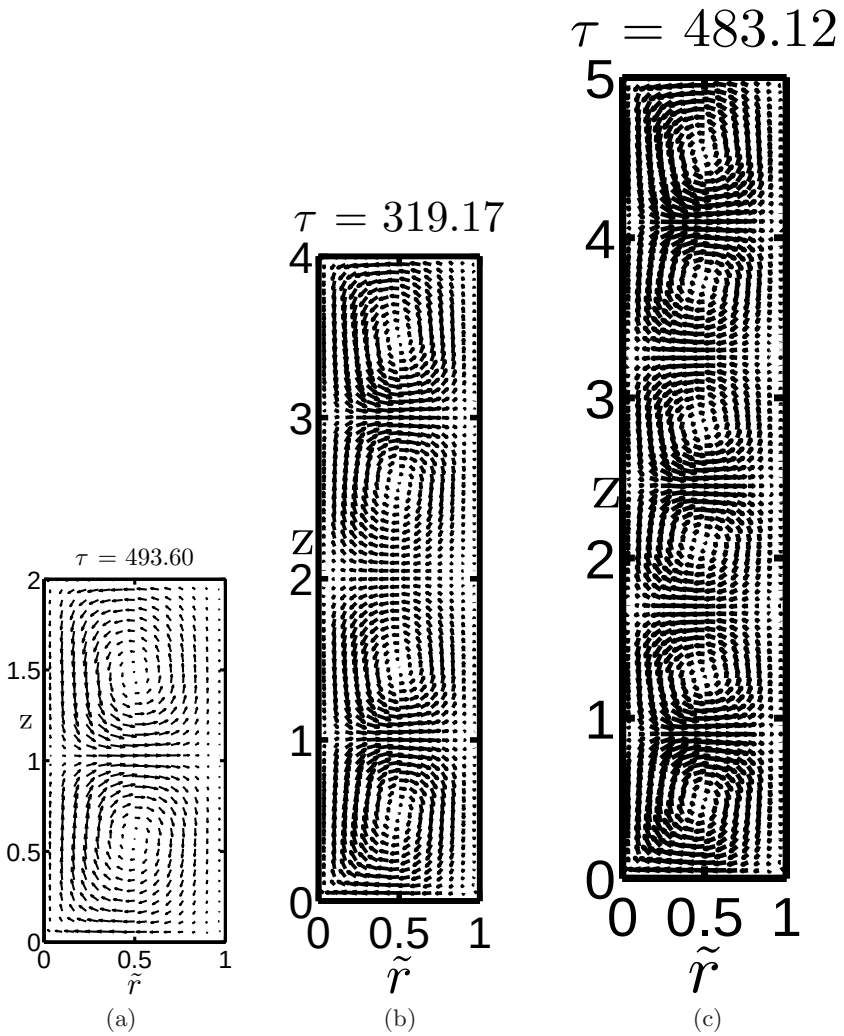

Figure 5.7: Fully developed vortices for reflecting-type boundary conditions in the axial direction for (a) $L/d_w = 2$ (two vortices), (b) $L/d_w = 4$ (four vortices) and (c) $L/d_w = 5$ (six vortices). Parameter values are $d_w = 25$, $R_o = 75$, $\tilde{r} = (r - R_i)/d_w$, $\nu_{av} = 0.2$, $e_n = 1.0$, $\omega_i = 0.1$, $n_{binr} = 15$ for (a) $n_{binz} = 35$, (b) $n_{binz} = 80$ and (c) $n_{binz} = 100$

Figure 5.8 shows the hydrodynamic profiles for the set of parameters of Fig. 5.7(a). The density variation being linear in radial and non-monotonic in axial, as shown in Fig. 5.8(a) and (b) respectively. With density varying in both radial and axial direction, compressibilty effects are important and therefore, cannot be neglected. The positive peak of radial velocity at the centre can also be seen from Fig. 5.7(a) where all the velocity vectors are pointing towards the outer direction. The axial velocity in Fig. 5.8(c) also shows a periodic variation, approaching zero slip velocity at the walls. The azimuthal velocity in Fig. 5.8(e) decreases with $\tilde{r}$ and approaches the slip velocity at the outer wall. The radial velocity in Fig. 5.8(h) is symmetric about the cylinder's centreline and shows a maxima at the centre. Temperature follows a completely opposite behavior to that of density as shown in Fig. 5.8(c, d) whereas axial velocity undergoes a transition from particles being moving in the downward direction to moving in the upward direction at $\tilde{r} = 0.5$ as shown in Fig. 5.8(i).

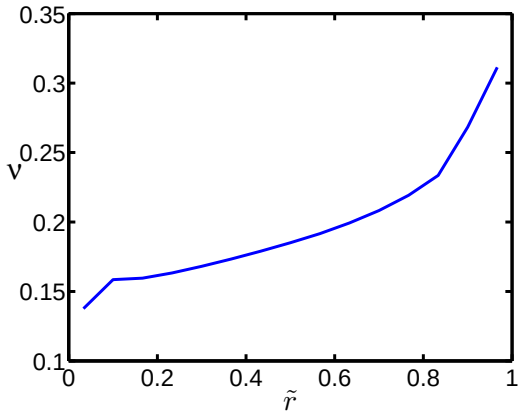
0.35
0.3
0.25
0.2
0.15
0.1
ν
0
0.2
0.4
0.6
0.8
1
$\tilde{r}$

(a)

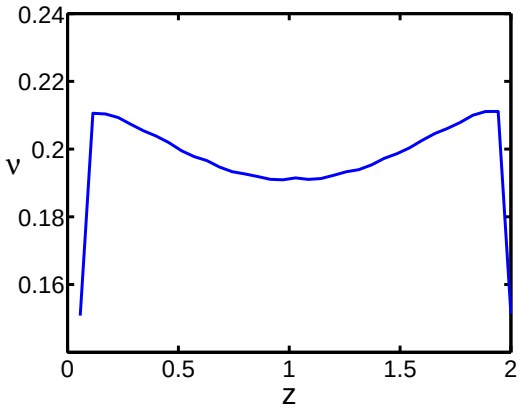
0.24
0.22
0.2
0.18
0.16
ν
0
0.5
1
1.5
2
z

(b)

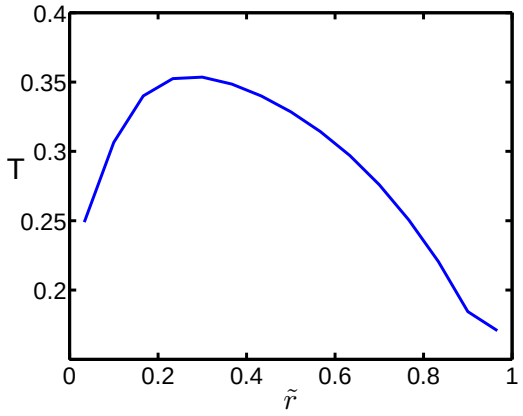
0.4
0.35
0.3
0.25
0.2
T
0
0.2
0.4
0.6
0.8
1
$\tilde{r}$

(c)

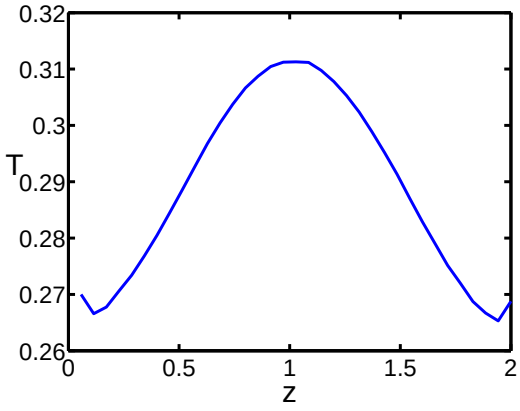
0.32
0.31
0.3
0.29
0.28
0.27
0.26
T
0
0.5
1
1.5
2
z

(d)

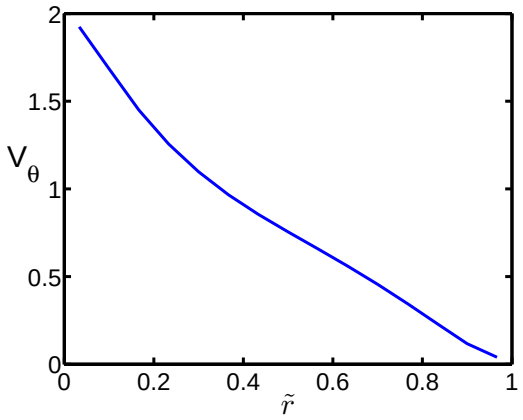
2
1.5
1
0.5
0
V_θ
0
0.2
0.4
0.6
0.8
1
$\tilde{r}$

(e)

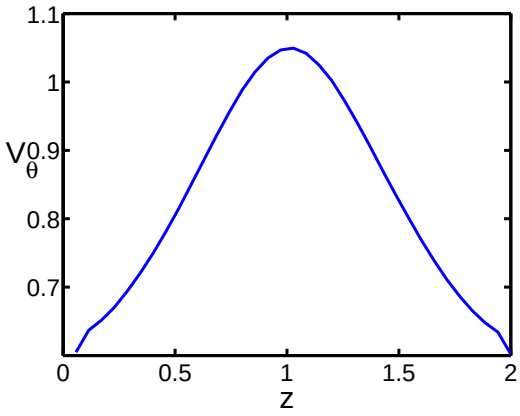
1.1
1
0.9
0.8
0.7
V_θ
0
0.5
1
1.5
2
z

(f)

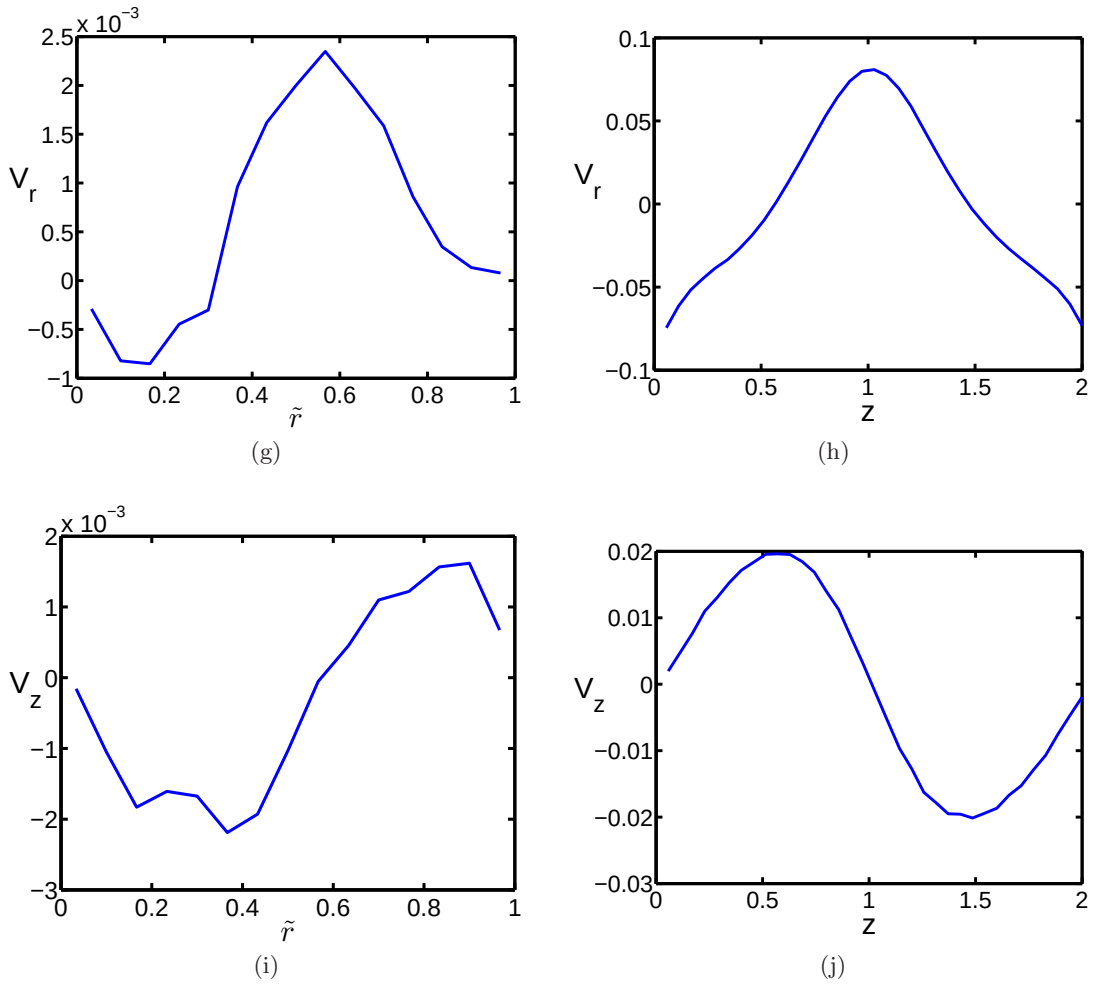

Figure 5.8: Hydrodynamic profiles along the radial (a, c, e, g, i) and axial direction (b, d, f, h, j). Parameter values are same as in Fig. 5.7(a)

Figure 5.9 shows the mean profiles for the same set of paramters as in Fig. 5.7(b). The negative radial velocity at the centre in Fig. 5.9(h) can be seen from fig 5.7(b) with the flow being in the inward direction. The radial density profile does not show any change in trend with the change in the length of the cylinders, compared to that in Fig. 5.8(a). Also the temperature profile in Fig. 5.9(d) is opposite in trend to the density profile, though both are periodic in nature. The radial velocity profile in the radial direction in Fig. 5.9(g) is mainly dominated by the particles moving towards the outer wall with a region of particles near the innner wall flowing inwards. The opposite is observed for axial velocity in Fig. 5.9(i) where the majority of the particles along the radial direction are flowing in the downward direction. There is not much difference in the hydrodynamic profiles with increase in length qualitatively. The periodic nature exists in the axial direction whereas the radial profiles remain the same.

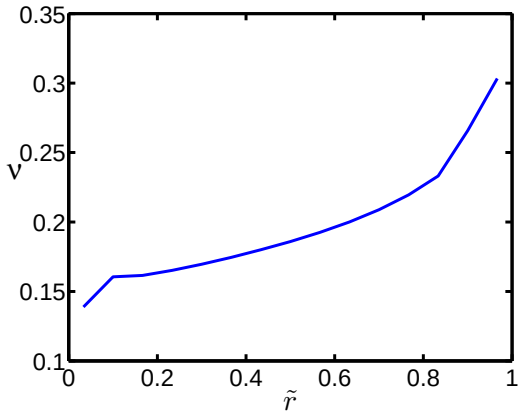
0.35
0.3
0.25
0.2
0.15
0.1
ν
0
0.2
0.4
0.6
0.8
1
$\tilde{r}$

(a)

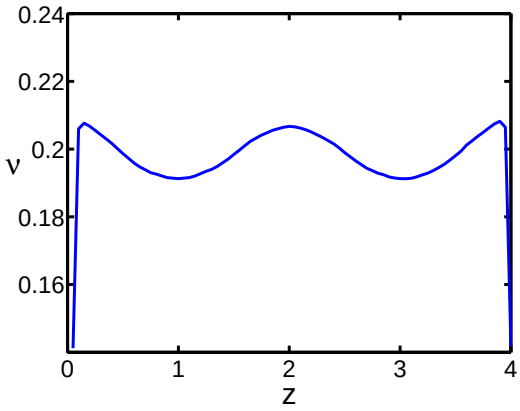
0.24
0.22
0.2
0.18
0.16
ν
0
1
2
3
4
z

(b)

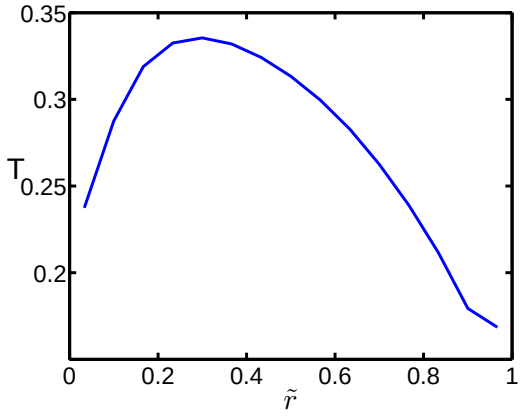
0.35
0.3
0.25
0.2
T
0
0.2
0.4
0.6
0.8
1
$\tilde{r}$

(c)

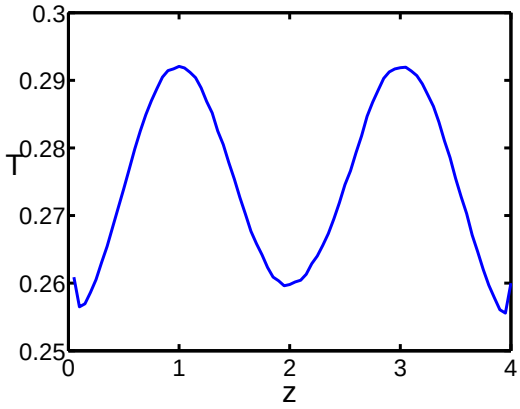
0.3
0.29
0.28
0.27
0.26
0.25
T
0
1
2
3
4
z

(d)

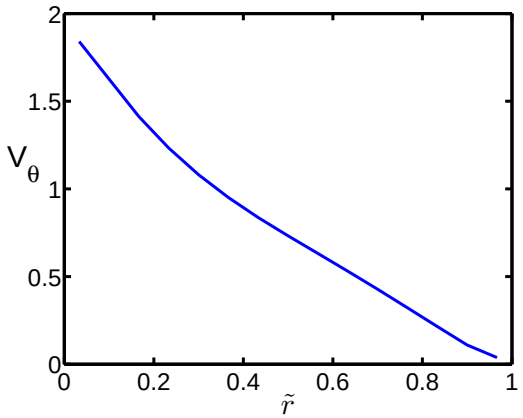
2
1.5
1
0.5
0
V_θ
0
0.2
0.4
0.6
0.8
1
$\tilde{r}$

(e)

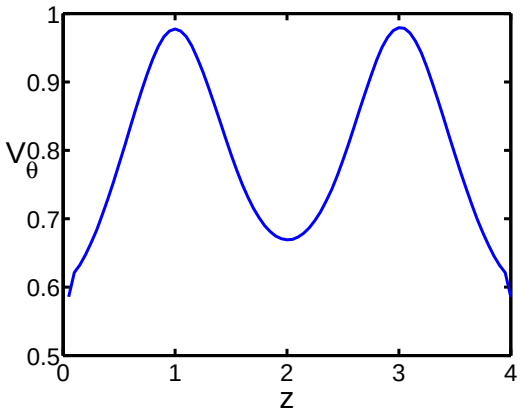
1
0.9
0.8
0.7
0.6
0.5
V_θ
0
1
2
3
4
z

(f)

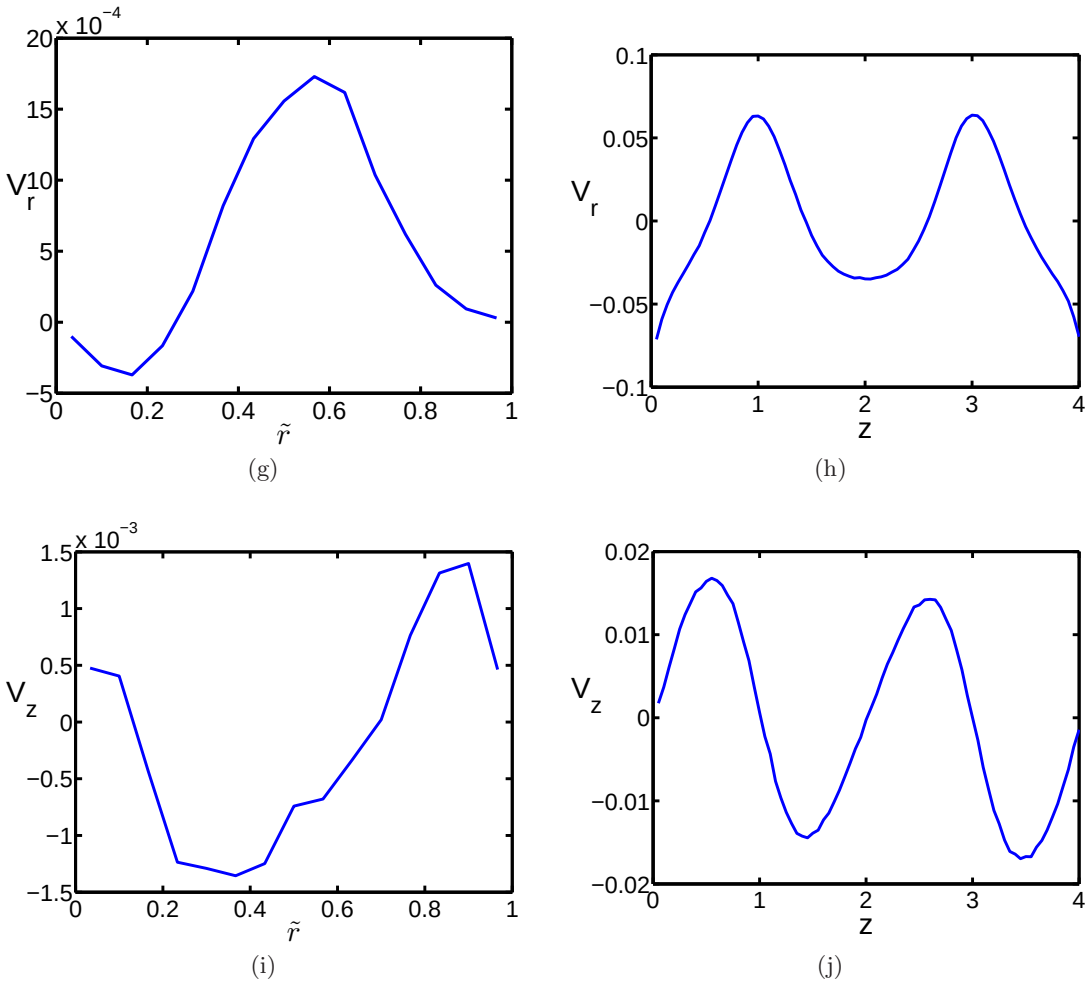

Figure 5.9: Hydrodynamic profiles along the radial (a, c, e, g, i) and axial direction (b, d, f, h, j). Parameter values are same as in Fig. 5.7(b)

The contour plots of density and granular temperature in Fig. 5.10 will give a better picture of the localised bands formed in the flow. The plots shows the final fully developed profile averaged over $N \times 5000$ collisions and the snapshots are taken after every $N \times 20$ collisions. The density appears to be higher near the outer cylinder and vary sinusoidally in z near the radial centre. The behaviour of density profile follows a different trend near the outer and inner wall with minimal variation near the former and two round shaped peaks near the latter. A completely opposite behaviour is observed for temperature with particles having more energy near the inner cylinder and lesser energy near the outer wall.

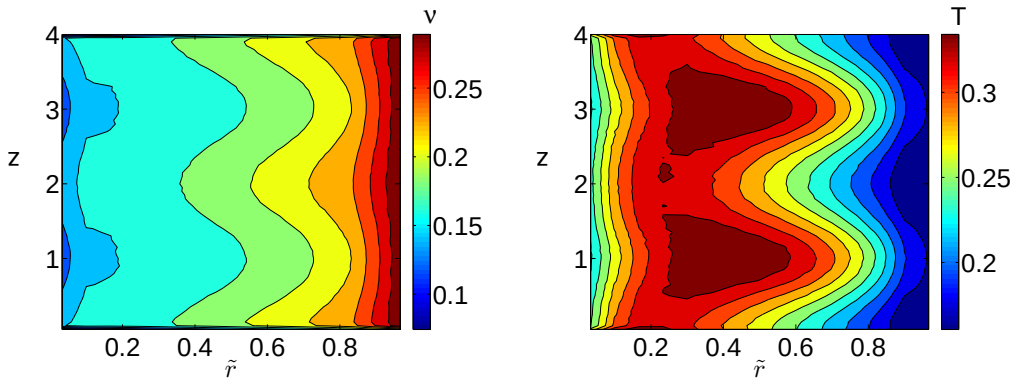

(a) (b)

Figure 5.10: Contour plots of (a) density (b) granular temperature in z and $\tilde{r}$ direction. Parameter values are same as in Fig. 5.7(b)

Figure 5.11 shows the radial and axial variations of angular momentum for elastic particles which are calculated using the following equations,

$$\omega(r) = \omega(r,\theta,z)\big\rangle_{\theta,z} = \big\langle V_\theta(r,\theta,z)\big\rangle_{\theta,z}/r, \tag{5.5}$$

$$\omega(z) = \omega(r,\theta,z)\big\rangle_{\theta,r} = \big\langle V_\theta(r,\theta,z)\big\rangle_{\theta,r}/r, \tag{5.6}$$

$$l(r) = \big\langle l(r,\theta,z)\big\rangle_{\theta,z} = \big\langle \nu(r,\theta,z)V_\theta(r,\theta,z)\big\rangle_{\theta,z} r, \tag{5.7}$$

$$l(z) = \big\langle l(r,\theta,z)\big\rangle_{\theta,r} = \big\langle \nu(r,\theta,z)V_\theta(r,\theta,z)\big\rangle_{\theta,r} r \tag{5.8}$$

where $V_\theta(r,\theta,z)$ is the final temporally averaged azimuthal velocity, $\nu(r,\theta,z)$ is the local density and r is the radial distance from the centre. The angular momentum and angular velocity are non-dimensionalised by $(d_w^2\omega_i)$ and ω_i respectively. The angular momentum in Fig. 5.11(a) decreases linearly with radius, as the particles near the inner wall have a higher angular momentum compared to the particles near the outer cylinder. The variations of both angular momentum and angular velocity in Fig. 5.11(b) follows a similar trend as of azimuthal velocity.

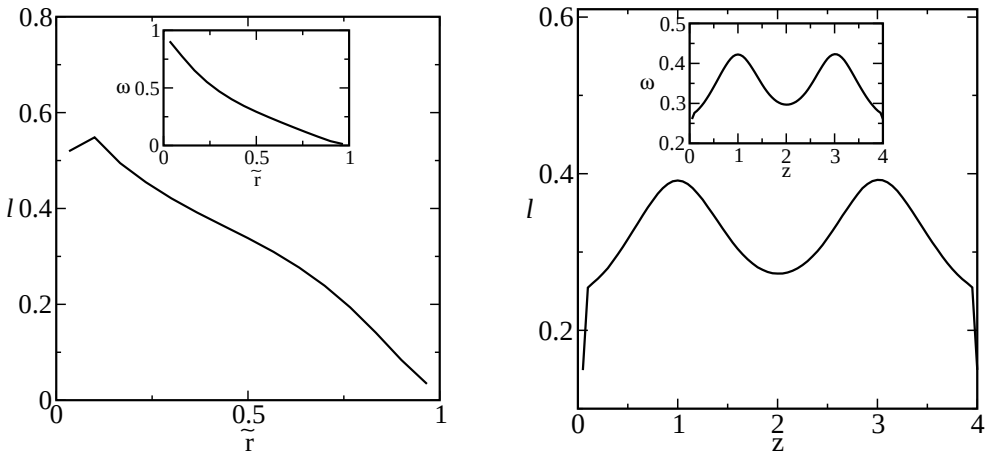

(a) (b)

Figure 5.11: Profiles of (a) radial (b) axial angular momentum along with inset showing the angular velocity. Parameter values are same as in Fig. 5.7(b)

5.2 Taylor-Couette Flow of Inelastic Particles

As the flow is not expected to be homogeneous, due to inelastic nature of the particles, the procedure of using only one quadrant is not valid and hence the entire system involving all the four quadrants is to be simulated. A mean volume fraction of $\nu_{av} = 0.2$ involves simulating about 360000 particles. Figure 5.12 shows the temporal variation of the energy, $E(t) = \sum_{i=1}^{N}(c_{xi}^2 + c_{yi}^2 + c_{zi}^2)/2N$, per particle for $e_n = 0.99$ (a) and $e_n = 0.9$ (b).

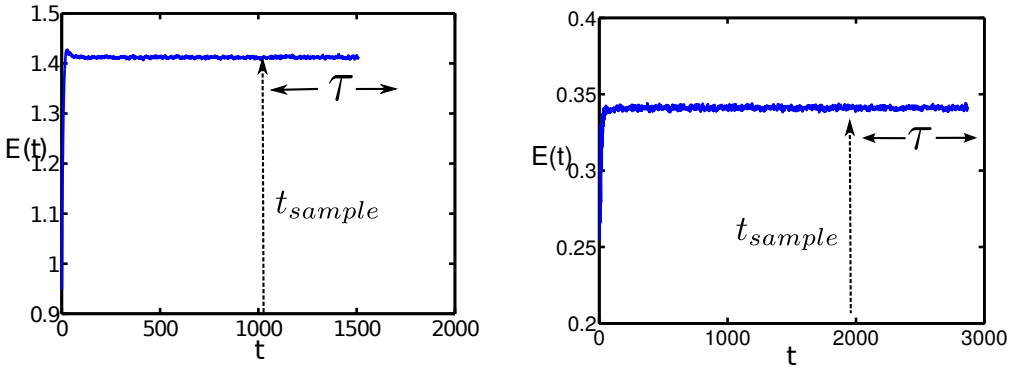

(a) (b)

Figure 5.12: Evolution of total kinetic energy versus time when the system reaches a statistical steady state for (a) $e_n = 0.99$ and (b) $e_n = 0.9$ with reflecting axial boundary conditions. Parameter values are $d_w = 25$, $N = 365748$, $n_{binr} = 15$, $n_{binz} = 80$, $R_o = 75$, $L/d_w = 4$, $\tilde{r} = (r - R_i)/d_w$, $\nu_{av} = 0.2$ and $\omega_i = 0.1$

The inelasticity in the system is defined by the coefficient of restitution (e_n), which is a measure of average kinetic energy loss $(\propto (1 - e_n^2))$ during a collision for smooth particles. The normal velocity of a particle changes after a collision, whereas its tangential component remains constant. A qualitative comparison will be made between the two cases for $L/d_w = 4$ and a set of values for the coefficient of restitution $e_n \in (0.9, 0.99)$. Note that the number of particles is four times higher in this section compared to the previous section §5.1 even though the mean volume fraction is same. The present simulations have captured the effects of inelasticity on the development of Taylor-vortices and hydrodynamic profiles. The velocity vectors are averaged in the same way as given by Eq. 5.1. Note that the snapshots are taken after every $N \times 20$ collisions and are averaged over a period of $N \times 2000$ collisions. The averaging starts at $N \times 4000$ and ends at $N \times 6000$ collisions. The time at which the first snapshot is taken for averaging is same for both velocity vectors and other hydrodynamic profiles.

5.2.1 Periodic boundary conditions

Figure 5.13 shows the final picture of fully developed vortices with same parameters used in Fig. 5.12 for $e_n = 0.99$ and $e_n = 0.9$. No discernible change can be seen for $e_n = 0.99$ when compared to its counterpart in Fig. 5.7 (see panel b). Only the magnitude of velocity vectors appear to be reduced in Fig. 5.13 which is more visible for $e_n = 0.9$ in Fig. 5.13(b).

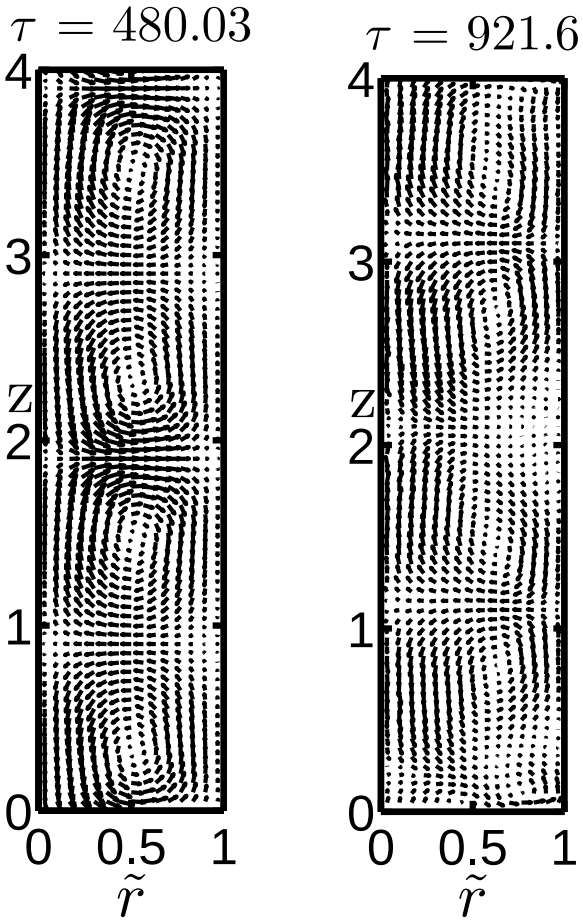

Figure 5.13: Fully developed vortices for reflecting boundary conditions in the axial direction for (a) $e_n = 0.99$ and (b) $e_n = 0.9$. Parameter values are same as in Fig. 5.12 except for periodic boundary conditions.

The pair of vortices in Fig. 5.13(b) appears to be tilted in the direction of the velocity vectors. This tilt was absent for the elastic case considered in section 5.1.

5.2.2 Reflecting boundary conditions

Figure 5.14 shows fully developed vortices for dissipative system with reflecting-type boundary conditions. No discernible difference is observed for $e_n = 0.99$ (see Fig. 5.14(a)), with different types of axial wall-boundary conditions as can be seen by comparing Fig. 5.13 with Fig. 5.14. Two pair of vortices, mirror images about the z-centreline, are formed for both cases.

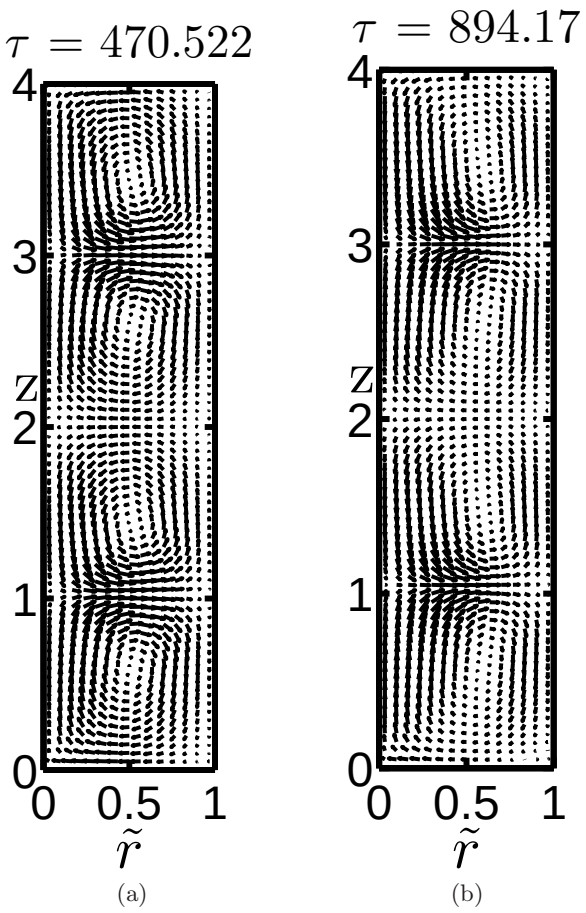

Figure 5.14: Fully developed vortices for reflecting boundary conditions in the axial direction for (a) $e_n = 0.99$ and (b) $e_n = 0.9$. Parameter values are same as in Fig. 5.12.

An interesting feature observed in Fig. 5.14(b) is the formation of two pair of weaker vortices indicating the effect of inelasticity in the system due to large number of particle-particle collisions.

Figure 5.15 shows the contour plots of density and granular temperature for different values of e_n. Clearly the temperature for $e_n = 0.9$ is lower near the outer wall as can also be seen from the Fig. 5.15(e). The temperature is lower at the centre for $e_n = 0.99$ and $e_n = 0.9$ due to large number of particle-particle collisions resulting in a loss of energy which is manifested in the form of lower temperature. The higher temperature near the inner wall is due to small number of particle-particle collisions in the rarefied region and gain in the energy from the inner wall.

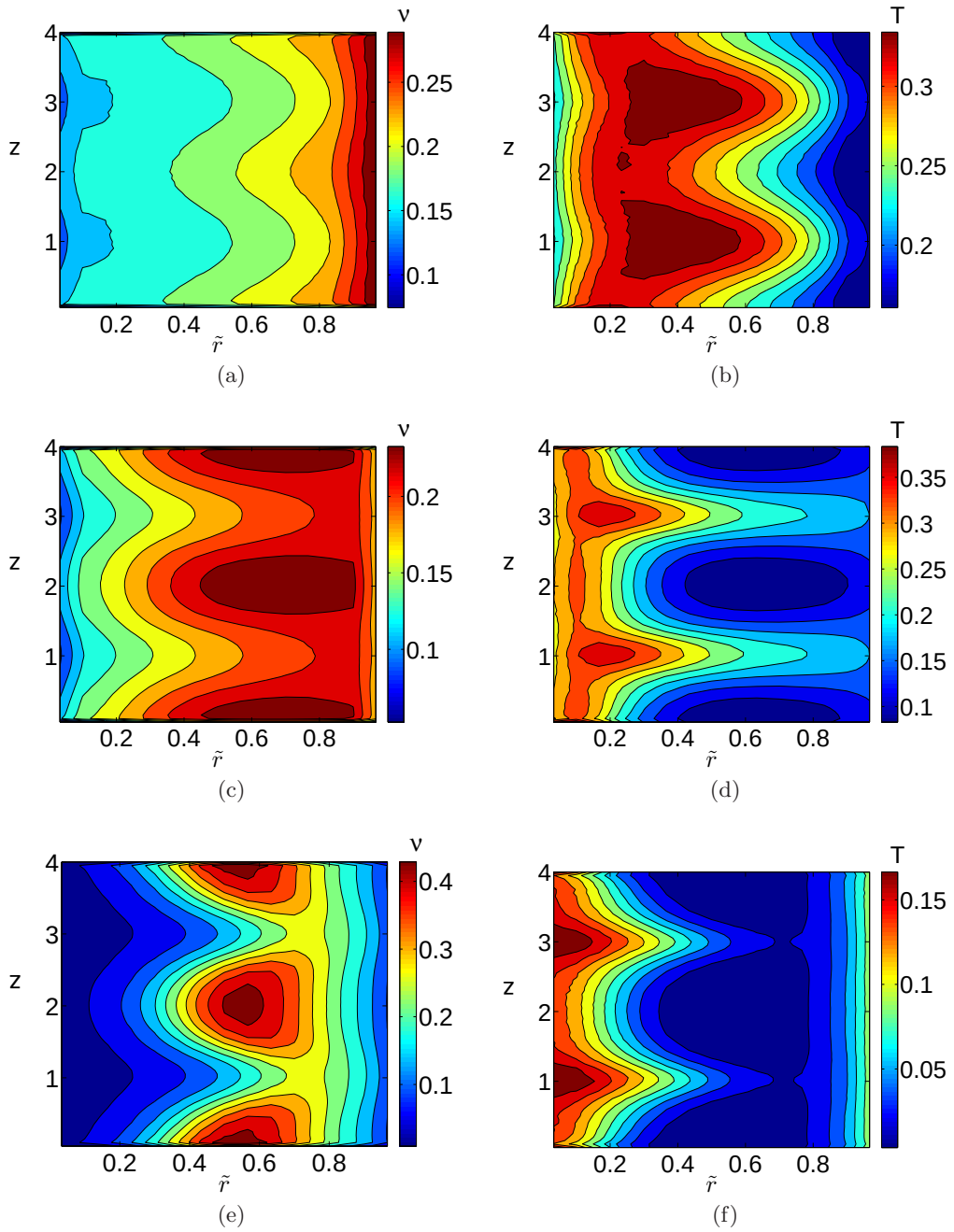

Figure 5.15: Contour plots of (a, c, e) density (b, d, f) granular temperature in z and $\tilde{r}$ direction for(a, b) $e_n = 1.0$, (c, d) $e_n = 0.99$ and (e, f) $e_n = 0.9$. Parameter values are same as in Fig. 5.14

Figures(5.16-5.25) show the effects of inelasticity on hydrodynamic profiles. For the elastic system in Fig. 5.16(a), the homogeneous distribution of the particles leads to a very low values of V_r with a net inward flow near the vicinity of the inner wall. An addition of small inelasticity in the system, Fig. 5.16(b), makes the system inhomogeneous. A comparatively larger magnitude of V_r suggests that the flow is completely in the outward direction $(+ve\ V_r)$ even in the vicinity of the walls for both $e_n = 0.99$ and $e_n = 0.9$.

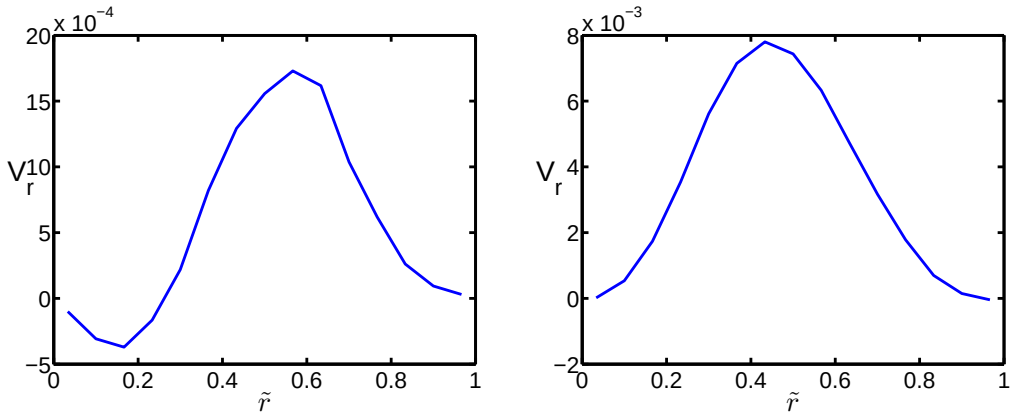

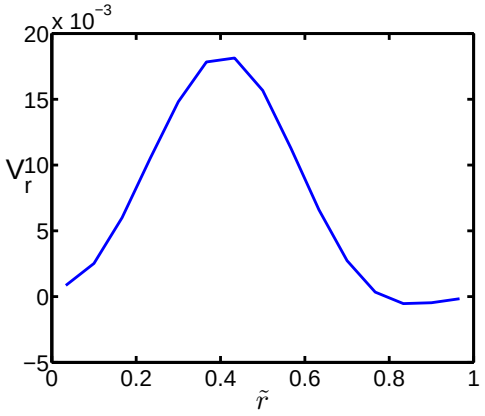

Figure 5.16: Radial variation of radial velocity (averaged in the axial and azimuthal direction): (a) $e_n = 1.0$, (b) $e_n = 0.99$ and $(c) e_n = 0.9$. Other parameter values are same as in Fig. 5.14.

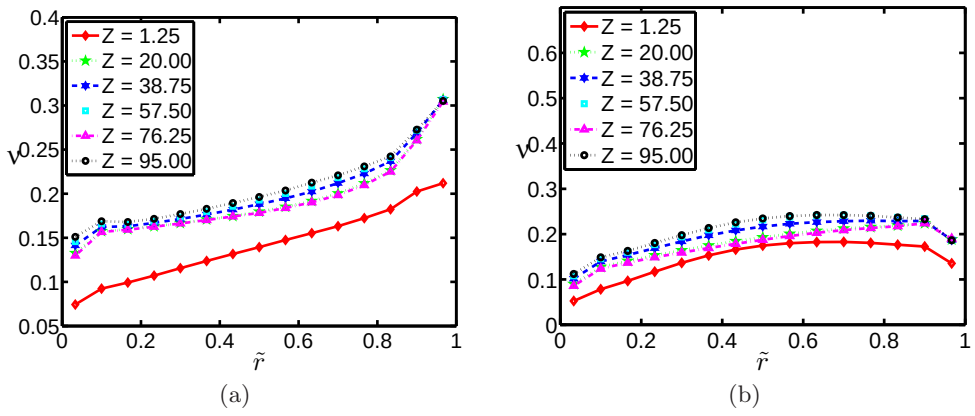

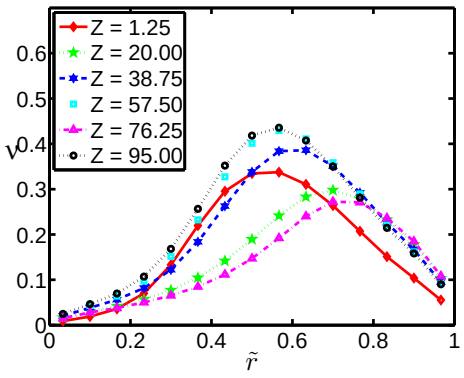

(c)

Figure 5.17: Density variation in radial direction (averaged in the azimuthal direction) at different z: (a) $e_n = 1.0$, (b) $e_n = 0.99$ and (c) $e_n = 0.9$. Other parameter values are same as in Fig. 5.14.

Figure 5.17 shows the radial density variation at different z. The clustering in the radial direction can be seen for $e_n = 0.9$; and the density profile is almost homogeneous for $e_n = 0.99$. Linear variation is observed for non-dissipative system due to the inertial effect of centrifugal force.

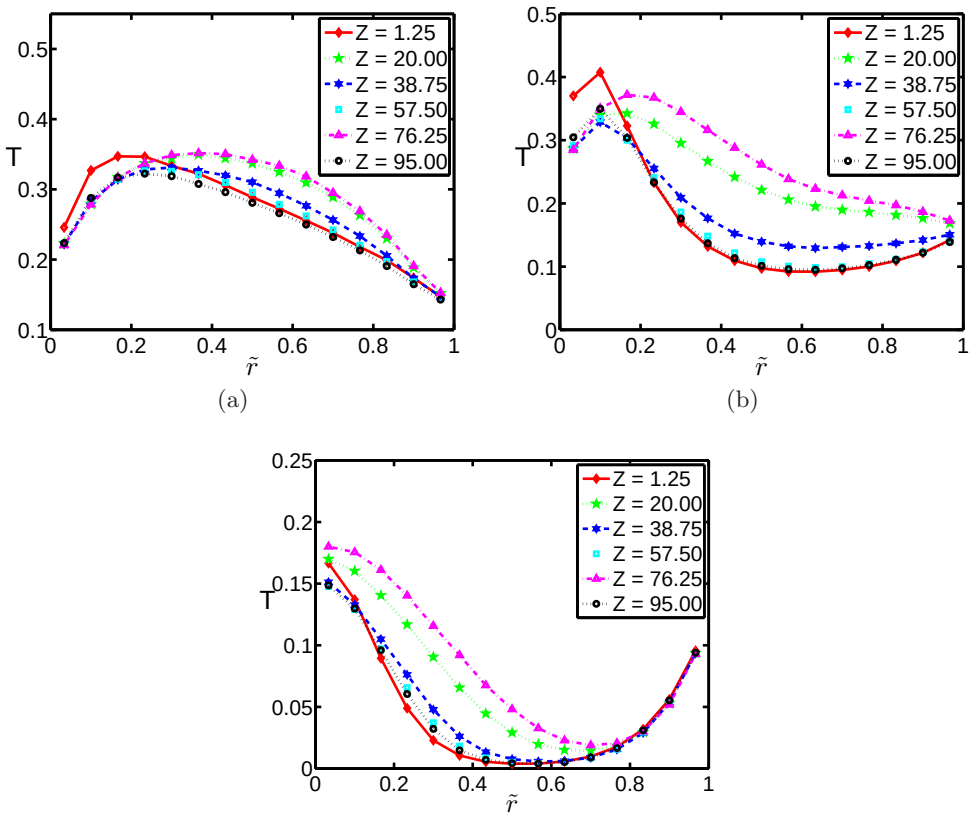

(a) (b)

(c)

Figure 5.18: Radial variation of granular temperature (averaged in the azimuthal direction) at different z: (a) $e_n = 1.0$, (b) $e_n = 0.99$ and (c) $e_n = 0.9$. Other parameter values are same as in Fig. 5.14.

Figure 5.18 shows the radial variation of granular temperature at different z. The lower temperature at the centre in Fig. 5.18(b, c) is due to energy loss caused by the dissipation present in the system, whereas a maxima in temperature can be seen near the centre for $e_n = 1$ in Fig. 5.18(a).

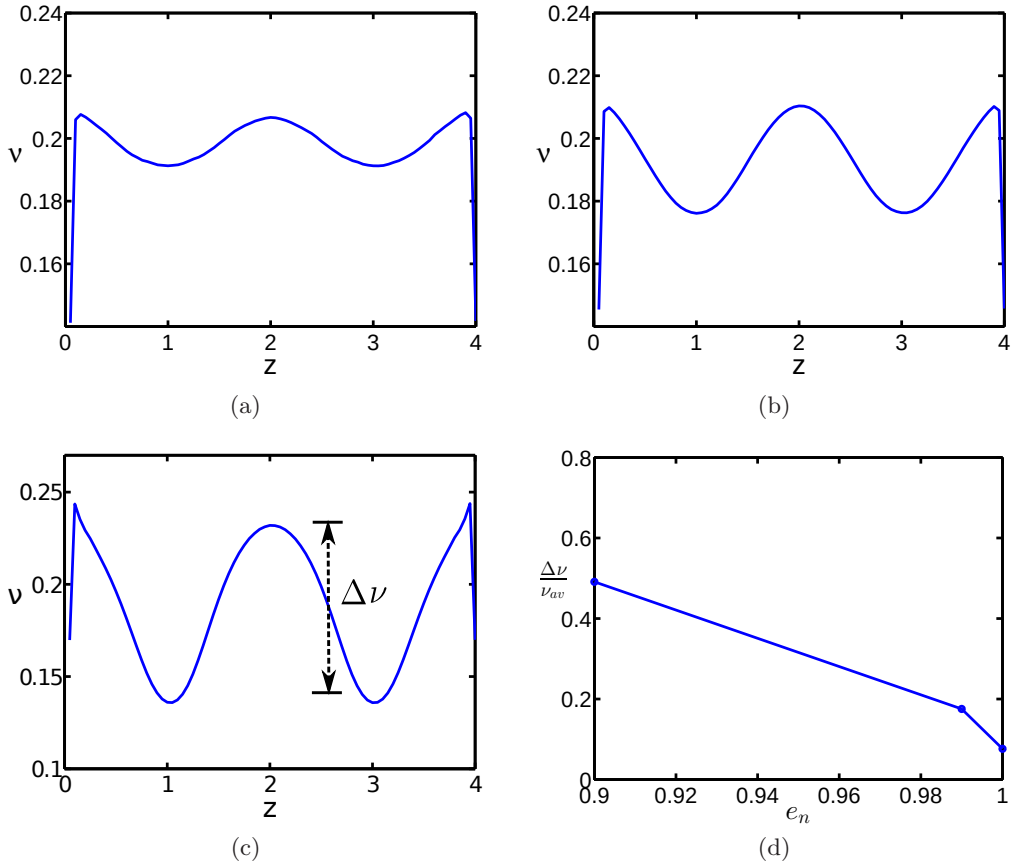

Figure 5.19: Density variation in the axial direction (averaged in the azimuthal and radial direction): (a) $e_n = 1.0$, (b) $e_n = 0.99$, (c) $e_n = 0.9$ and (d) shows the variation of $\frac{\Delta\nu}{\nu_{av}}$ (extent of shear banding) with coefficient of restitution. Other parameter values are same as in Fig. 5.14.

Figure 5.19 shows the axial variation of density averaged over $\tilde{r}$ and θ for different values of coefficient of restituion. The variation in density magnifies with increase in dissipation of the system which is mainly due to clustering. This increase in density is also observed in Fig. 5.17(b) and (c). The quantity excess density $(\frac{\Delta\nu}{\nu_{av}})$, where $\Delta\nu = \nu_{max} - \nu_{min}$, is a measure of extent of axial-clustering in the system and gives an idea on the effect of e_n on the formation of shear bands along th axial direction: these are also called "vorticity-bands" (Goddard 2003; Shukla & Alam 2013). Shifting our focus to axial variation of temperature in Fig. 5.20, the clustering seems to affect the temperature profile by increasing the excess temperature $(\frac{\Delta T}{T_{av}})$, where $\Delta T = T_{max} - T_{min}$, with increase in dissipation as shown in Fig. 5.20(d). This can be explained by the loss in energy due to large number of particle-particle collisions for $e_n = 0.9$. The particle-depleted region will have a higher granular temperature. Therefore, with inclusion of dissipation in the system, the excess density and temperature increases, and the vorticity-bands become stronger with decreasing e_n. Both the quantities are non-dimnesionalised by their

corresponding averages given by ν_{av} and T_{av}, where T_{av} is the average of temperature values shown in Fig. 5.20(c) and ν_{av} is the average volume fraction ($\nu_{av} = 0.2$).

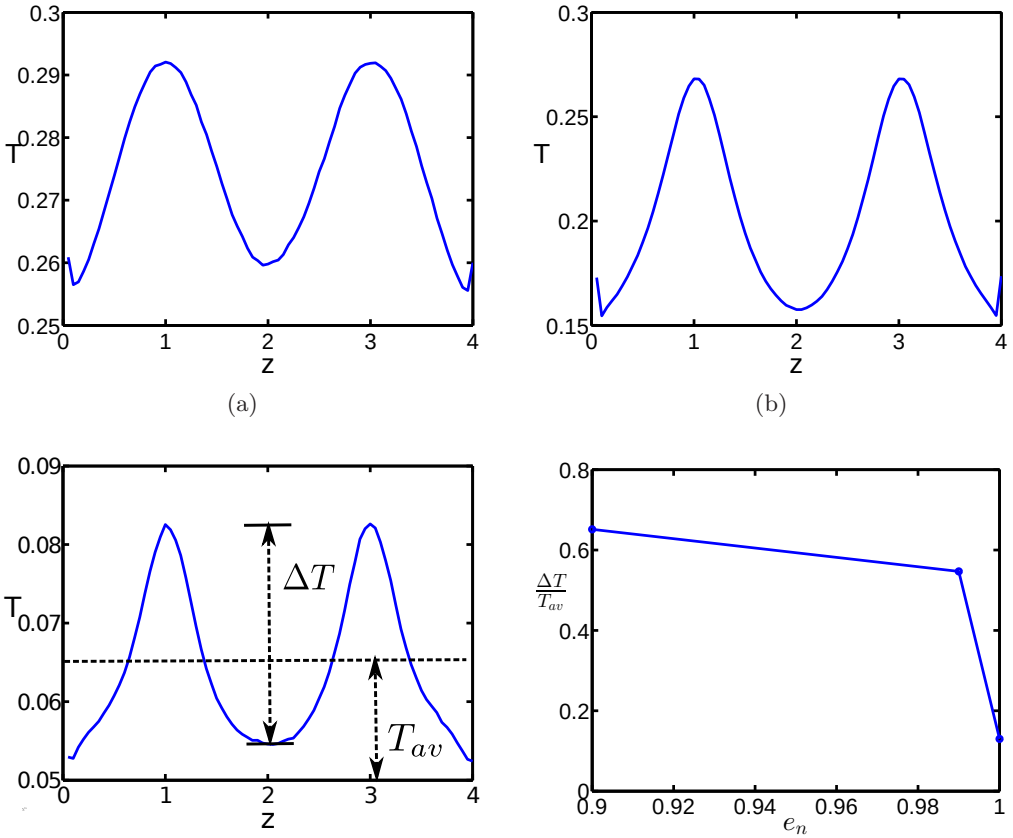

Figure 5.20: Temperature variation in the axial direction (averaged in the azimuthal and radial direction): (a) $e_n = 1.0$, (b) $e_n = 0.99$, (c) $e_n = 0.9$ and (d) shows the variation of $\frac{\Delta T}{T_{av}}$ (extent of shear banding) with coefficient of restitution. Other parameter values are same as in Fig. 5.14.

Figure 5.21 shows the radial variation of azimuthal velocity (V_θ) averaged over θ at different z. The effects of axial length on the tangential velocity can be observed at $z = 20$ and $z = 76.25$ in panels (b) and (c). The velocities at all other z follows a similar trend and are in agreement with the typical velocity profiles observed in TC flows ($V_\theta \sim 1/r$).

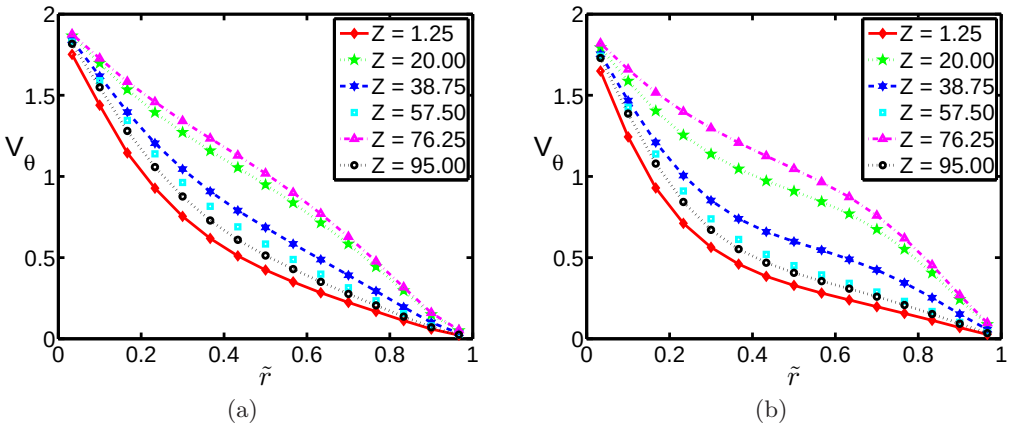

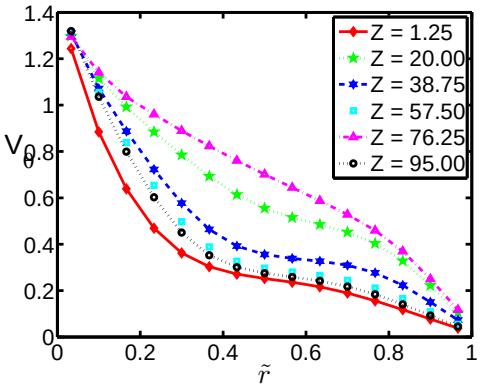

(c)

Figure 5.21: Radial variation of azimuthal velocity (averaged in the azimuthal direction) at different z: (a) $e_n = 1.0$, (b) $e_n = 0.99$ and (c) $e_n = 0.9$. Other parameter values are same as in Fig. 5.14.

Figure 5.22 shows the radial variation of radial velocity averaged over θ for different values of e_n and z. The bulk of the particles are moving in the outer radial direction with a higher magnitude. Only the particles moving towards the centre ($-ve$ V_r) seems to be affected by dissipation with velocities getting flatter with decrease in e_n.

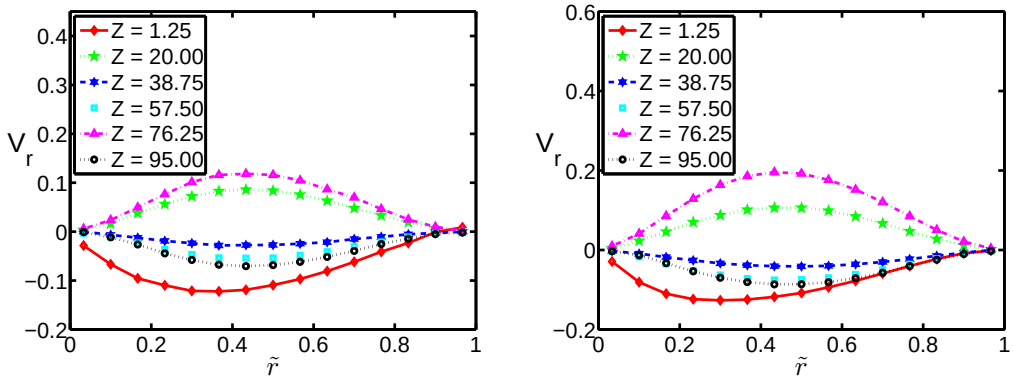

(a) (b)

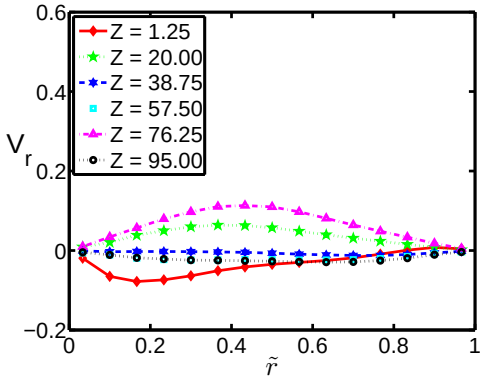

(c)

Figure 5.22: Radial variation of radial velocity (averaged in the azimuthal direction) at different z: (a) $e_n = 1.0$, (b) $e_n = 0.99$ and (c) $e_n = 0.9$. Other parameter values are same as in Fig. 5.14.

The effect of inelastic dissipation can also be seen from axial velocity profiles with the velocities getting flatter with decrease in e_n as shown in Fig. 5.23(b, c)

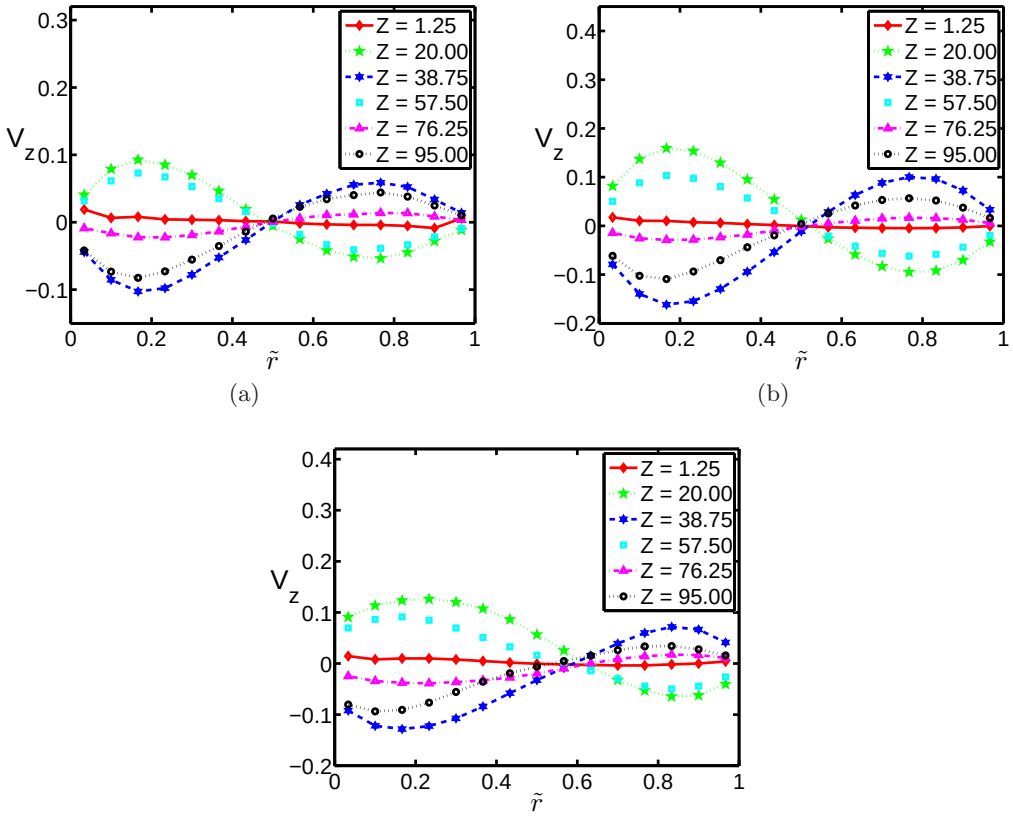

(a) (b)

(c)

Figure 5.23: Radial variation of axial velocity (averaged in the azimuthal direction) at different z: (a) $e_n = 1.0$, (b) $e_n = 0.99$ and (c) $e_n = 0.9$. Other parameter values are same as in Fig. 5.14.

Figure 5.24 shows the radial variation of angular momentum and angular velocity (inset) for different values of e_n. A clear distinction can be seen in the profiles when dissipation is introduced into the system. The degree of non-monotonicity increases with increase in dissipation.

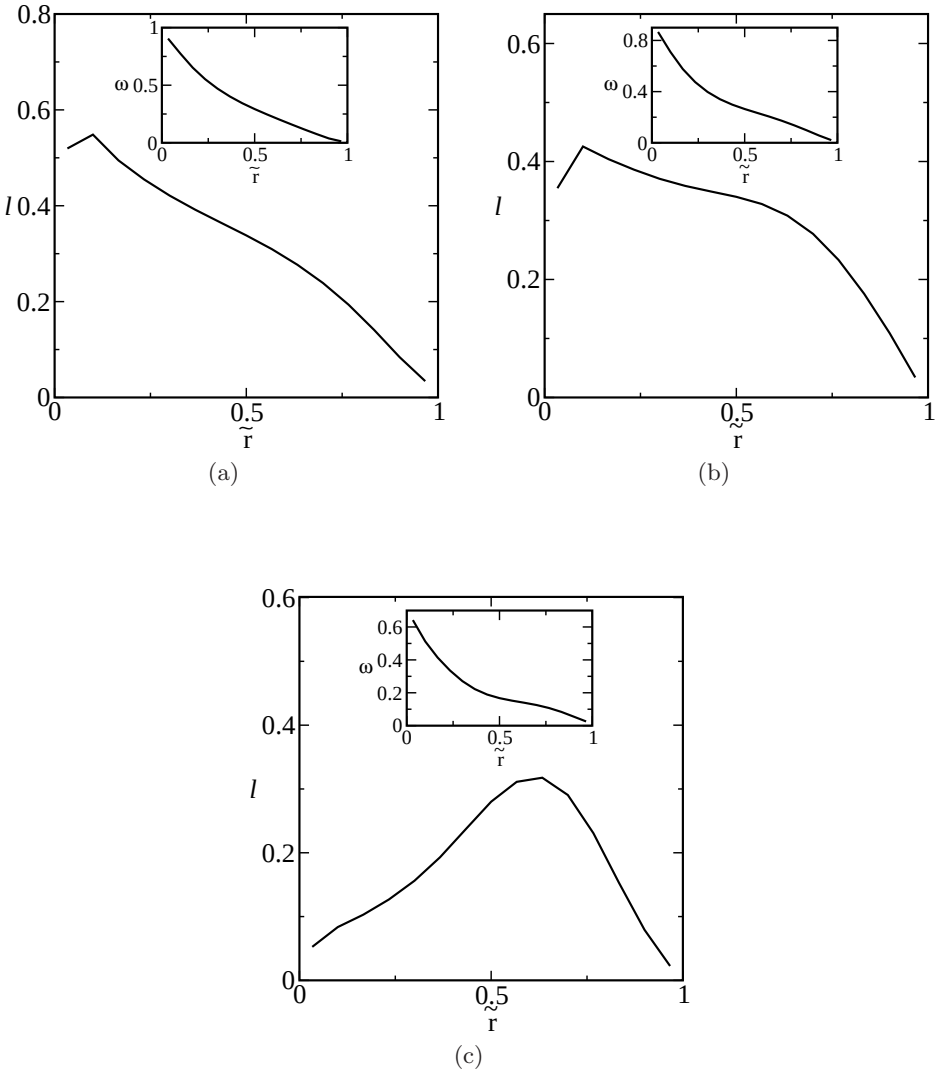

Figure 5.24: Radial variation of angular momentum (averaged in the azimuthal and axial direction): (a) $e_n = 1.0$, (b) $e_n = 0.99$ and (c) $e_n = 0.9$. Inset shows the radial variation of angular velocity. Other parameter values are same as in Fig. 5.14.

Figure 5.25 shows the axial variation of radial velocity (V_r) averaged over (θ, r) for different values of restitution coefficient. The radial distance between peaks of velocity maxima decreases with increase in dissipation. Again the low values of V_r for $e_n = 0.9$ in Fig. 5.25(c) shows that the dissipation slows down the fluid due to the energy loss. Also, with variation in e_n, ΔV_r undergoes a tranistion from maximum at $e_n = 0.99$ to minima at $e_n = 1$ and 0.9 as shown in Fig. 5.25(d).

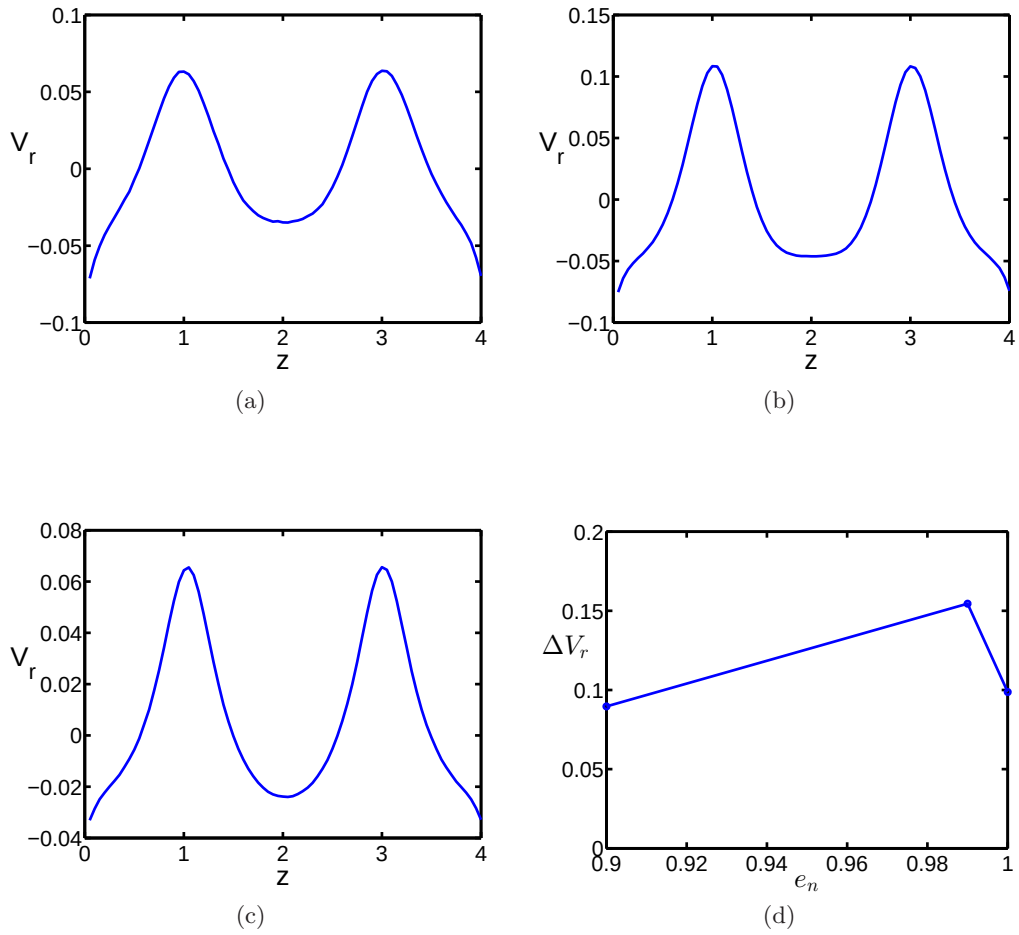

Figure 5.25: Axial variation of radial velocity (averaged in the azimuthal and radial direction): (a) $e_n = 1.0$, (b) $e_n = 0.99$, (c) $e_n = 0.9$ and (d) shows the variation of ΔV_r with coefficient of restitution. Other parameter values are same as in Fig. 5.14.

5.3 Summary and Outlook

The simulation results in this chapter has mainly dealt with the preliminary studies of the effect of inelasticity on the TC system along with different axial wall-boundary conditions. The vortex patterns and average hydrodynamic properties show completely different behaviour on varying the coefficient of restitution. On increasing the dissipation, weaker vortices were formed which lose energy due to dissipation present in the system. The quantities, excess density and excess temperature, increases on increasing the inelastic dissipation. This dependence of excess temperature on e_n has also been observed in a recent study by Alam *et al.* (2015). Also, the "vorticity-bands" formed in the axial direction become stronger with decrease in e_n.

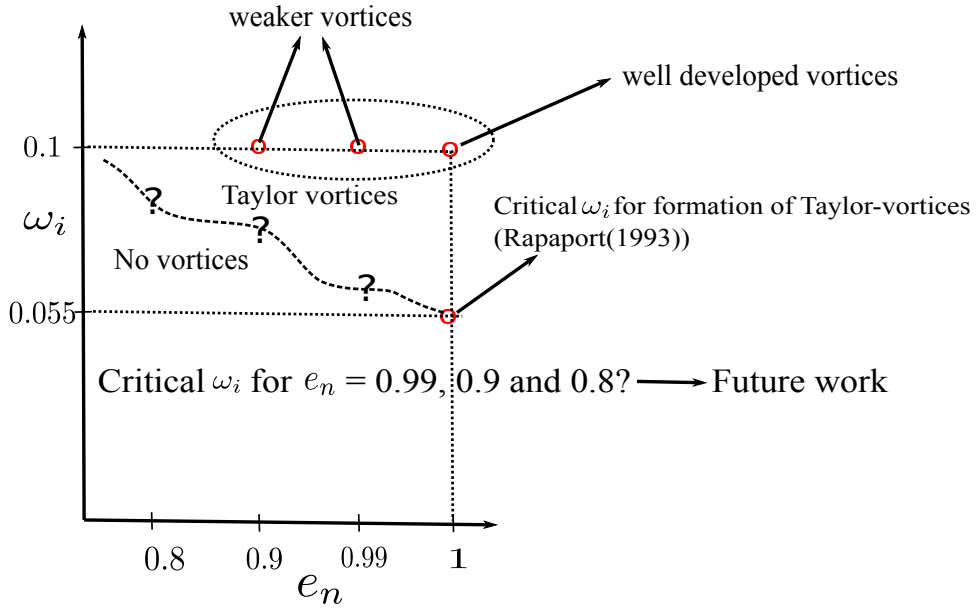

(a)

Figure 5.26: Phase diagram showing approximate demarcation of the region with and without Taylor-like vortices and future prospects in granular Taylor-Couette flow.

Figure 5.26 shows the effect of inelasticity on the formation of Taylor-like vortices. As the strength of vortices decreases with increase in dissipation, it can be expected that the critical ω_i for the formation of vortices might increase with increase in dissipation, thus resulting in a region of phase space as shown in Fig. 5.26 (dotted zig-zag line). Additional runs will involve simulating for different values of e_n and ω_i to find out the exact nature of the phase space. The aim is to get the critical line (dotted zig-zag line) demarcating the region where Taylor-like vortices are observed for a granular TC system. Further work will also involve on sweeping the entire phase space $(\omega_o, \omega_i, e_n)$ with additional effects of inelasticity.

Chapter 6

Summary and Conclusions

Throughout this thesis, we have tried to explain the effects of rarefaction and dissipation in a system of driven granular particles starting with a simple geometry (2D Poiseuille flow) and extending it to a more intricate configuration (2D/3D Taylor-Couette flow). The driving force is gravity in Poiseuille flow and is replaced by centrifugal force in the Taylor-Couette setup. Additional effects of rotation rates ω_i) and dissipation were anaylsed in the latter where inertial force was observed to play a dominant role at high ω_i. Towards the end of Chapter 5, our aim were (i) to assess the role of dissipation on the formation of Taylor vortices and (ii) to elucidate the role of axial end-walls on the transient dynamics of the vortex formation. In this final chapter, we collate our findings and suggest further extension of the work in the future.

6.1 Granular Poiseuille Flow

Two important rarefaction effects, Knudsen minimum and temperature bimodality, were studied and the influence of wall-roughness and inelastic dissipation on these effects were elucidated for a dilute granular Poiseuille flow. Smooth inelastic hard-disks flowing under the effect of gravity were simulated using event-driven molecular dynamics simulations. The walls were observed to play a crucial role in influencing the occurence of a minimum in flow rate. The flow rate goes through a local minima resembling the well-known Knudsen minimum effect (Knudsen 1909) that occurred at a Knudsen number of $Kn \sim O(0.01)$ but the maximum flow rate occurred at a finite Knudsen number of $Kn \sim O(1)$, beyond which the flow-rate decreases. On the other hand, the Knudsen minimum was found to be absent (i) even for quasi-elastic collisions ($e_n \sim 0.99$), irrespective of the wall-roughness, as well as (ii) for relatively rougher walls ($\beta_w > -0.6$) at any e_n. Another important finding was the anomalous decrease in the slip velocity with increasing Kn which is completely opposite to what has been observed in many microfluidic studies on rarefied gases. The origin of this anomalous variation of the slip velocity seems to be tied to the competing effects of (i) the dissipation-induced 'clustering' (i.e. the inhomogeneity of the density field along the transverse/wall-normal direction) and (ii) the rarefaction-induced 'declustering' of particles along the wall-normal direction.

The second part of the work dealt with the bimodality in granular temperature profile which was first theoretically predicted for the case of a molecular gas (Tij & Santos 1994), follwed by studies on granular gases by Tij & Santos (2004). The origin of temperature bimodality was linked to rarefaction for a molecular gas till we found that for granular gases inelastic dissipation dictates the bimodal nature of the temperature at low Knudsen number $Kn > O(0.1)$ beyond which rarefaction effects drive it as observed in its molecular counterpart. Therefore, the observed temperature bimodality in granular Poiseuille flow is a consequence of the competition between dissipation and rarefaction. Increasing inelastic dissipation increases the excess

temperature ratio $\triangle T$ and hence the degree of temperature bimodality is enhanced. Finally we have compared our reusults with the existing theories which uses a kinetic model without incorporating the effect of the walls. The extent of bimodality increases with the increase in dissipation which is completely opposite to what has been predicted by the theory of Tij & Santos (2004).

6.2 Granular Taylor-Couette Flow

After the initial study on channel flow, the next aim was to extend the analysis to a more complex geometry and assess the above-mentioned effects by replacing the gravity with centrifugal force. An extra paramter in the form of rotation of the inner disk (2D) or cylinder (3D) played a crucial in understanding the role of inertial forces on the system which was not seen in the earlier problem. Initial simulations on 2D annular disk revealed that rarefaction and dissipation play the same role as was observed in Poiseuille flow till centrifugal forces take control of the dynamics of the system. At low densities, the rarefaction effects were dominant, but dissipation starts to kick in at high density. The formation of cluster is another common feature of granular flows, and with an increase in density, the cluster transits from a liquid-like behaviour to a solid-like. The temporal evolution of the centre of mass of the system reflects that the cluster reaches a steady state with increase in ω_i more swiftly compared to lower rotation rate.

For 3D, two different axial boundary conditions: periodic and reflecting were used. The code was tested with existing simulation data and the number of vortices was found to increase with increase in the length of system for elastic collisions ($e_n = 1$). On moving to a dissipative system, the vortices appear to have similar structural features for mild dissipation ($e_n = 0.99$) whereas the strength of vortices decreases with further increase in dissipation ($e_n = 0.9$) for reflecting-type boundary conditions. The formation of weak-vortices is due to higher energy loss at the bulk compared to the ends. The reflecting-type boundary condition is found to be responsible for the nucleation of vortices near the end-walls which move towards the centre for an elastic system but due to the inelasticity present in the system ($e_n = 0.9$), the energy gets dissipated and a pair of weak vortices can be seen. The end-walls can therefore be used to modulate the Taylor-like vortices in granular Taylor-Couette flow.

6.3 Extension

The next immediate step in TC flow is to implement the wall boundary conditions with a roughness parameter (β_w) (see Chapter 2) instead of using thermal walls. These boundaries are more realistic for an athermal system like granular flows as the particles will never be in a thermal equilibrium with the walls. Furthermore, an extended analysis to map the entire phase space (ω_o, ω_i, e_n) is essential to validate the presence of various patterns (spiral turbulence, modulated waves etc.) which were observed in earlier studies on incompressible Taylor-Couette flow. It will be interesting to see whether all these patterns can be captured using event molecular dynamics simulations due to its inability to simulate large system with current computing power. Although the extensions mentioned above may all be considered to be viable next steps in the development of our understanding of granular materials, they barely scratch the surface of the

myriad possible developments that could be made based on above discussions. In this thesis, we have made progress in the creation of a robust numerical code for simulating granular flows in a three-dimensional curvilinear geometry. Given the wealth of fascinating experiments reported across the literature, such a wall model and numerical code is likely to be useful to study granular flows in curvilinear geometry.

References

Ahlers, G. & Cannell, D. S. 1983 Vortex-front propagation in rotating couette-taylor flow. *Physical Review Letters* **50** (20), 1583.

Alam, M. & Chikkadi, V. 2010 Velocity distribution function and correlations in a granular poiseuille flow. *Journal of Fluid Mechanics* **653**, 175.

Alam, M., Chikkadi, V. & Gupta, V. 2009 Density waves and the effect of wall roughness in granular poiseuille flow: Simulationand linear stability. *The European Physical Journal Special Topics* **179** (1), 69–90.

Alam, M. & Luding, S. 2003 Rheology of bidisperse granular mixtures via event-driven simulations. *Journal of Fluid Mechanics* **476**, 69–103.

Alam, M. & Luding, S. 2005*a* Energy nonequipartition, rheology, and microstructure in sheared bidisperse granular mixtures. *Physics of Fluids (1994-present)* **17** (6), 063303.

Alam, M. & Luding, S. 2005*b* Non-newtonian granular fluids: Simulation and theory. *Powders and Grains 2005* p. 1141.

Alam, M., Mahajan, A. & Shivanna, D. 2015 On knudsen-minimum effect and temperature bimodality in a dilute granular poiseuille flow. *Journal of Fluid Mechanics* **782**, 99–126.

Allen, M. P. & Tildesley, D. J. 1989 *Computer simulation of liquids*. Oxford university press.

Andereck, C. D., Liu, S. & Swinney, H. L. 1986 Flow regimes in a circular couette system with independently rotating cylinders. *Journal of Fluid Mechanics* **164**, 155–183.

Aoki, K., Sone, Y. & Yoshimoto, M. 1999 Numerical analysis of the taylor-couette problem for a rarefied gas by the direct simulation monte carlo method. In *International symposium on rarefied gas dynamics*.

Aoki, K., Takata, S. & Nakanishi, T. 2002 Poiseuille-type flow of a rarefied gas between two parallel plates driven by a uniform external force. *Physical Review E* **65** (2), 026315.

Aoki, K., Yoshida, H., Nakanishi, T. & Garcia, A. L. 2003 Inverted velocity profile in the cylindrical couette flow of a rarefied gas. *PHYSICAL REVIEW-SERIES E-* **68** (1; PART 1), 016302–016302.

Bagnold, R. A. 1941 *The physics of blown sand and desert dunes*. Courier Corporation.

Bagnold, R. A. 1954 Experiments on a gravity-free dispersion of large solid spheres in a newtonian fluid under shear. In *Proceedings of the Royal Society of London A: Mathematical, Physical and Engineering Sciences*, , vol. 225, pp. 49–63. The Royal Society.

Benjamin, T. & Mullin, T. 1981 Anomalous modes in the taylor experiment. In *Proceedings of the Royal Society of London A: Mathematical, Physical and Engineering Sciences*, , vol. 377, pp. 221–249. The Royal Society.

Benjamin, T. B. 1978 Bifurcation phenomena in steady flows of a viscous fluid. i. theory. In *Proceedings of the Royal Society of London A: Mathematical, Physical and Engineering Sciences*, , vol. 359, pp. 1–26. The Royal Society.

Bird, G. A. 1994 Molecular gas dynamics and the direct simulation of gas flows .

Bocquet, L., Losert, W., Schalk, D., Lubensky, T. & Gollub, J. 2001 Granular shear flow dynamics and forces: Experiment and continuum theory. *Physical review E* **65** (1), 011307.

Bödewadt, U. 1940 Die drehströmung über festem grunde. *ZAMM-Journal of Applied Mathematics and Mechanics/Zeitschrift für Angewandte Mathematik und Mechanik* **20** (5), 241–253.

Brilliantov, N. & Pöschel, T. 2004 The physics of granular media .

Brown, R. & Richards, J. C. 1970 Principles of powder mechanics .

Burnett, D. 1935 The distribution of velocities in a slightly non-uniform gas. *Proceedings of the London Mathematical Society* **2** (1), 385–430.

Campbell, C. S. 1990 Rapid granular flows. *Annual Review of Fluid Mechanics* **22** (1), 57–90.

Cercignani, C. 2000 *Rarefied gas dynamics: from basic concepts to actual calculations*, , vol. 21. Cambridge University Press.

Cercignani, C. & Daneri, A. 1963 Flow of a rarefied gas between two parallel plates. *Journal of Applied Physics* **34** (12), 3509–3513.

Chandrasekhar, S. 1960 The stability of non-dissipative couette flow in hydromagnetics. *Proceedings of the National Academy of Sciences* **46** (2), 253–257.

Chapman, S. & Cowling, T. G. 1970 *The mathematical theory of non-uniform gases: an account of the kinetic theory of viscosity, thermal conduction and diffusion in gases*. Cambridge university press.

Chen, J.-C. & Kuo, J.-Y. 1990 The linear stability of steady circular couette flow with a small radial temperature gradient. *Physics of Fluids A: Fluid Dynamics (1989-1993)* **2** (9), 1585–1591.

Cheng, X., Lechman, J. B., Fernandez-Barbero, A., Grest, G. S., Jaeger, H. M., Karczmar, G. S., Möbius, M. E. & Nagel, S. R. 2006 Three-dimensional shear in granular flow. *Physical review letters* **96** (3), 038001.

Chikkadi & Alam 2007 Velocity distribution and the effect of wall roughness in granular poiseuille flow. *Physical Review E* **75** (5), 051306.

Chikkadi, V. & Alam, M. 2009 Slip velocity and stresses in granular poiseuille flow via event-driven simulation. *Physical Review E* **80** (2), 021303.

Clever, R. & Busse, F. H. 1997 Tertiary and quaternary solutions for plane couette flow. *Journal of Fluid Mechanics* **344**, 137–153.

Cliffe, K. & Mullin, T. (985 A numerical and experimental study of anomalous modes in the taylor experiment. *Journal of Fluid Mechanics* **153**, 243–258.

Cole, J. 1965 Experiments of taylor vortices between eccentric rotating cylinders. In *Proceedings of the 2nd Australian Conference on Hydraulics and Fluid Mechanics*, pp. 313–320.

Conway, S. L., Shinbrot, T. & Glasser, B. J. 2004 A taylor vortex analogy in granular flows. *Nature* **431** (7007), 433–437.

Couette, M. 1888 Sur un nouvel appareil pour lâétude du frottement des fluides. *Comptes Rendus* **107**, 388–390.

Czarny, O., Serre, E., Bontoux, P. & Lueptow, R. M. 2003 Interaction between ekman pumping and the centrifugal instability in taylor–couette flow. *Physics of Fluids (1994-present)* **15** (2), 467–477.

Dubrulle, B., Dauchot, O., Daviaud, F., Longaretti, P.-Y., Richard, D. & Zahn, J.-P. 2005 Stability and turbulent transport in taylor–couette flow from analysis of experimental data. *Physics of Fluids (1994-present)* **17** (9), 095103.

Duran, J. 2012 *Sands, powders, and grains: an introduction to the physics of granular materials*. Springer Science & Business Media.

Einzel, D., Panzer, P. & Liu, M. 1990 Boundary condition for fluid flow: curved or rough surfaces. *Physical review letters* **64** (19), 2269.

Faraday, M. 1831 On the forms and states assumed by fluids in contact with vibrating elastic surfaces. *Philos. Trans. R. Soc. London* **121** (319), 1831.

Forterre, Y. & Pouliquen, O. 2008 Flows of dense granular media. *Annu. Rev. Fluid Mech.* **40**, 1–24.

Galvin, J., Hrenya, C. & Wildman, R. 2007 On the role of the knudsen layer in rapid granular flows. *Journal of Fluid Mechanics* **585**, 73–92.

Gayen, B. & Alam, M. 2008 Orientational correlation and velocity distributions in uniform shear flow of a dilute granular gas. *Physical review letters* **100** (6), 068002.

van Gils, D. P., Huisman, S. G., Grossmann, S., Sun, C. & Lohse, D. 2012 Optimal taylor–couette turbulence. *Journal of fluid mechanics* **706**, 118–149.

Goddard, J. 2003 Material instability in complex fluids. *Annual review of fluid mechanics* **35** (1), 113–133.

Goldhirsch, I. 2003 Rapid granular flows. *Annual review of fluid mechanics* **35** (1), 267–293.

Grad, H. 1949 On the kinetic theory of rarefied gases. *Communications on pure and applied mathematics* **2** (4), 331–407.

van Hecke, Martin Fenistein, D. & van de Meent, J. W. 2004 Universal and wide shear zones in granular bulk flow. *Physical review letters* **92** (9), 094301.

Hirshfeld, D. & Rapaport, D. 1998 Molecular dynamics simulation of taylor-couette vortex formation. *Physical review letters* **80** (24), 5337.

Hollerbach, R. & Fournier, A. 2005 End-effects in rapidly rotating cylindrical taylor-couette flow. *arXiv preprint astro-ph/0506081* .

Jaeger, H., Liu, C.-h. & Nagel, S. R. 1989 Relaxation at the angle of repose. *Physical Review Letters* **62** (1), 40.

Jaeger, H. M., Nagel, S. R. & Behringer, R. P. 1996 Granular solids, liquids, and gases. *Reviews of Modern Physics* **68** (4), 1259–1273.

Jasti, V. & Higgs III, C. F. 2008 Experimental study of granular flows in a rough annular shear cell. *Physical Review E* **78** (4), 041306.

Jenkins, J. & Richman, M. 1985 Kinetic theory for plane flows of a dense gas of identical, rough, inelastic, circular disks. *Physics of Fluids (1958-1988)* **28** (12), 3485–3494.

Jenkins, J. & Savage, S. 1983 A theory for the rapid flow of identical, smooth, nearly elastic, spherical particles. *Journal of Fluid Mechanics* **130**, 187–202.

Jones, C. 1981 Nonlinear taylor vortices and their stability. *Journal of Fluid Mechanics* **102**, 249–261.

Kao, K.-H. & Chow, C.-Y. 1992 Linear stability of compressible taylor–couette flow. *Physics of Fluids A: Fluid Dynamics (1989-1993)* **4** (5), 984–996.

Khain, E., Meerson, B. & Sasorov, P. V. 2008 Knudsen temperature jump and the navier-stokes hydrodynamics of granular gases driven by thermal walls. *Physical Review E* **78** (4), 041303.

Knudsen, M. 1909 Die gesetze der molekularstromung und der inneren reibungsstromung der gase durch rohren. *Ann. Phys.* **333**, 75–130.

Kogan, M. 1969 Rarefied gas dynamics. *Plenum Press, New York* **2**, l.

Krishnaraj, K. & Nott, P. R. 2016 A dilation-driven vortex flow in sheared granular materials explains a rheometric anomaly. *Nature communications* **7**.

Kuhlthau, A. 1960 Recent low-density experiments using rotating cylinder techniques. In *Rarefied Gas Dynamics*, , vol. 1, p. 192.

Liss, E. D., Conway, S. L. & Glasser, B. J. 2002 Density waves in gravity-driven granular flow through a channel. *Physics of Fluids* **14**, 3309.

Lubachevsky, B. D. 1991 How to simulate billiards and similar systems. *Journal of Computational Physics* **94** (2), 255–283.

Luding, S. & McNamara, S. 1998 How to handle the inelastic collapse of a dissipative hard-sphere gas with the tc model. *Granular Matter* **1** (3), 113–128.

Mallock, A. 1888 Determination of the viscosity of water. *Proceedings of the Royal Society of London* **45** (273-279), 126–132.

Mansour, M., Baras, F. & Garcia, A. L. 1997 On the validity of hydrodynamics in plane poiseuille flows. *Physica A: Statistical Mechanics and its Applications* **240** (1), 255–267.

Marcus, P. S. 1984 Simulation of taylor-couette flow. part 1. numerical methods and comparison with experiment. *Journal of Fluid Mechanics* **146**, 45–64.

Mareschal, M. & Kestemont, E. 1987 Order and fluctuations in nonequilibrium molecular dynamics simulations of two-dimensional fluids. *Journal of statistical physics* **48** (5-6), 1187–1201.

Maxwell, J. C. 1867 Philos. *Trans. R. Soc. London Ser. A* **170**, 231.

Mehandia, V., Gutam, K. J. & Nott, P. R. 2012 Anomalous stress profile in a sheared granular column. *Physical review letters* **109** (12), 128002.

Minguito & Meerson 2007 Phase separation of a driven granular gas in annular geometry. *Physical Review E* **75** (1), 011304.

Moser, R., Moin, P. & Leonard, A. 1983 A spectral numerical method for the navier-stokes equations with applications to taylor-couette flow. *Journal of Computational Physics* **52** (3), 524–544.

Murdoch, N., Rozitis, B., Nordstrom, K., Green, S., Michel, P., de Lophem, T.-L. & Losert, W. 2013 Granular convection in microgravity. *Physical review letters* **110** (1), 018307.

Nedderman, R. M. 2005 *Statics and kinematics of granular materials*. Cambridge University Press.

Peters, I. R., Majumdar, S. & Jaeger, H. M. 2016 Direct observation of dynamic shear jamming in dense suspensions. *Nature* **532** (7598), 214–217.

Pöschel, T. & Luding, S. 2001 *Granular gases*, , vol. 564. Springer Science & Business Media.

Pöschel, T. & Schwager, T. 2005 *Computational granular dynamics: models and algorithms*. Springer Science & Business Media.

Puhl, A., Mansour, M. M. & Mareschal, M. 1989 Quantitative comparison of molecular dynamics with hydrodynamics in rayleigh-benard convection. *Physical Review A* **40** (4), 1999.

Raman, C. 1923 A theory of the viscosity of liquids. *Nature* **111**, 532–533.

Rao, K. K. & Nott, P. R. 2008 *An introduction to granular flow*. Cambridge University Press Cambridge.

Rapaport, D. 1987 Microscale hydrodynamics: Discrete-particle simulation of evolving flow patterns. *Physical Review A* **36** (7), 3288.

Rapaport, D. & Clementi, E. 1986 Eddy formation in obstructed fluid flow: a molecular-dynamics study. *Physical review letters* **57** (6), 695.

Rayleigh, L. 1917 On the dynamics of revolving fluids. *Proceedings of the Royal Society of London. Series A, Containing Papers of a Mathematical and Physical Character* pp. 148–154.

Riechelmann, D. & Nanbu, K. 1993 Monte carlo direct simulation of the taylor instability in rarefied gas. *Physics of Fluids A: Fluid Dynamics (1989-1993)* **5** (11), 2585–2587.

Rongali, R. & Alam, M. 2014 Higher-order effects on orientational correlation and relaxation dynamics in homogeneous cooling of a rough granular gas. *Physical Review E* **89** (6), 062201.

Saha, S. & Alam, M. 2014 Non-newtonian stress, collisional dissipation and heat flux in the shear flow of inelastic disks: a reduction via gradâs moment method. *Journal of Fluid Mechanics* **757**, 251–296.

Saha, S. & Alam, M. 2016 Normal stress differences, their origin and constitutive relations for a sheared granular fluid. *Journal of Fluid Mechanics* **795**, 549–580.

Sela, N. & Goldhirsch, I. 1998 Hydrodynamic equations for rapid flows of smooth inelastic spheres, to burnett order. *Journal of Fluid Mechanics* **361**, 41–74.

Shukla, P. & Alam, M. 2013 Nonlinear vorticity-banding instability in granular plane couette flow: higher-order landau coefficients, bistability and the bifurcation scenario. *Journal of Fluid Mechanics* **718**, 131–180.

Stefanov, S. & Cercignani, C. 1993 Monte carlo simulation of the taylor–couette flow of a rarefied gas. *Journal of Fluid Mechanics* **256**, 199–213.

Tagg, R. 1994 The couette-taylor problem. *Nonlinear Science Today* **4** (3), 1–25.

Tardos, G. I., Khan, M. I. & Schaeffer, D. G. 1998 Forces on a slowly rotating, rough cylinder in a couette device containing a dry, frictional powder. *Physics of Fluids (1994-present)* **10** (2), 335–341.

Taylor, G. I. 1923 Stability of a viscous liquid contained between two rotating cylinders. *Philosophical Transactions of the Royal Society of London. Series A, Containing Papers of a Mathematical or Physical Character* pp. 289–343.

Tehver, R., Toigo, F., Koplik, J. & Banavar, J. R. 1998 Thermal walls in computer simulations. *Physical Review E* **57** (1), R17.

Tibbs, K. W., Baras, F. & Garcia, A. L. 1997 Anomalous flow profile due to the curvature effect on slip length. *Physical Review E* **56** (2), 2282.

Tij, M. & Santos, A. 1994 Perturbation analysis of a stationary nonequilibrium flow generated by an external force. *Journal of statistical physics* **76** (5-6), 1399–1414.

Tij, M. & Santos, A. 2004 Poiseuille flow in a heated granular gas. *Journal of statistical physics* **117** (5-6), 901–928.

Torrilhon, M. & Struchtrup, H. 2004 Regularized 13-moment equations: shock structure calculations and comparison to burnett models. *Journal of Fluid Mechanics* **513**, 171–198.

Trevelyan, D. J. & Zaki, T. A. 2016 Wavy taylor vortices in molecular dynamics simulation of cylindrical couette flow. *Physical Review E* **93** (4), 043107.

Wereley, S. T. & Lueptow, R. M. 1998 Spatio-temporal character of non-wavy and wavy taylor–couette flow. *Journal of Fluid Mechanics* **364**, 59–80.

Yoshida, H. & Aoki, K. 2006 Linear stability of the cylindrical couette flow of a rarefied gas. *Physical Review E* **73** (2), 021201.